

ulm university universität
uulm

Reverse Engineering the Kinetics of Grain Growth in Al-Based Polycrystals by Microstructural Mapping in 4D

Dissertation

zur Erlangung des akademischen Grades

Doktor-Ingenieur
(Dr.-Ing.)

der Fakultät für Ingenieurwissenschaften, Informatik und Psychologie
der Universität Ulm

von
Mingyan Wang
aus Shandong, China

Gutachter:	Prof. Carl E. Krill III, PhD
	Prof. Marc Bernacki
Amtierender Dekan:	Prof. Dr.-Ing Maurits Ortmanns

Ulm, 17. June 2021

Abstract

Many metallic materials used in industry are initially produced as large castings. They are further processed by deformation and annealing to obtain the final product. During the annealing step, the phenomena of recovery, recrystallization and grain growth take place. This work focuses on the final stage of annealing—grain growth—which is a key process for controlling the microstructure and achieving the desired materials properties. Although grain growth has been studied in polycrystalline materials for many years, our understanding of its underlying mechanisms remains incomplete. Even in the case of normal grain growth, computer simulations differ significantly from experimental findings. For example, the grain size distributions observed in real materials tend to be less symmetric than those predicted by simulations operating under the assumption of isotropic boundary properties, and discrepancies between the measured and simulated evolution of individual grains can be particularly pronounced.

Instead of modeling grain growth in the conventional manner using boundary parameters derived from physical principles, we elected to try the opposite approach: *i.e.,* to work backwards from experimental measurements to the kinetics of individual grain boundaries. A reverse engineering type of analysis was established, allowing the boundary reduced mobility (the product of boundary mobility and energy) to be extracted from 3D microstructural evolution. Employing synchrotron-based 3D x-ray diffraction (3DXRD) microscopy, we investigated thermally induced coarsening in two different Al-based alloys. We collected and reconstructed a series of microstructural snapshots between isothermal annealing steps. In these time-resolved 3D datasets, we followed the morphology, misorientation, inclination and migration of thousands of boundaries in a single sample, forming the basis for a robust statistical analysis of local growth kinetics.

In an Al-1 wt% Mg specimen, the microstructural evolution and the associated grain statistics demonstrated that abnormal grain growth took place. In comparison, the coarsening of an Al-5 wt% Cu specimen resembled normal grain growth. On the grain boundary level, many low-angle grain boundaries were found in AlMg. Through the reverse engineering procedure, the reduced mobility of grain boundaries was extracted and related to the boundary misorientation and inclination. The results show that the reduced mobility manifests a clear trend with respect to misorientation. Beyond this general trend, the data spreads reveal that grain boundaries of similar misorientation may vary significantly in their reduced mobility. Such spreads were found to be larger in the AlMg sample, for which the extreme values in reduced mobility were often associated with the boundaries of abnormal grains. From an analysis of the extracted reduced mobility, we determined that factors beyond the usual capillary force must have altered the migration of grain boundaries in AlMg, facilitating the abnormal grain growth. Moreover, in both samples the mobility of individual grain boundaries was found to vary over time (rather than maintaining a constant value), suggesting that the reduced mobility depends on atomic-scale details of the growth mechanism that are overlooked by mesoscale grain growth simulations.

Contents

Abstract i

Contents iii

1 Introduction 1
- 1.1 Open questions . . . 4
- 1.2 Structure of the thesis . . . 6

2 Coarsening in Polycrystalline Materials 9
- 2.1 Grain boundaries in polycrystalline materials . . . 9
  - 2.1.1 Five-parameter description of grain boundaries . . . 10
    - 2.1.1.1 Misorientation . . . 10
    - 2.1.1.2 Inclination . . . 12
  - 2.1.2 Structure of grain boundaries . . . 14
    - 2.1.2.1 Low/High-angle grain boundaries . . . 14
    - 2.1.2.2 Tilt/twist grain boundaries . . . 18
  - 2.1.3 Grain boundary energy and its measurement . . . 19
  - 2.1.4 Grain boundary mobility and its measurement . . . 21
    - 2.1.4.1 Capillary-driven boundary migration technique . . . 22
    - 2.1.4.2 Bicrystal in a magnetic field . . . 24
    - 2.1.4.3 Observation of boundary migration in bicrystals . . . 24
- 2.2 Grain growth . . . 25
  - 2.2.1 Abnormal grain growth . . . 27
- 2.3 Ostwald Ripening . . . 29

3 Computer Simulation 33
- 3.1 Introduction to simulation methods . . . 33
- 3.2 Phase field simulation of ideal grain growth . . . 34
- 3.3 Numerical solution of the phase field equations . . . 35
- 3.4 Grain growth with anisotropic boundary properties . . . 37
- 3.5 Phase field simulation of Ostwald ripening . . . 41

4 4D Characterization of Microstructure 43
- 4.1 3DXRD and other comparable 3D characterization techniques . . . 44
- 4.2 Data collection . . . 46
- 4.3 Data reconstruction and post-processing . . . 48
  - 4.3.1 Far-field data reconstruction . . . 48
  - 4.3.2 Near-field data reconstruction . . . 51

4.3.3 Post-processing . . . 52
4.3.3.1 Stitching . . . 52
4.3.3.2 Registration . . . 52
4.3.3.3 Tracking . . . 53
4.3.3.4 Smoothing . . . 53

5 Reverse Engineering Method 55
5.1 Measurement of boundary migration velocity . . . 56
5.2 Measurement of boundary curvature . . . 58
5.3 Method validation . . . 63
5.4 A guide to experimental design . . . 67

6 Coarsening in an Al-Mg Alloy 71
6.1 Sample preparation and 4D data acquisition . . . 71
6.2 Microstructural evolution at the grain level . . . 72
6.3 Microstructural evolution at the grain boundary level . . . 76
6.4 Reverse engineering the grain boundary M' . . . 79
6.5 Discussion and final remarks . . . 82
6.5.1 A case study . . . 82
6.5.2 Final remarks . . . 84

7 Coarsening in an Al-Cu Alloy 87
7.1 Sample preparation and 4D data acquisition . . . 87
7.2 Microstructural evolution at the grain level . . . 88
7.3 Microstructural evolution at the grain boundary level . . . 94
7.4 Reverse engineering the grain boundary M' . . . 96
7.5 Final remarks . . . 98

8 Discussion and Conclusions 101
8.1 Validity of the reverse engineering method . . . 101
8.2 Validity of the curvature-driven mechanism of boundary migration . . . 104
8.3 Dependency of boundary reduced mobility on macroscopic boundary properties . . . 108
8.4 Conclusions . . . 114

Bibliography 117

List of Publications 137

List of Conference Contributions 139

Acknowledgments 141

Chapter 1

Introduction

Most solid, structural materials used in industry are polycrystalline, which means that they are composed of a collection of many small crystals—namely, grains. When grains of different orientations impinge on each other, they form grain boundaries (GBs). Grain boundaries are considered to be the most dominant defects in polycrystalline materials [1]. These microscopic defects have a great influence on a material's macroscopic properties, including strength, toughness, corrosion resistance, electrical conductivity, magnetic susceptibility, etc. [1–3]. For example, grain boundaries block the movement of dislocations, owing to the orientation discontinuity of the adjacent grains; in turn, this blockage hinders the onset of plastic deformation. Hall and Petch observed that the yield strength of a material is inversely correlated with the square root of the average grain size [4, 5]. Consequently, the strength of a material can be increased by reducing its average grain size, which corresponds to incorporating a larger area of GBs into a given sample volume. Finer grain size leads to an increase in the total area of GBs, therefore resulting in a higher strength. Understanding GBs in polycrystalline materials is vital for obtaining the optimal processing parameters that lead to desired properties.

Grain boundaries store excess free energy. When a kinetic driving force is applied to a material, such as a stress or a thermal load, the thermodynamically favored minimization of this excess energy will occur via the reduction in GB area of the system. Known as grain growth, the latter process leads to a decrease in the total number of grains and an increase in the mean grain radius. Grain growth is one of the most fundamental phenomena in metallurgy. During grain growth, atoms diffuse from one grain to another, resulting in the migration of GBs. In an early theoretical treatment of the topic from 1952, Burke and Turnbull proposed a model for GB migration [6]:

$$v = M\gamma H, \tag{1.1}$$

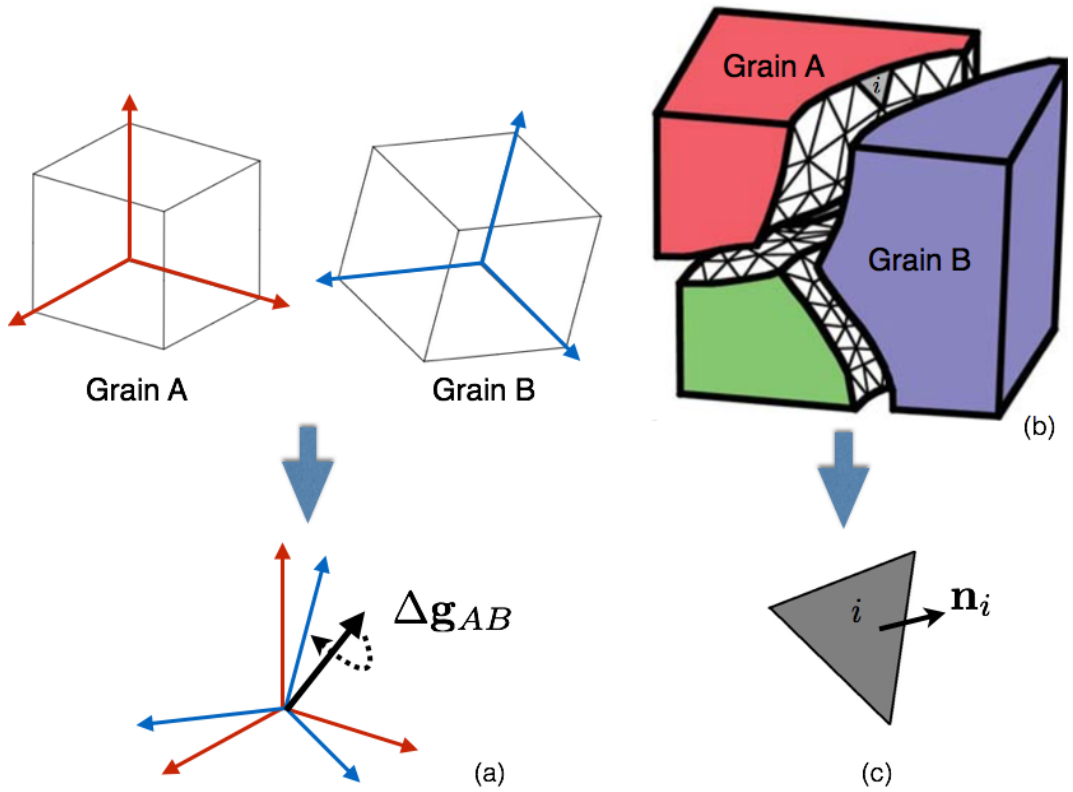

FIGURE 1.1: (a) Illustration of the crystal lattice orientation of two grains meeting at a GB. The misorientation between the crystal lattices of Grain A and B can be quantified by a 3D rotation matrix, $\Delta \mathbf{g}_{AB}$. (b, c) Along the GB between Grains A and B, the direction of the boundary normal may vary. At location i of the boundary, the boundary inclination can be specified by the local unit normal $\mathbf{n}_i$. Panel (b) was reprinted by permission from Springer Nature: Springer Nature, JOM Journal of the Minerals, Metals and Materials Society, 59(9), The distribution of grain boundary planes in polycrystals, G. S. Rohrer, 38–42, Copyright 2007.

where v denotes the migration velocity of a GB, and M, γ and H are the boundary mobility, energy and mean curvature, respectively. Although the form of Eq. 1.1 appears to be simple, an abundance of subsequent research shows that one of the difficulties in understanding the migration of GBs in polycrystalline materials is the multidimensional space describing the structure of a given GB. At the macroscopic level, a GB can be characterized by five degrees of freedom, including three to specify the boundary misorientation (the misalignment between two crystal lattices) and two to specify the boundary inclination (the direction of the boundary normal) [7]. In Fig. 1.1, the definitions of boundary misorientation and inclination are illustrated schematically. Two of the parameters appearing in Eq. 1.1, M and γ, are known to vary in their values with respect to these five parameters [1, 8].

According to Eq. 1.1, it is not the dependence of M or γ separately on the GB degrees of freedom that is important to grain growth, but rather the product of M and γ, which is often called the reduced GB mobility M'. Unfortunately, knowledge of how M'

depends on boundary macroscopic properties is lacking [9]. In this area of research, one of the most successful measurement strategies is based on the so-called bicrystal technique [1]. Among various bicrystal arrangements, the Sun-Bauer configuration is most notable [10–13]. From an experimental observation of bicrystal boundary migration, one can extract a value for M' with respect to a specific combination of GB misorientation and inclination. In other words, one measurement yields a single point in the five-dimensional GB parameter space; as a result, an impractically large number of measurements would be necessary to characterize the entire parameter space. Additionally, bicrystal experiments are quite tedious to carry out, requiring fabrication of a bicrystal, measurement of the boundary location, and pre-treatment of thermal grooves. The migration of a bicrystal GB is also found to be very sensitive to the bicrystal quality, *e.g.,* to the sample surface roughness, which complicates the interpretation of experimental results [14].

In order to apply Eq. 1.1 to a real polycrystalline material, we need to determine M' throughout the five-dimensional boundary space, as any polycrystalline sample will contain hundreds of thousands of GBs, each with its own combination of misorientation and inclination. Three-dimensional microstructural characterization is necessary to recover the full information regarding GB misorientation and inclination. Additionally, M' is accessible only when a 3D microstructure is mapped in a time-resolved manner, as illustrated in Fig. 1.2. For properly chosen combinations of annealing temperature and time, a GB located at time t_i is trackable at later time t_{i+1}. From the migration distance ΔR between times t_i and t_{i+1}, the migration velocity v can be estimated. Meanwhile, the boundary curvature H can be evaluated from the GB morphology. Knowing these quantities, we can calculate M' simply by rearranging Eq. 1.1. From additional information provided by the mapping procedure, we can compute the boundary misorientation and its various inclinations. In this way, the dependency of M' on $\mathbf{\Delta g}$ and $\mathbf{n}$—*i.e.,* $M'(\Delta g, \mathbf{n})$—can be investigated.

Such time-resolved 3D datasets are provided only by a nondestructive 3D characterization technique. Conventional 3D characterization methods like serial sectioning are able to reconstruct 3D microstructure, by they do not permit the same surface/volume to be re-observed in a time series, as the measurement technique destroys the observed region [15–19]. Owing to this limitation, efforts have been devoted to the development of nondestructive 3D characterization techniques. Since its first demonstration in 1997 [20], 3D x-ray diffraction (3DXRD) microscopy has gained steadily in popularity. This synchrotron-based x-ray imaging technique allows for the characterization of grain volume, grain shape, crystallographic orientation and elastic strain in single/multi-phase materials [21–24]. Prior to the start of this thesis work, only a limited number of measurements had focused on investigating grain growth in 4D (3D + time). The spatial

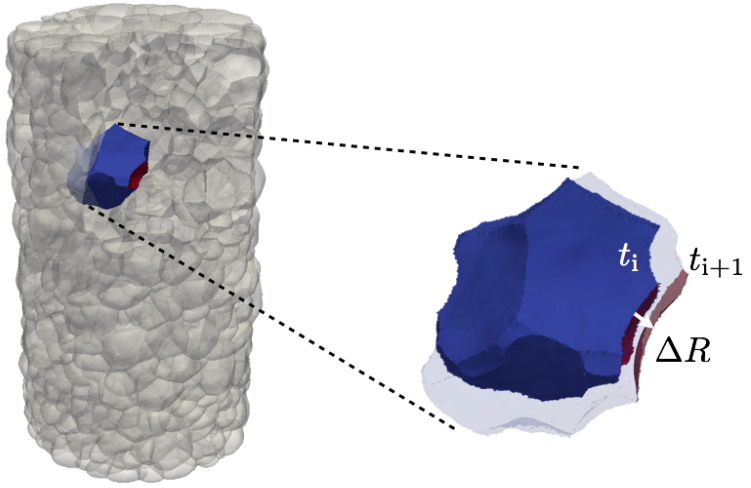

FIGURE 1.2: Illustration of the process to retrieve the reduced GB mobility from time-resolved mappings of 3D microstructure. At time t_i, the locations of GBs are mapped (left). During annealing, the grain boundaries migrate; afterwards, the location of individual GBs at t_{i+1} is determined. For example, the boundary in red of the blue grain migrates by a distance ΔR between t_i and t_{i+1}. With the curvature H estimated from the measured boundary morphology, M' can be computed for the GB from the relationship given in Eq. 1.1.

and temporal resolution that had been achieved in 3DXRD studies was not on the level of bicrystal experiments and therefore insufficient for retrieving grain boundary properties. For example, in Ref. [25], Schmidt *et al.* recorded grain growth taking place in an Al-0.1% Mn specimen, in which the number of grains dropped from 483 to 27 in a single annealing step. Such a drastic change makes it difficult to track the migration of individual GBs in a well-defined local environment. A more recent study performed by Syha *et al.* utilized a comparable synchrotron-based technique (diffraction contrast tomography), measuring the evolution of 849 grains in strontium titanate before and after one annealing step [26, 27]. Nevertheless, the analysis of these data focused on the general statistics of the grain ensemble rather than on the behavior of individual GBs.

1.1 Open questions

Aiming to extract reduced GB mobility directly from time-resolved mappings of 3D microstructure and to relate the resulting M' values to macroscopic GB parameters, my research was guided by the following open scientific questions:

1. Is it possible to retrieve the reduced GB mobility from measurements of the coarsening of grains in a polycrystalline material?

As demonstrated in Fig. 1.2, one can in principle "reverse engineer" the reduced GB mobility if a time-resolved dataset capturing the 3D evolution of microstructure is available. Nevertheless, the main challenge lies in extracting the necessary boundary parameters with sufficient accuracy. Literature shows that the estimation of boundary curvature from voxelized data is strongly affected by the pre-smoothing procedure [28, 29]. Additionally, upon annealing, grain boundaries evolve hand in hand with a change in grain size and shape, which leads to difficulty in the determination of boundary migration velocities. Therefore, the reverse engineering analysis carried out in this thesis focused on addressing these issues.

Before such an analysis can be applied to a real polycrystalline material, however, the method needs to be validated by checking it against a system in which the result (M') is a known quantity. From this perspective, a computer simulation of grain growth is an ideal starting point, as M' is usually an input parameter that governs the evolution of grains during the simulation. Moreover, validation against a simulated "ground truth" makes it possible to assess the limitations of the reverse engineering method, which mainly can be traced to the fact that certain types of GBs are not suitable for such an analysis. Unlike the boundaries in the bicrystal experiments, which can be pre-designed for convenient and accurate measurement, GBs in polycrystalline materials vary in size, curvature, shape, etc. For example, if a boundary is small in area, its curvature estimation can exhibit rather large uncertainty. Therefore, certain general conditions must be fulfilled by the GBs that go into the analysis, along with requirements placed on the spatial and temporal resolution of the experimental measurements. Finally, new 3D microstructural mappings had to be carried out in order to obtain the large number of data points needed for a proper statistical analysis.

2. Is GB curvature the primary driving mechanism for boundary migration in polycrystalline materials?

As described in Eq. 1.1, each location along a GB migrates toward the local center of curvature [6]. Computer simulations show that when GB migration is driven solely by curvature, and M' takes on the same value for all boundaries, the resulting grain growth is invariably "normal," in the sense that the grain size distribution is unimodal, and it evolves in a self-similar manner [30]. However, the GBs of real materials do not all share the same M' value. In addition, other factors beyond the capillary force could influence GB migration. For example, second-phase particles may exert a pinning force on GBs [3]. The relationship between the pinning force and the particle characteristics (*e.g.,* particle size and volume fraction) is described by the Zener equation [31]. Surface grooves and the concentration of solute elements in a material are also known to influence the speed of GB migration [32, 33]. By examining thousands of GBs in polycrystalline materials, we

will be able to determine which mechanism or mechanisms govern boundary migration in a given experimental specimen.

3. Is the reduced GB mobility determined uniquely by the macroscopic GB properties?

In the field of materials science, computer simulations play a major role in understanding materials properties and developing new materials. Compared to experiments, simulations provide a convenient foundation for testing theoretical ideas, because simulations offer the possibility for characterization and control at shorter length scales than what is experimentally accessible. In simulations of microstructural coarsening, such as vertex models [34, 35] and phase field simulations [36, 37], microstructural evolution takes place as a result of migrating grain boundaries. The boundary migration velocity is directly controlled by the GB energy and mobility, which depend on the boundary misorientation and inclination. Nevertheless, the dependency inserted into a simulation is often unphysically simplistic, which can lead to huge discrepancies between simulation results and experimental observations [38]. Even approximate models suggest that the M' of real-world materials is generally quite complex [1, 39]. Whether or not M' is a well-defined function of a GB's macroscopic degrees of freedom is thus a fundamental question that needs to be answered before computer simulations can be carried out with predictive accuracy. By reverse engineering the migration of thousands of GBs in experimental specimens, we aim to resolve this issue.

1.2 Structure of the thesis

In the next chapter, GB structure and the phenomenon of coarsening in polycrystalline materials are explained before the approaches to measuring GB energy and mobility are reviewed. Chapter 3 introduces various computational techniques that are used to simulate microstructural coarsening. The focus here is on the underlying theory as well as on the implementation of a phase field model with isotropic/anisotropic grain boundary properties. In Chapter 4, I review the working principles of 3DXRD microscopy, together with the experimental procedure and the associated data reconstruction routines. The reverse engineering *Ansatz* for retrieving reduced GB mobility from time-resolved 3D datasets is described in Chapter 5. Detailed considerations concerning the accurate estimation of boundary curvature and migration velocity are addressed, followed by validations performed on computer simulations. In Chapters 6 and 7, I present measurements of the coarsening that took place in two Al-based alloys (Al-1 wt% Mg and Al-5 wt% Cu), and I analyze the results at both the grain and grain boundary levels. The corresponding reverse engineering extraction of reduced GB mobilities is discussed

accordingly. Based on these findings, I give answers in the last chapter of the dissertation to the three open questions listed above.

Chapter 2

Coarsening in Polycrystalline Materials

2.1 Grain boundaries in polycrystalline materials

In polycrystalline materials, grains with different crystallographic orientations are separated by grain boundaries (GBs). Those boundaries play an important role in governing various mechanical and functional properties of the materials. For example, GBs serve as barriers for the movement of dislocations; thus, the more boundaries there are in a material, the higher the mechanical strength tends to be [4, 5]. Therefore, one may achieve or improve the desired properties of a polycrystalline material by manipulating the frequency or even arrangement of different types of grain boundaries. This "design and control" process is often called "grain boundary engineering" [40–44].

Nonetheless, one of the difficulties in understanding boundaries is that the parameter space describing the structure of a GB is multidimensional. Macroscopically, a GB is characterized by five degrees of freedom, involving three parameters to describe the misalignment between the two adjacent crystal lattices (misorientation) and two parameters to specify the direction normal to the boundary plane (inclination). The structure and properties of a GB are found to vary significantly with misorientation and inclination [2, 45]. On a microscopic level, there are additional degrees of freedom associated with the structure of a given GB at the atomic length scale; however, these are not the focus of this thesis.

2.1.1 Five-parameter description of grain boundaries

2.1.1.1 Misorientation

It is vital to understand the concept of orientation before discussing misorientation, as the misorientation of a GB can be derived from the orientations of the adjacent crystals. The orientation of a crystal lattice is described by means of rotation with respect to a reference frame. It is often presented using various descriptors, such as a rotation matrix, Euler angles, axis-angle pair or Rodrigues vectors [46, 47].

However, in a research paper written by Rowenhorst *et al.*, the authors drew attention to the fact that a number of different conventions appear in textbooks or are used by research groups, which makes the interpretation of orientation data troublesome, especially when converting one representation into another [48]. From my own working experience, it is very easy to make sign errors in such conversions, leading to conflicting results. Therefore, this section specifies the conventions used in this thesis and the definitions of various orientation representations. In this manner, a consistent orientation (misorientation) description is developed to describe grains measured experimentally, treated analytically or simulated on a computer.

In all orientation representations, the reference frame C_r is chosen to be right-handed and Cartesian. A rotation U brings the reference frame onto the crystal frame C_c:

$$C_c = U \cdot C_r. \tag{2.1}$$

In three dimensions, U can be represented by a 3×3 matrix. This rotation matrix is thus defined as the orientation of the crystal [46]. The rotation matrix is the fundamental way to denote the crystal orientation. Since only three entries of this matrix are independent, one can deduce other orientation representations that have more compact forms.

The most naturally intuitive representation is the axis-angle pair. Here, the corresponding rotation is described by a rotation angle θ around a specific axis $\mathbf{a}$ ($|\mathbf{a}| = 1$). The rotation angle is taken to be positive for counterclockwise rotation. A drawback of this representation is that degeneracy exists when the rotation angle approaches 0; in the latter situation, the rotation axis is ambiguous [49].

The axis-angle representation utilizes four parameters to describe an orientation.[1] The number of parameters can be reduced to three when considering the Rodrigues vector representation proposed by Frank [50]. Rodrigues vectors $\mathbf{r}$ can be derived from the

[1] In a Cartesian coordinate system, a rotation axis is described by a three-component vector, and one parameter is necessary to describe the rotation angle around the axis.

axis-angle pair, expressed as

$$\mathbf{r} = \mathbf{a} \tan\left(\frac{\theta}{2}\right). \tag{2.2}$$

Using Rodrigues vectors, the axis of rotation is represented by the direction of $\mathbf{r}$ in the Rodrigues-Frank space. Hence, rotations that have the same rotation axis lie on a straight line that passes through the origin of Rodrigues-Frank space. Meanwhile, the magnitude of $\mathbf{r}$ represents the rotation angle [51]. When close to the origin, rotation angles are smaller. Since the three components of Rodrigues vectors are independent, each contains distinct orientation information. When these components are mapped onto the RGB color space, different colors denote unique orientations. Owing to its convenience, this approach is adopted to represent grain orientations for the figures in this thesis.

Another commonly-used representation is provided by Euler angles. The latter are defined as three subsequent rotations around fixed axes. In this thesis, the Bunge convention is used—*i.e.,* the first rotation is around the z axis, the second rotation is around the x axis and the third rotation is around the z axis. The associated rotation angles $\varphi_1, \phi, \varphi_2$ are the three Euler angles [52]. According to this convention, φ_1, ϕ and φ_2 lie in the ranges $[0, 2\pi], [0, \pi]$ and $[0, 2\pi]$, respectively [52, 53].

In some cases, for example, in a computer simulation of coarsening where grain orientation plays a role, it is necessary to apply a uniform distribution of orientations to the microstructure. Such a process—namely, the generation of *a random distribution of orientations*—can utilize the approach described in Refs. [46, 54] based on Euler angles. The main steps are listed as follows:

1. Generate random numbers $x_i (i = 1, 2, 3)$ in the range [0,1].
2. Transform the first two numbers by $\varphi_i = 2\pi x_i$ $(i = 1, 2)$ to the range $[0, 2\pi]$.
3. Transform the third by $\phi = \arccos(2x_3 - 1)$ to the range $[0, \pi]$.
4. $\varphi_1, \phi, \varphi_2$ are the Euler angles of the randomly generated orientation.

Once the grain orientations are defined, the misorientation between grains can be calculated. A misorientation $\mathbf{\Delta g}$ is defined as a rotation that brings the orientation of grain A (U_A) into the orientation of grain B (U_B). Mathematically,

$$U_B = \mathbf{\Delta g} \cdot U_A. \tag{2.3}$$

Thus, $\mathbf{\Delta g}$ is calculated as

$$\mathbf{\Delta g} = U_B \cdot U_A^{-1}. \tag{2.4}$$

Similarly, besides the rotation matrix, misorientations can be expressed in different representations, as in the case of orientation. Nevertheless, it is worth mentioning that

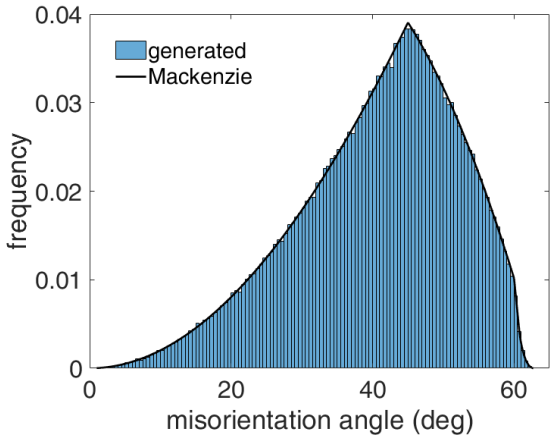

FIGURE 2.1: The histogram shows the misorientation distribution calculated from 1000 randomly generated orientations. It closely matches the theoretically derived Mackenzie distribution for the cubic symmetry system [56].

when calculating misorientations, the crystal symmetries of grain A and B must be considered. When both grains have cubic symmetry, which has 24 symmetry elements, there are $24 \times 24 = 576$ equivalent expressions for the misorientation [55]. The misorientation angle θ—sometimes called *disorientation* in the literature—is defined as the minimum angle calculated from the 576 misorientation matrices. It can be extracted from the maximum trace of all misorientation matrices using the following equation [55]:

$$\theta = \arccos\left(\frac{\mathbf{tr_{max}}\left(\Delta\mathbf{g}\right) - 1}{2}\right). \tag{2.5}$$

Taking symmetry operations into consideration, Mackenzie [56] derived the misorientation distribution for a random grain assembly. In the case of cubic symmetry, the misorientation distribution is described by the piecewise function plotted in Fig. 2.1. The misorientation angle has maximum probability at 45°. On the same plot, the misorientation distribution of orientations generated randomly following the procedure described above is compared. It is clear that the algorithm successfully generates the desired random distribution. For other crystal symmetries, the misorientation distributions have been derived in Refs. [57–59].

2.1.1.2 Inclination

Misorientation describes the misalignment of the crystal lattices of two adjacent grains, but it says nothing about how the boundary is oriented between the grains. In Figs. 2.2 (a) and (b), the upper and lower grains have orientations U_A and U_B, respectively. The boundary misorientation is the same, $\Delta\mathbf{g}_{AB}$, in both cases; however, the boundaries are oriented differently. The boundary plane orientation—namely, inclination ($\mathbf{n}$)—can be

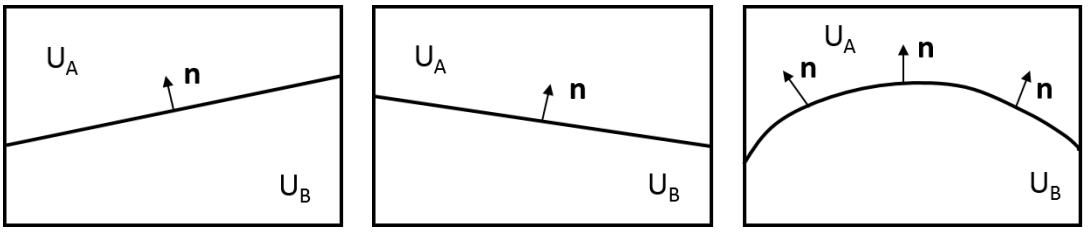

(a) (b) (c)

FIGURE 2.2: Boundaries with the same misorientation $\Delta\mathbf{g}_{AB}$ in (a) and (b) have different inclinations $\mathbf{n}$. The inclination varies along the boundary in (c).

specified by the boundary's normal vector. It is worth mentioning that the inclination may exhibit a greater complexity in a real microstructure than in the case of Figs. 2.2 (a) or (b), as a single grain boundary may consist of many differently oriented plane segments. In the two-dimensional case shown in Fig. 2.2 (c), the inclination $\mathbf{n}$ varies with location along the boundary.

A complete description of boundary inclination must take into account the fact that the boundary orientation has different indices when described in the coordinate systems of the grains on either side of the GB [60]. Hence, the calculation of boundary inclination requires the following procedure:
1. The boundary plane normal is acquired in the specimen reference coordinate system C_r.
2. The orientations of the grains that abut the boundary are acquired in the same C_r.
3. The boundary inclination is calculated from the normal vector expressed in the coordinate systems of the two adjacent grains, yielding two different expressions for the same inclination.

Fig. 2.3 illustrates a simple example for such calculations. A cubic grain is embedded in a spherical grain. The reference coordinate system is Cartesian, and the x, y, z-axes are shown in red. The orientation of the cubic grain is defined as 0, as the coordinate system of the cubic grain is perfectly aligned with the reference frame. The orientation of the spherical grain is constructed by rotating the reference frame by $-45°$ about the [001] direction. The resulting coordinate system of the spherical grain is shown in green in Fig. 2.3 (a). Now we consider one of the boundaries between the cubic grain and the spherical grain: the (100) plane. For calculation of its inclination, the normal direction of the boundary, [100], is expressed in both crystal frames. The result is shown in the [001] pole figure of Fig. 2.3 (b) using an equal-area projection. It has two poles: the [100] pole comes from the plane normal with respect to the cubic grain's frame; the [110] pole is the plane normal expressed in the spherical grain's coordinate system.

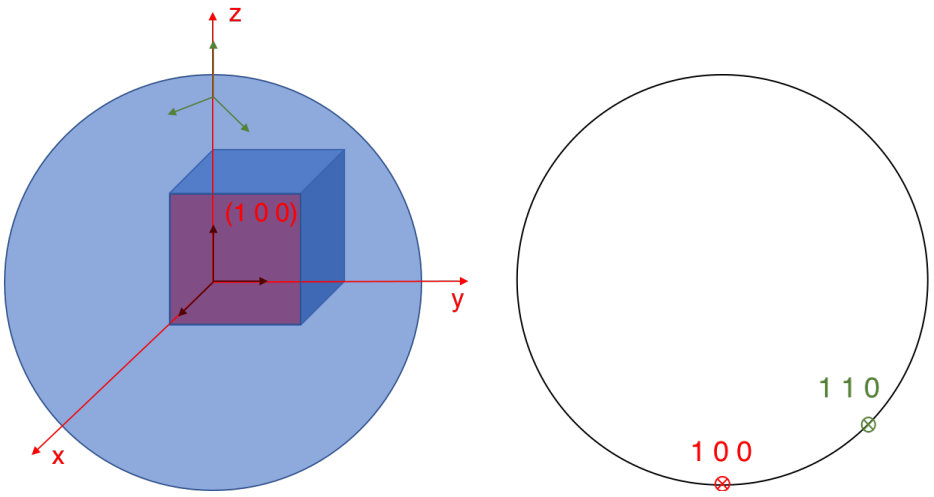

FIGURE 2.3: (a) A cubic grain embedded in a spherical grain having a different orientation. The inclination of the (100) plane boundary is calculated and shown in (b) with respect to the cubic grain's frame (red axes) and the spherical grain's coordinate system (green axes).

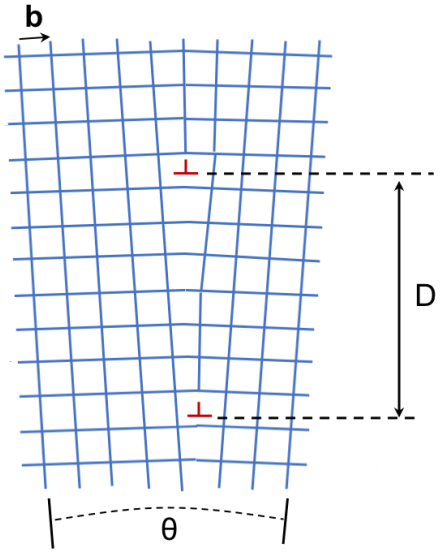

FIGURE 2.4: Representation of a low-angle tilt grain boundary between grains with misorientation angle θ. The dislocations (red) with Burgers vector $\mathbf{b}$ are separated by the distance D given by Eq. 2.6.

2.1.2 Structure of grain boundaries

2.1.2.1 Low/High-angle grain boundaries

Based on the five-parameter description of grain boundaries, boundaries in polycrystalline materials can be categorized into different types. One of the most common categorizations is low *vs.* high misorientation angle θ. For low-angle grain boundaries

(LAGBs), since the misorientation angle between two adjacent grains is small, the boundary can be treated as an array of dislocations [61, 62]. The simple case of a symmetric tilt boundary is shown in Fig. 2.4. When the crystal lattices on either side of the boundary are misoriented with angle θ, the distance between the dislocations D can be derived from the Burgers vector $\mathbf{b}$ and the angle θ [63]:

$$D = \frac{\|\mathbf{b}\|}{2\sin\left(\frac{\theta}{2}\right)}. \tag{2.6}$$

When θ is small, the above equation can be rearranged into,

$$\frac{b}{D} \approx \theta. \tag{2.7}$$

The energy of LAGBs is proposed by Read and Shockley [61]. In their dislocation model, as the boundary misorientation increases, the spacing between dislocations becomes smaller, according to Eq. 2.7. This leads to a higher dislocation density and, consequently, a higher boundary energy. The relation between the boundary energy γ and the misorientation angle θ is given as

$$\gamma = \gamma_0 \cdot \theta \left(A - \ln\theta\right), \tag{2.8}$$

where γ_0 and A are constant values dependent on the elastic properties of the given material.

The Read-Shockley model does not hold when θ is too large, as the dislocation cores begin to overlap under this circumstance. Such boundaries are termed high-angle grain boundaries (HAGBs). Compared to LAGBs, HAGBs are often found to have higher energy [3, 8]. A simple approximation for the boundary energy as a function of θ is

$$\gamma = \begin{cases} \gamma_m \dfrac{\theta}{\theta_m}\left(1 - \ln\dfrac{\theta}{\theta_m}\right) & \theta < \theta_m, \\ \gamma_m & \theta > \theta_m. \end{cases} \tag{2.9}$$

When $\theta < \theta_m$, the equation is just Eq. 2.8 rewritten in terms of the maximum boundary energy $\gamma_m = \gamma_0\theta_m$. From Eq. 2.8, θ_m at this point is $\exp(A-1)$. The angular limit for LAGBs, θ_m, is usually estimated to be 15° [3, 61, 64–66]. The piecewise equation (2.9) is plotted in Fig. 2.5, demonstrating the Read-Shockley relationship between the boundary energy and misorientation for both LAGBs and HAGBs.

Although HAGBs exhibit relatively high energy, some special HAGBs are reported to have significantly lower energies than general HAGBs [67, 68]. These special HAGBs are found to have higher symmetry at the atomistic level, which is described by the

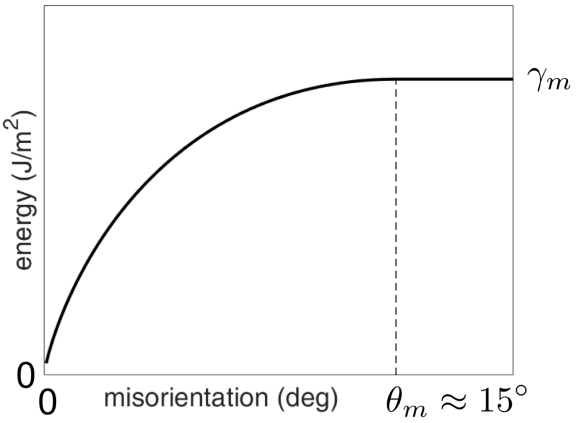

FIGURE 2.5: Grain boundary energy with respect to the boundary misorientation angle θ in the Read-Shockley approximation.

concept of the coincidence site lattice (CSL) [69]. Consider the two crystal lattices on either side of a grain boundary: one crystal lattice is now brought onto the other by translation (but not rotation) so that a maximum number of lattice points coincide. Depending on the crystallographic relation between the two crystals, the coincidence level may vary. This can be quantified by the so-called Σ value, which is defined as the ratio between the volume enclosed by a unit cell of the coincidence sites and the lattice unit cell. An example in 2D illustrating such a calculation is shown in Fig. 2.6. The lattice points of the two neighboring grains (blue and orange) are overlaid. The resulting coincidence sites are marked in green. Thus, the solid black square shows the unit cell of the coincidence sites with side length $\sqrt{m^2+n^2}$ ($m = 3$, $n = 1$). The Σ value is calculated as the ratio between the area of the solid black square and the area of the lattice unit cell; in this example, Σ is 10. However, we see that there is a smaller unit cell marked by the dashed black square. Using this unit cell, Σ is calculated to be 5. It is worth noting that, for cubic symmetry, there is always a coincidence lattice site in the center of the $m \times n$ cell when Σ is even [70]. In this circumstance, the actual Σ value is reduced by a factor of 2:

$$\Sigma = \begin{cases} \dfrac{m^2+n^2}{2} & \text{when } m^2+n^2 \text{ is even} \\ m^2+n^2 & \text{when } m^2+n^2 \text{ is odd} \end{cases} \tag{2.10}$$

From Eq. 2.10, it is clear that Σ can only be odd for cubic lattice symmetry.

All boundaries can be associated with a Σ value. However, when a general boundary manifests no special symmetry of atomic arrangements, Σ can be extremely large. For this reason, only small Σ boundaries are considered, as they are the only ones that potentially exhibit special boundary properties. In this thesis, I consider CSL boundaries

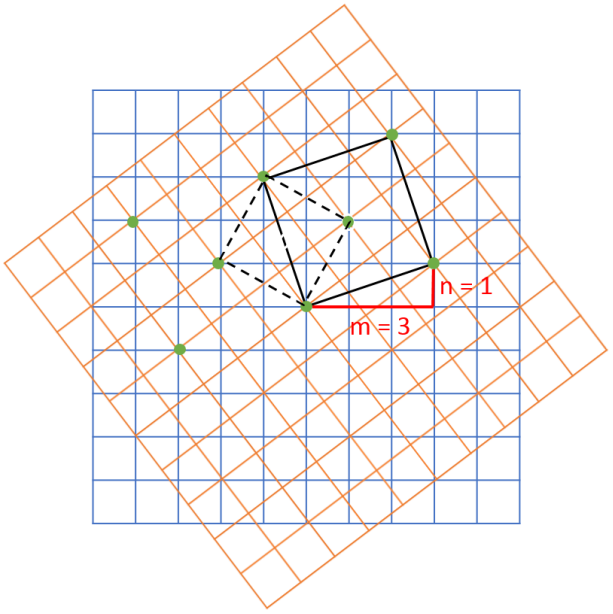

FIGURE 2.6: Schematic of a Σ5 boundary between 2D grains having a square lattice. The coincident sites between the blue and orange lattice are marked in green.

with Σ up to 23. From its construction, each type of CSL boundary can be associated with one (or more) misorientation(s). For example, a Σ3 boundary can be described by the angle-axis pair 60°/[111]. For the detailed correspondence of CSL boundaries with their misorientation representations, readers are referred to Ref. [3]. Note that certain types of CSL boundaries can be achieved by more than one type of misorientation. Up to Σ23, the following boundaries have two different misorientation types: $\Sigma 13, \Sigma 17, \Sigma 19$ and Σ21.

A boundary that deviates from the exact CSL definition by a small angle $\delta\theta$ may still exhibit the same properties as those of the CSL boundary. This proximity is expected to be related to the periodicity of the CSL boundary. In 1966, Brandon [71] quantified the notion of proximity, which is nowadays known as the Brandon criterion:

$$\delta\theta = \frac{\theta_m}{(\Sigma)^{1/2}}, \tag{2.11}$$

in which θ_m is the angular limit for LAGBs in Eq. 2.9. Within the angular range of $\pm\delta\theta$ with respect to the specified Σ boundary, such boundaries are also considered to be CSL-type boundaries.

Although CSL boundaries are a special kind of HAGB, CSL boundaries still exist in a random grain assembly. The frequencies of their occurrence in a system where the misorientation distribution follows the Mackenzie type were calculated by Morawiec [72]. If the orientation-space volume of a CSL boundary that is confined by the Brandon

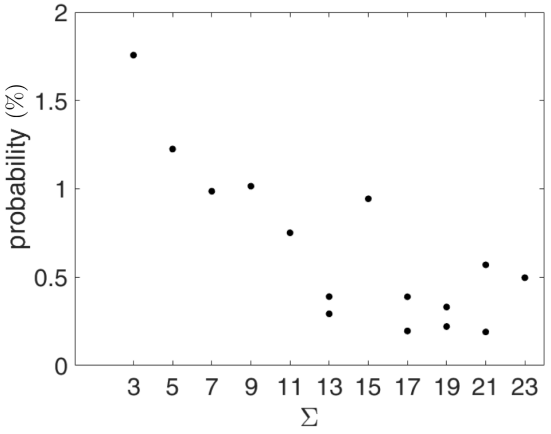

FIGURE 2.7: Frequencies of occurrence of CSL boundaries up to $\Sigma = 23$ in a random grain assembly.

criterion is divided by the volume of the entire orientation space, the fraction of each possible CSL boundary can be calculated and plotted as in Fig. 2.7.

2.1.2.2 Tilt/twist grain boundaries

The classification of boundaries based on misorientation was discussed in the previous section. When boundary inclinations are taken into consideration, boundaries can be categorized into tilt and twist type. If the boundary plane normal is parallel to the misorientation axis, the boundary is a twist type; if the boundary plane normal is perpendicular to the misorientation axis, the boundary is a tilt type. Most boundaries in a polycrystal manifest a mixed character of both types. Decomposition of a mixed boundary into tilt/twist components can follow from the routine described in Refs. [2, 73].

It is worth noting that the classification of CSL boundaries into coherent/incoherent types is also related to the boundary inclination. The term coherent refers to the complete match of atoms at the boundary. For example, consider a twin boundary ($\Sigma 3$ boundary) whose misorientation is $60°/[111]$ in angle/axis notation.[2] When the boundary normal is parallel to the misorientation axis [111], such twin boundaries are found to be coherent, whereas all other types of twin boundaries are incoherent. The coherent twins are reported to have extremely low boundary energy [8].

[2] A twin boundary can be considered to be a twist boundary ($60°/[111]$ in angle-axis representation) or a tilt boundary ($70.53°/[110]$ in angle-axis representation) [3]. Here, I consider the angle-axis pair that has the minimal misorientation angle, namely, $60°/[111]$.

2.1.3 Grain boundary energy and its measurement

Grain boundary energy is defined as the excess free energy (per unit area) associated with the presence of a grain boundary. As discussed in Sec. 2.1.2.1, the energy of LAGBs is well described by the Read-Shockley model. In this model, a grain boundary is represented by a collection of dislocations; thus, the boundary energy is the sum of the energy of the individual dislocations. The energy of LAGBs increases with increasing misorientation. Compared to LAGBs, HAGBs usually have higher energy. However, for CSL boundaries, Brandon [71, 74] suggested that they have lower energies than general boundaries, owing to symmetries. Some experimental studies [67] have reported the presence of "cusps" in the energy profile corresponding to CSL boundaries. Nevertheless, Rohrer [8] claimed in a review paper that the CSL Σ value is not a reliable criterion for predicting the boundary energy, judging from various experimental results. This view is also supported by calculations of boundary energy from atomistic simulations. In Refs. [75, 76], the authors found that there is no correlation between the boundary energy and the Σ value for their calculations of boundary energy in both FCC and BCC materials.

To measure grain boundary energy experimentally, it often necessary to measure the spatial arrangement of boundaries. Specifically, at thermodynamic equilibrium, the interfacial force at a triple line should fulfill the Herring equation [77],

$$\gamma_i \vec{t_i} + \frac{\partial \gamma_i}{\partial \theta} \vec{n_i} = 0 \text{ for } i = 1, 2, 3. \tag{2.12}$$

The parameters in the above equation can be understood from the schematic boundary geometry shown in Fig. 2.8 (a), in which three boundaries GB 1, GB 2 and GB 3 meet at a triple line that extends perpendicular to the plane of the schematic. γ_i in Eq. 2.12 refers to the boundary energy of GB i ($i = 1, 2, 3$), respectively. Force balance must be fulfilled in both the tangential $\vec{t_i}$ and normal $\vec{n_i}$ directions with respect to the boundaries. The normal force, often called a torque, results from boundary energy anisotropy, which can be quantified by the derivative of the energy with respect to the misorientation angle θ.

When boundary energies are nearly isotropic, the torque terms are small enough to be ignored. In this case, Eq. 2.12 can be simplified into the following form,

$$\frac{\gamma_1}{\sin \alpha_1} = \frac{\gamma_2}{\sin \alpha_2} = \frac{\gamma_3}{\sin \alpha_3}, \tag{2.13}$$

where α_1, α_2 and α_3 denote the dihedral angles between the boundaries, as shown in Fig. 2.8 (a). This simplified form is usually referred to as Young's equation [78, 79].

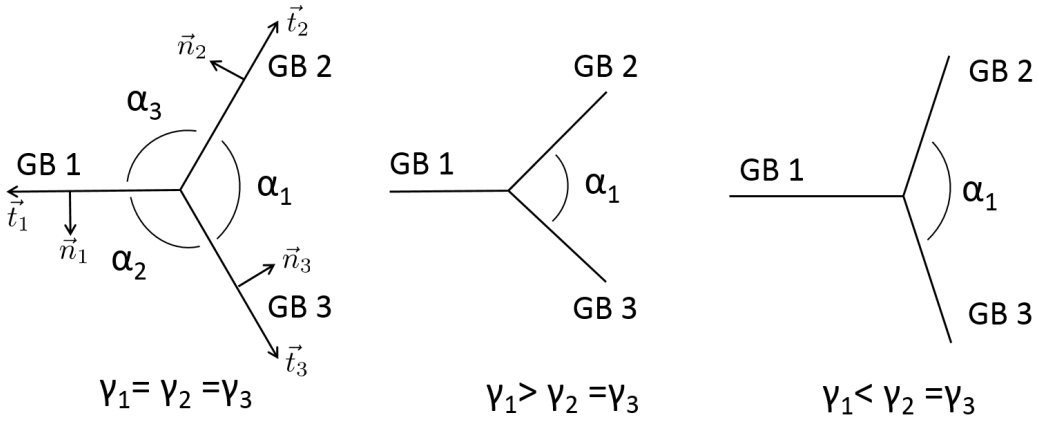

FIGURE 2.8: (a) Three grain boundaries meet at the triple line that is perpendicular to the plane of the diagram. $\vec{n}_i$ and $\vec{t}_i$ $(i = 1, 2, 3)$ denote the normal and tangential vectors to GB i. When $\gamma_1 = \gamma_2 = \gamma_3$, the corresponding dihedral angles α_1, α_2 and α_3 are equal to 120°. (b) When $\gamma_1 > \gamma_2 = \gamma_3$, the angle between GB 2 and GB 3, α_1, is smaller than 120°. (c) When $\gamma_1 < \gamma_2 = \gamma_3$, α_1 is larger than 120°.

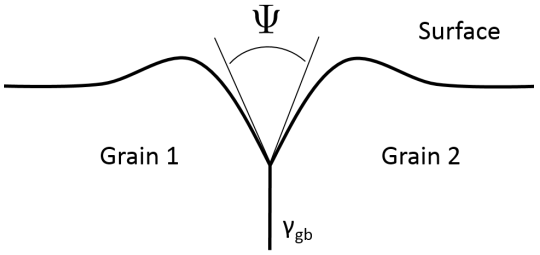

FIGURE 2.9: A thermal groove forms when a grain boundary meets a free surface. From the opening angle of the groove Ψ and the free surface energy γ_s, a value for the grain boundary energy γ_{gb} can be estimated.

When the three boundaries have the same boundary energy ($\gamma_1 = \gamma_2 = \gamma_3$), $\alpha_1 = \alpha_2 = \alpha_3 = 120°$ (Fig. 2.8 (a)). The dihedral angles change when the energy relationship between the boundaries changes. For example, when $\gamma_1 > \gamma_2 = \gamma_3$, α_1 calculated from Eq. 2.13 is smaller than 120° (Fig. 2.8 (b)); when $\gamma_1 < \gamma_2 = \gamma_3$, α_1 is larger than 120° (Fig. 2.8 (c)). From a thermodynamic perspective, if one boundary has higher energy, it will pull the triple line along its tangent to reduce its contribution to the force balance at the triple line. If the energy of this boundary is high enough, it will eventually be replaced by the other two boundaries of lower energies. A phenomenon called solid-state wetting takes place when the boundary energies fulfill $\gamma_1 > \gamma_2 + \gamma_3$ [80, 81].

Employing Young's equation, we can retrieve the relative energies of the boundaries meeting at a triple line if the dihedral angles are known. The dihedral angles can be extracted from the measured triple junction geometry. One of the most common approaches takes advantage of thermal grooving. A schematic of a thermal groove is shown in Fig. 2.9, where a grain boundary meets a free surface; such grooves form upon the heat treatment of a material. If the surface energy is known to be γ_s, the boundary

energy can be derived from Eq. 2.13 as

$$\gamma_{gb} = 2\gamma_s \cos\left(\frac{\Psi}{2}\right), \tag{2.14}$$

where Ψ is the opening angle of the groove, which can be estimated from the groove geometry as measured by atomic force microscopy [82]. Correlating such grooves with an EBSD map of the surface microstructure, Saylor *et al.* [83] observed that grain boundaries with small misorientation angles tend to have shallow thermal grooves and, accordingly, relatively low boundary energies.

However, it is not possible to evaluate the energy anisotropy accurately without using the complete form of Eq. 2.12 [8]. Morawiec [84] has developed an approach using the Hoffman-Cahn formalism of the capillarity vector to solve the Herring equation numerically on every segment of the triple lines of a boundary network. Using this technique, the relative boundary energy has been extracted for various metals and ceramics, for example in steel [85, 86], Ni [87], MgO [88] and Y_2O_3 [89]. More recently, an improved technique based on Morawiec's approach using a non-parametric reconstruction method was proposed in Ref. [90]. The authors claim that the new method is better able to deal with the situation in which only a small number of triple junctions lie within one bin of the five-parameter space, generating smaller errors compared to Morawiec's method.

It is worth mentioning that one of the main findings of boundary energy calculations based on 3D maps has been that the boundary energy is inversely correlated with the boundary-type population [7, 8, 88, 91, 92]. That is to say, boundary types that occur with higher relative frequency have lower energies, and vice versa. Nevertheless, in Refs. [93, 94], the authors compare the energy calculated by Morawiec's method with the results from their atomistic simulations, concluding that such an inverse relationship is strong for boundary types that have a high frequency of occurrence, but the inverse relationship is not apparent for infrequent boundary types, owing to poor statistics.

2.1.4 Grain boundary mobility and its measurement

In the classic model of boundary migration proposed by Burke and Turnbull, the grain boundary energy γ together with the boundary curvature H generate a net pressure P that drives boundary migration [6]:

$$P = \gamma H. \tag{2.15}$$

The boundary velocity v is assumed to be linearly proportional to P, $v = MP$. Combining the latter with Eq. 2.15, we obtain

$$v = M\gamma H, \tag{2.16}$$

in which the proportionality factor M is called the boundary mobility. Generally, M is found to exhibit an Arrhenius-type dependence on temperature,

$$M = M_0 \exp\left(-\frac{Q}{RT}\right), \tag{2.17}$$

where M_0 is a temperature-independent prefactor, Q is the activation energy for boundary migration, R is the universal gas constant and T is the absolute temperature. The activation energy Q varies from boundary to boundary, depending on boundary properties like crystallographic misorientation and chemical composition, which, in turn, leads to anisotropy in boundary migration. For example, in Ref. [95] the authors measured a discrete step-change in Q at the transition from LAGBs to HAGBs.

Differing from the measurement of boundary energies, which is carried out on static structures, the experimental measurement of boundary mobility is usually complicated, as it requires tracking a boundary over time. Boundary migration is a function of three parameters, as given in Eq. 2.16. While watching a boundary migrate at a velocity v, one can extract the product of M and γ if the boundary curvature H is known from the boundary morphology. The product of M and γ is usually referred to as the "reduced mobility" and denoted by M'.

In this section, I describe techniques that allow for efficient determination of the reduced mobility from measurements of boundary migration. One of the most successful methods is the so-called bicrystal technique [1], where two single crystals are fabricated in such a way that the boundary between them can migrate under either an internal driving force or an external driving force. Different types of bicrystal configurations are discussed in the following section.

2.1.4.1 Capillary-driven boundary migration technique

Owing to the curvature exhibited by the grain boundary inside a bicrystal, the boundary moves toward its center of curvature. Different configurations are presented in the 2D schematics of Fig. 2.10. Fig. 2.10 (a) shows the simplest "wedge" configuration. Considering Eq. 2.15, Grain 2 shrinks under the driving force $P = \gamma/R$, where R is the radius of curvature of the grain boundary. This simple and direct relationship between the driving force and the displacement is easy to handle for analysis. However, as

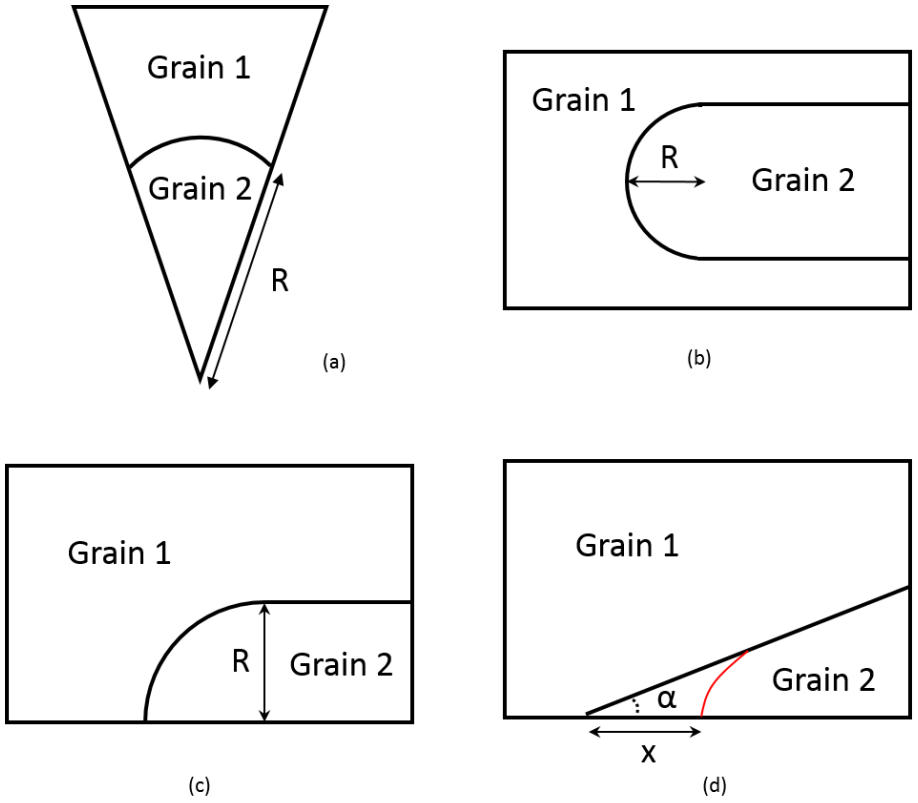

FIGURE 2.10: Different kinds of bicrystal configurations in research: (a) capillary configuration, (b,c) constant-driving force configuration, and (d) reverse capillary configuration (also known as the Sun-Bauer configuration).

R is initially large, the driving force is usually small, which often results in pinning of the microstructure. Once migration is triggered, the driving force increases with displacement of the grain boundary. Therefore, this type of bicrystal design is often named the capillary configuration.

The pinning issue is addressed by the constant-driving force configuration (Figs. 2.10 (b) and (c)). The grain boundary is designed to have a half-loop or quarter-loop shape. With the driving force γ/R, such boundaries retain their shape during steady-state motion [96]. This, in turn, keeps the driving force constant.

Another configuration is shown in Fig. 2.10(d), which has grown in popularity owing to its simpler design than the half-loop or quarter-loop, which can be difficult to achieve experimentally. First proposed by Sun and Bauer [10, 11], this bicrystal design is also named the Sun-Bauer configuration. Owing to the high curvature at the sharp point of Grain 2, the bicrystal boundary moves to the position indicated by the red curve in Fig. 2.10(d) at a later time t_1. The driving force is given by $f(\alpha)\gamma/x$, where $f(\alpha)$ is an amplification factor [1]. This driving force decreases as the displacement of the grain boundary increases. Because of its simplicity in sample preparation and the large

initial driving force, this method has been used widely to investigate grain boundary migration [10–13].

2.1.4.2 Bicrystal in a magnetic field

The driving force for boundary migration in the bicrystal configurations mentioned above is the capillary force of the structure itself. External driving forces can be applied to materials to induce boundary migration, provided the material behaves anisotropically under such a force. Bismuth (Bi) has different magnetic susceptibilities parallel and perpendicular to the trigonal axis (c-axis or $\langle 111 \rangle$-axis); thus, Bi is suitable for such an investigation. A free energy difference in the adjacent crystals will be created under an applied magnetic field, serving as the driving force for boundary migration.

Investigations on Bi were first carried out by Mullins [97]. A high-purity Bi (99.999%) bicrystal was grown by directional crystallization in a horizontal mold under Ar. The misorientation angle between the axes of two crystals was set to be 90° in order to obtain the maximal magnetic driving force. Although the misorientation has a fixed value in bicrystal-based capillary-driven techniques, the boundary inclination varies along the bicrystal boundary. In contrast, the magnetic force driven method offers an approach to investigating boundary migration with a fixed misorientation and a fixed inclination. Such a boundary exhibits no curvature, which means that no capillary force acts on it. Investigating symmetrical and asymmetrical tilt boundaries in Bi, Molodov *et al.* [98] discovered that the grain boundary mobility varied with the boundary inclination. Similar investigations were carried out in Zn under a magnetic field [99–102].

2.1.4.3 Observation of boundary migration in bicrystals

All of the techniques mentioned above require tracking the bicrystal boundary migration during heat treatment. One of the most common methods is to measure the thermal grooves that form during sample cooling, which mark the position of the grain boundary. But it is necessary to remove the grooves by mechanical polishing each time in order to suppress their influence on further boundary migration. Other measurement techniques involve utilizing the reflection of polarized light, photoemission microscopy, EBSD, XRD and x-ray topography [1].

Although the bicrystal method is popular in the investigation of boundary migration—in particular, the Sun-Bauer configuration provides valuable information on how certain types of boundaries migrate in polycrystalline materials—it is worth mentioning that the bicrystal method often requires a considerable amount of experimental effort, ranging

from the fabrication of a bicrystal with given misorientation and inclination to the measurement of grain boundary migration by microscopy. Moreover, the kinetic properties of a bicrystal boundary are reported to be quite sensitive to the bicrystal quality [14]. In some cases, grain boundaries move in a "jerky" manner purely due to surface roughness [14]. On the other hand, considering the fact that one bicrystal experiment offers insight into the behavior of boundaries with a single misorientation and certain inclination(s), using bicrystal studies to cover the entire five-parameter boundary orientation space is highly impractical. Therefore, in Chap. 5, a new approach is proposed and validated for extracting the reduced mobility directly from measurements of boundary migration in polycrystalline materials.

2.2 Grain growth

Section 2.1 describes the characteristics and migration of individual grain boundaries in a polycrystalline material. Grain growth is a collective result of grain boundary migration. In a polycrystalline material, the total free energy G is the sum of the free energy of the material when it is in the single-crystalline state, G_0, and the excess energy contributed by the boundaries,

$$G = G_0 + \gamma A_{GB}, \tag{2.18}$$

where A_{GB} is the total area of the boundaries in the system and the prefactor γ is the associated boundary energy per unit area. From a thermodynamic perspective, the driving force for grain growth is the reduction of the boundary energy term in Eq. 2.18.

Understanding individual boundary migration is vital to gaining deeper insight into grain growth. The basics of individual boundary migration are discussed in Sec. 2.1.4. As shown in Eq. 2.16, a grain boundary migrates toward its center of curvature at a velocity v [6]. When the mean curvature H is expressed as the sum of the two principal curvatures, Eq. 2.16 can be rewritten as

$$v = M\gamma \left(\frac{1}{R_1} + \frac{1}{R_2} \right), \tag{2.19}$$

where R_1 and R_2 are the local radii of curvature. Burke and Turnbull [6] averaged Eq. 2.19 over the grain ensemble of a polycrystal, arguing that $\langle R_1^{-1} + R_2^{-1} \rangle$ can be approximated by $\langle R \rangle^{-1}$, which gives

$$\frac{d\langle R \rangle}{dt} = \frac{2M\gamma}{\langle R \rangle}. \tag{2.20}$$

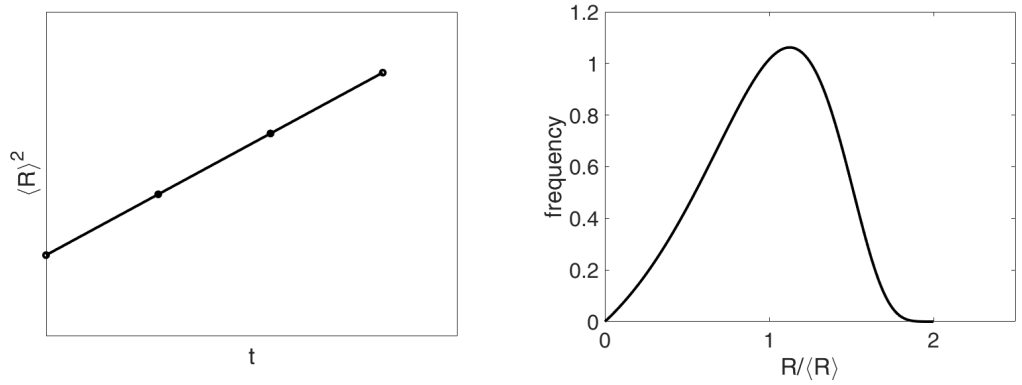

(a) (b)

FIGURE 2.11: (a) Parabolic relationship between the average grain radius $\langle R \rangle$ and the time t during normal grain growth. (b) Grain size distribution derived from mean-field theory [103]. In normal grain growth, the distribution remains time-invariant when plotted against R scaled by the average grain size $\langle R \rangle$.

The integrated form of Eq. 2.20 is

$$\langle R \rangle^2 - \langle R_0 \rangle^2 = 4M\gamma t, \tag{2.21}$$

where $\langle R_0 \rangle$ denotes the average grain radius at time $t = 0$. Plotted in Fig. 2.11 (a), it is clear that $\langle R \rangle^2$ increases linearly with time. This relation is known as the parabolic law of grain growth.

In 1965, Hillert derived a mathematical description of the curvature-driven growth of grains in a polycrystal in which each grain is embedded in the same mean environment [103], also known as the mean-field approximation. In this approach, the growth rate of a grain of radius R is given by

$$\frac{dR}{dt} = \frac{M\gamma}{R}\left(\frac{R}{R_c} - 1\right), \tag{2.22}$$

in which R_c is a critical grain radius for grain growth. That is to say, when a grain is larger than R_c, the grain grows; when a grain is smaller than R_c, the grain shrinks. For grain growth in 3D, $R_c = (9/8)\langle R \rangle$, where $\langle R \rangle$ is the mean grain radius. For this growth expression, Hillert derived the distribution of grain sizes f to be

$$f = (2e)^3 \frac{3u}{(2-u)^5} e^{6/(u-2)}, \tag{2.23}$$

assuming self-similar evolution of the microstructure. In this equation, u is the normalized grain radius R/R_c. This distribution is plotted in Fig. 2.11 (b), showing a unimodal shape. If all grain boundaries in a polycrystal are isotropic in mobility and energy, microstructural evolution is purely the result of curvature flow. Such a type of growth is

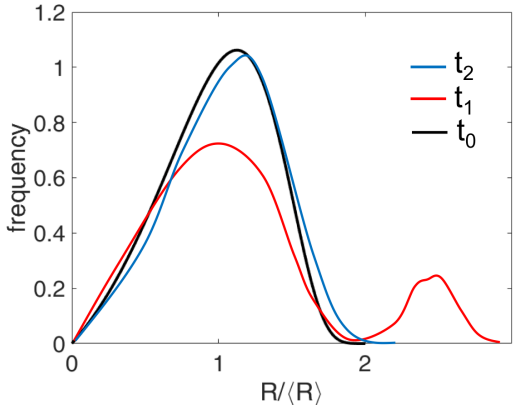

FIGURE 2.12: Evolution of the grain size distribution during abnormal grain growth ($t_0 < t_1 < t_2$).

sometimes called ideal grain growth, which is the simplest form of normal grain growth (NGG). Upon annealing, some grains grow by consumption of their smaller neighbors, leading to an increase in the average grain size $\langle R \rangle$. However, the grain size distribution retains its shape when normalized by $\langle R \rangle$ [104, 105]. The time-invariant grain size distribution is another key feature of NGG besides the parabolic growth behavior mentioned above.

2.2.1 Abnormal grain growth

During grain growth, a few grains can sometimes grow much faster than the rest. This type of growth is termed abnormal grain growth (AGG) [3]. An abnormally growing grain of radius R should fulfill the following growth rate requirement [3]

$$\langle R \rangle \frac{dR}{dt} - R \frac{d\langle R \rangle}{dt} > 0, \tag{2.24}$$

where $\langle R \rangle$ is the mean grain radius of the grain assembly. Owing to the presence of fast-growing abnormal grains, the time-invariant property of the grain size distribution in NGG is lost. The peak position may shift, and the peak width may broaden. Indeed, sometimes a bimodal size distribution can develop, provided a sufficient number of grains grow abnormally. Upon further heat treatment, the distribution can revert to a unimodal shape when large abnormal grains eventually impinge on each other (Fig. 2.12) [3].

Depending on the particular application, AGG might be desired or something to be avoided in the microstructure. For example, the abnormal growth of $110\langle 001 \rangle$ cube-oriented grains in silicon transformer steels improves the material's magnetic properties [106]. On the other hand, thanks to the large size of the abnormal grains, the

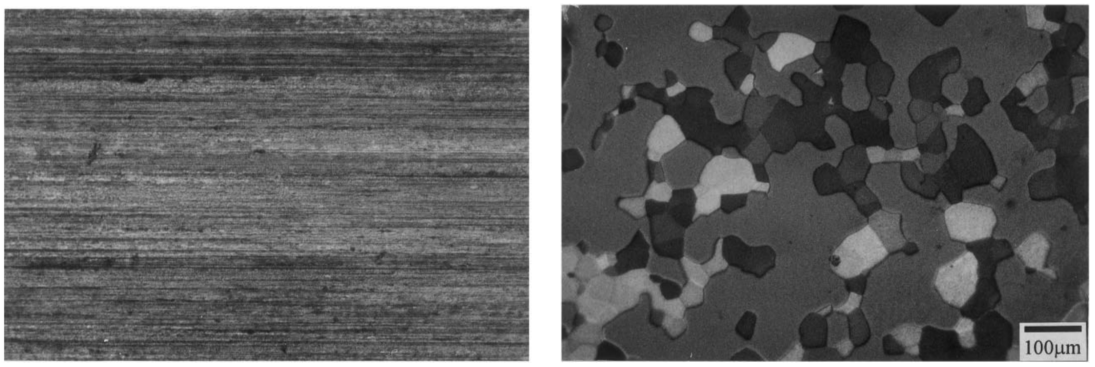

(a) (b)

FIGURE 2.13: Microstructure of a high-purity Al foil in (a) the as-rolled state and (b) after 1000 s annealing at 360°C, revealed by optical microscopy [110]. Reprinted from Materials Science and Engineering: A, 271, O. Engler and M.-Y. Huh, Evolution of the cube texture in high purity aluminum capacitor foils by continuous recrystallization and subsequent grain growth, 371-381, Copyright 1999, with permission from Elsevier.

yield strength may be reduced according to the Hall-Petch relation. Therefore, for controlling the final microstructure, it is important to understand the physics underlying the formation of abnormal grains. The key to the latter lies in the anisotropy of grain boundary energy and mobility [107–109]. In the remainder of this section, I will discuss two main factors (texture and second-phase particles) that give rise to large anisotropy in boundary properties, which can eventually lead to the occurrence of AGG.

During the processing of materials, grains in the final microstructure may exhibit preferred crystallographic orientations. Inside one texture component, the boundaries between grains have low misorientation. These boundaries often manifest low energy and mobility. If some grains are present with another texture component, the associated boundaries have high misorientation, resulting in higher boundary energy and mobility, which can promote the occurrence of abnormal grain growth. For example, the authors of Ref. [110] investigated the grain growth in high-purity aluminum foils. The samples were cold-rolled, of which the as-deformed state shows a typical banded microstructure (Fig. 2.13 (a)). Upon annealing at 360°C for 1000 s, numerous larger grains were found in the microstructure (Fig. 2.13 (b)). Abnormal grain growth took place, as a large number of LAGBs were found in the sample due to the retained rolling texture [110].

AGG can also take place when no strong texture is present in a material, such as when AGG is induced by the presence of second-phase particles [3]. Second-phase particles can exert pinning forces that hinder the migration of grain boundaries. The first quantitative analysis of this phenomenon was carried out by Zener in 1948 [31]. In his model, a relationship between the final grain size, the volume fraction and the size of the second-phase particles is proposed. A pinning pressure P_z arising from the particles is introduced

into the kinetics of boundary migration,

$$\frac{dR}{dt} = M\left(P - P_z\right) = M\left(\frac{\gamma}{R} - \frac{3F_v\gamma}{2r}\right), \tag{2.25}$$

where F_v denotes the volume fraction of second-phase particles of radius r. Owing to the presence of the pinning particles, grain growth will eventually stagnate when $P = P_z$. The Zener limiting grain size R_{Zener} is thus estimated to be

$$R_{\text{Zener}} = \frac{2r}{3F_v}. \tag{2.26}$$

The pinning effect of particles will have a significant influence on the kinetics of grain growth when the driving pressure for grain growth is comparable to the pinning pressure. Zener pinning describes the situation where the second-phase particles are well-dispersed in a material, which eventually stabilizes the grain boundary network. However, the spatial distribution of particles, the pinning strength and the dissolution of particles may all influence the growth kinetics dramatically [111]. If the particles are inhomogeneously distributed in a material, the pinning effect varies from location to location. This results in two populations of fast and slowly migrating boundaries. For example, in Refs. [38, 112], AGG was reported to occur in an Al-3.5 wt% Cu specimen at the annealing temperature of 480°C. The authors found that the sample was free of texture, but the fraction of the pinning phase (Al_2Cu) was much lower at abnormal grain boundaries than at matrix grain boundaries. Thanks to the weaker pinning force, the boundaries of the abnormal grains were able to reach higher migrating velocities. It is also reported that the pinning pressure may undergo a localized reduction due to the dissolution and coarsening of pinning particles [113]. Consequently, the pinned boundaries in those locations become more mobile than the rest of the boundaries, leading to the occurrence of AGG.

2.3 Ostwald Ripening

Grain growth describes coarsening in a single-phase material (or a single-phase matrix surrounding a low volume fraction of inert second-phase particles). When coarsening takes place in a multiphase system, this phenomenon is known as Ostwald ripening. In the simplest case of a binary system, particles of one phase are embedded in a matrix of a second phase. An example is shown in Fig. 2.14, in which Sn-rich solid particles are surrounded by a Sn-Pb liquid at a temperature above the eutectic. At this elevated temperature, the larger solid particles grow at the expense of the smaller particles; meanwhile, the volume fraction of the solid phase (V_V) stays constant. At the atomistic

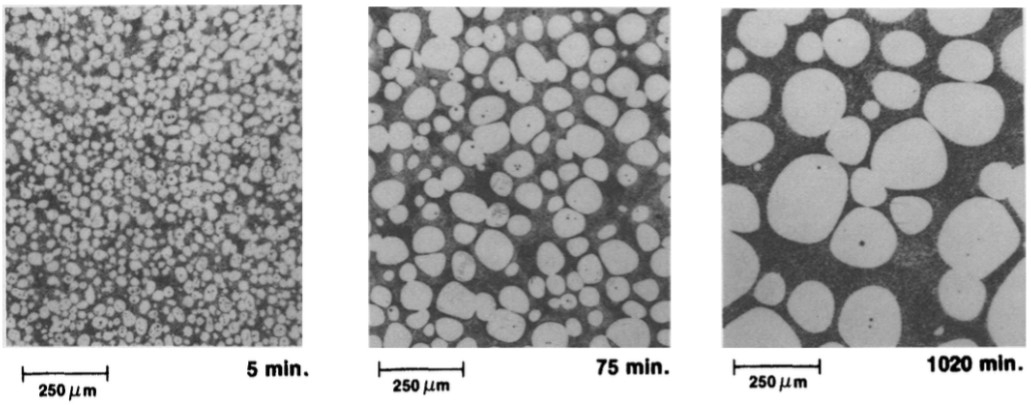

FIGURE 2.14: Example of Ostwald ripening taking place in a binary system. At 185°C, the Sn-Pb alloy consists of Sn-rich solid particles (light gray) and Sn-Pn liquid (dark gray). The average particle size of the coarsening phase increases with time, while its volume fraction remains constant at 0.64. Figures taken from Ref. [117] and reprinted by permission from Springer Nature: Springer Nature, Metallurgical and Materials Transactions A, 19, Ostwald ripening in a system with a high volume fraction of coarsening phase, S. C. Hardy and P. W. Voorhees, 2713–2721, Copyright 1988.

level, due to the Gibbs-Thomson effect, the solute concentration at the surface of smaller particles is greater than at the surface of larger particles when local equilibrium with the matrix has been established [114]. Thanks to these concentration gradients, the solute atoms from more highly curved particles dissolve into and through the matrix and attach to the less-curved (*i.e.,* larger) particles. Ostwald ripening leads to a drop in the number of particles in the system over time and to an increase in the average size of the particles. An analytic model for Ostwald ripening was developed in 1961 independently by Lifshitz, Slyozov [115] and Wagner [116]. Their model is nowadays referred to as LSW theory.

Under the assumption of a vanishing volume fraction of the coarsening phase ($V_V \to 0$), the LSW model describes the coarsening of a multiphase system in which the coarsening particles remain spherical, and there is no interaction between them. Under these conditions, the model derives a linear relation between the mean particle radius cubed and the coarsening time t,

$$\langle R \rangle^3 - \langle R_0 \rangle^3 = k(t - t_0), \tag{2.27}$$

where $\langle R_0 \rangle$ is the mean particle radius at time t_0, and k is a positive growth constant. The kinetics of Ostwald ripening differ from the parabolic growth law derived for grain growth. A cubic growth law has been observed in various experimental studies of coarsening in multiphase systems [117]. In the LSW model, the particle size distribution f is given by

$$f = \frac{1}{h_0} \frac{u^2}{(u+3)^{7/3} (3/2 - u)^{11/3}} e^{3/(2u-3)}, \tag{2.28}$$

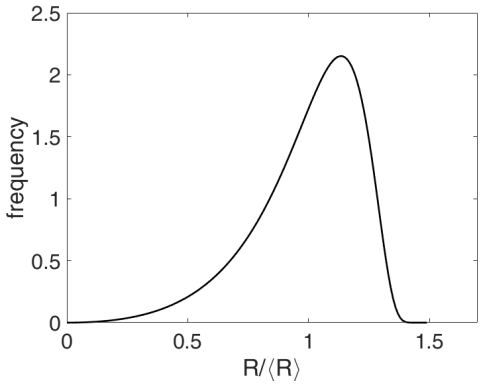

FIGURE 2.15: The distribution of particle sizes induced by Ostwald ripening, as predicted by the LSW model (Eq. 2.28).

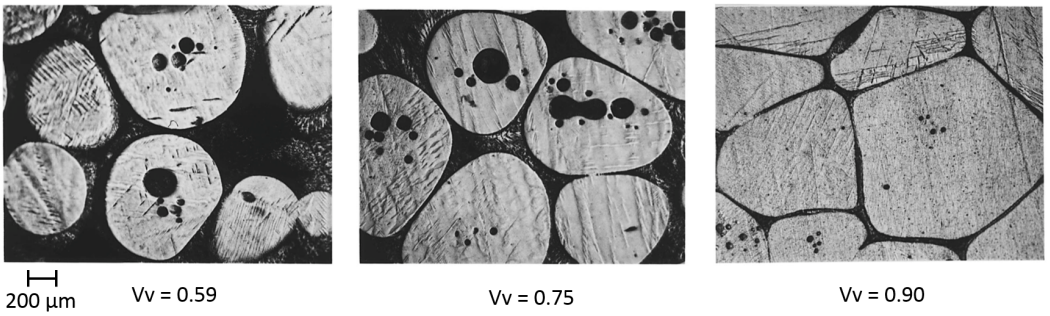

FIGURE 2.16: Microstructure of Sn-Pb alloys at various volume fractions V_V of the coarsening phase. Figures taken from Ref. [120] and reprinted by permission from Springer Nature: Springer Nature, Metallurgical and Materials Transactions A, 30, Investigation of microstructural coarsening in Sn-Pb alloys, S. K. Kailasam, M. Glicksman, S. S. Mani, and V. E. Fradkov, 1541–1547, Copyright 1999.

in which u denotes the normalized mean particle radius $R/\langle R\rangle$, and h_0 is a normalization factor equal to 0.014419 [118, 119]. This distribution is plotted in Fig. 2.15, showing a unimodal shape and a sharp drop in the frequency of large particles. Moreover, the distribution takes on a time-invariant shape during coarsening.

However, when V_V is high, the assumptions of LSW theory are no longer valid, as the interaction between particles in this situation cannot be ignored. In addition, the particle shape deviates from spherical and often exhibits a certain amount of shape accommodation, owing to geometric constraints. Figure 2.16 shows micrographs of Sn-Pb alloys at different V_V [120]. It can be seen that particles tend to have flattened interfaces with increasing V_V.

A large number of investigations have determined that the volume fraction of the coarsening phase has a great influence on the coarsening kinetics [120–124]. It is found that the resulting microstructural characteristics differ considerably from the prediction of LSW theory. For example, Rowenhorst *et al.* [122] collected 3D coarsening data in a

Pb-Sn alloy at two V_V (78% and 52% of the Sn-rich particles) using serial sectioning. The authors concluded that the particle size distributions did not follow the LSW prediction, but were in good agreement with the grain size distribution obtained from the grain growth simulation performed in Ref. [125]. Bender and Ratke [126] observed similar coarsening results in a Cu-Co system with V_V of the Co particles ranging from 0.25 to 0.7. With increasing V_V, the peak of the particle size distribution shifted to smaller sizes, resulting in a broader distribution.

Chapter 3

Computer Simulation

In addition to experimental investigations into the coarsening of polycrystalline materials, extensive efforts have been made utilizing computer simulations. This chapter first presents an introduction to simulation methods for modeling the coarsening of microstructure in three dimensions. This is followed by a detailed description of the phase field technique that is employed in this thesis to simulate microstructural evolution. Details on the implementation of this method to simulate various coarsening scenarios and the associated choice of simulation parameters are also discussed in this chapter.

3.1 Introduction to simulation methods

Many models have been developed to simulate the microstructural coarsening that occurs during recrystallization and grain growth. They mainly fall into the following categories: vertex models, Monte Carlo Potts models and phase field models [39]. Other important simulation techniques include cellular automata [127, 128] and the recently developed level set method [129–137].

Vertex models, also known as front-tracking models, are intuitively straightforward, because the model itself directly incorporates the equation for curvature-driven growth. The growth equation is directly applied to the nodes that separate a boundary into segments. However, when dealing with the vanishing of grains and the associated nodes, the vertex method runs into ambiguities that can be resolved only by implementing a complicated set of rules for reattaching boundary segments to the remaining nodes [34]. Extending the vertex method to 3D is possible but even more complicated, since tessellated surfaces must be constructed to represent grain boundaries [35, 138, 139].

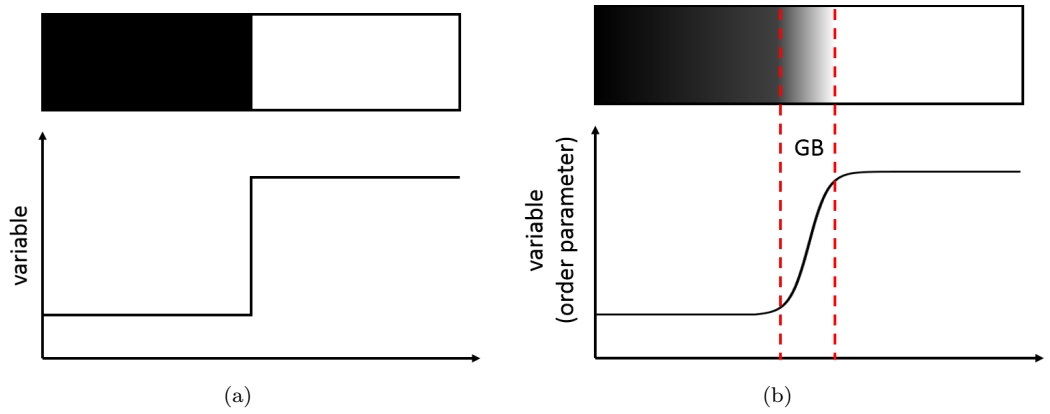

FIGURE 3.1: (a) Sharp grain boundary in vertex models, Monte Carlo Potts models, etc. (b) Diffuse grain boundary in the phase field model.

In Monte Carlo Potts models [140–143], grain boundaries are implicitly described by the spatial extent of individual grains. The model simulates grain boundary migration by the movement of kinks along the boundaries. It is a biased random walk process that gives boundary motion in agreement with the curvature-driven growth equation.

Unlike vertex and Monte Carlo models, a boundary in the phase field method is diffuse rather than sharp (Fig. 3.1 (a)). The diffuse boundaries are described by order parameters that vary smoothly across the boundary (Fig. 3.1 (b)). Moreover, instead of explicitly tracking the migration of individual boundary positions, the phase field method solves the energy-based equation that governs microstructural evolution for all positions in the system. This has an intrinsic advantage when using voxel (pixel)-based structures, avoiding pre-processing steps like the extraction of boundary locations [22]. Therefore, data from experiments such as EBSD and 3DXRD measurements, the as-collected data of which is pixel or voxel-based, can easily be incorporated into the phase field model. Owing to this feature, modeling of microstructural evolution is performed in this thesis using the phase field approach.

3.2 Phase field simulation of ideal grain growth

In the phase field model, the order parameters $\eta_i(\mathbf{r}, t)$ are functions of the spatial coordinates $\mathbf{r}$ and the time t, which may relate to the crystal structure, orientation, composition, etc. As shown in Fig. 3.1 (b), the order parameters within grains take nearly constant values, whereas they change gradually in value at the places where two neighboring grains are in contact. The position of the boundary is implicitly defined by a contour of constant values of the order parameters.

The temporal evolution of the order parameters is described by a set of partial differential equations. Different driving forces can be considered in the model, such as a reduction in bulk energy, interfacial energy or elastic energy [144]. Phase field simulation is nowadays a prevalent model that has been applied to various phenomena, such as solidification [145], recrystallization [146], grain growth [36, 37], etc. Recent improvements in computational speed and capacity allow the model to be extended to three dimensions [125, 147, 148].

The implementation of grain growth using a phase field model in this thesis is based on the method proposed by Fan and Chen [36, 37]. In a polycrystalline material, p number of grains are distinguished by the non-conserved order parameters, $\eta_i (i = 1, 2, ..., p)$. The free energy F of the system is defined as the sum of the bulk energy and the interfacial energy. In Fan and Chen's model, F takes on the form

$$F = \int_V \left[m f_0 + \sum_{i=1}^{p} \frac{\kappa}{2} \left| \nabla \eta_i \right|^2 \right] dV. \tag{3.1}$$

In this equation, V denotes the total volume of the system, and f_0 is the local free energy density of the bulk phase, associated with a strictly positive prefactor m. The energy coefficient κ is also positive, such that the gradient part yields a positive interfacial energy. In Fan and Chen's approach, f_0 is constructed in such a way that it has multiple degenerate minima at $\eta_i = \pm 1$ and $\eta_{j \neq i} = 0$:[1]

$$f_0 = \sum_{i=1}^{p} \left(\frac{\eta_i^4}{4} - \frac{\eta_i^2}{2} \right) + \gamma \sum_{i=1}^{p} \sum_{j \neq i}^{p} \eta_i^2 \eta_j^2, \tag{3.2}$$

in which γ is chosen to be 3/2 to ensure a symmetric interfacial profile [149].[2] The evolution of order parameters follows the time-dependent Ginzburg Landau (TDGL) equation,

$$\frac{\partial \eta_i}{\partial t} = -L \frac{\delta F}{\delta \eta_i}, \tag{3.3}$$

where L is a positive kinetic parameter.

3.3 Numerical solution of the phase field equations

Temporal and spatial discretization are both necessary to solve the TDGL equation numerically. We adopt a forward-difference approach for temporal discretization, owing

[1] In the phase field simulations implemented in this thesis, η is strictly non-negative. Hence, the minima of Eq. 3.2 are at $\eta_i = 1$ and $\eta_{j \neq i} = 0$.

[2] The symbol γ should not be confused with grain boundary energy, which, in the phase field literature, is represented by the symbol σ.

to its simplicity. In this case, the left-hand side of Eq. 3.3 can be written as

$$\frac{\eta\left(\mathbf{r}, t_{n+1}\right) - \eta\left(\mathbf{r}, t_n\right)}{\Delta t_s}. \tag{3.4}$$

In an explicit approach like this one, the time step Δt_s must be kept small in order to maintain numerical stability. In the simulations implemented in this thesis, Δt_s was set to the value 0.01.

Spatially, the continuous order parameters must be projected onto a finite grid. The Laplace operator in F on the right-hand side of Eq. 3.3 is calculated using the first-order central difference. In the end, the discretized form of Eq. 3.3 is

$$\begin{aligned}
&[\eta(\mathbf{r}, t_{n+1}) - \eta(\mathbf{r}, t_n)]/\Delta t_s = \\
&- L\{\partial f_0/\partial\eta(\mathbf{r}, t_n) - \kappa[\eta(\mathbf{r}_{x-1,y,z}, t_n) + \eta(\mathbf{r}_{x+1,y,z}, t_n) + \eta(\mathbf{r}_{x,y-1,z}, t_n) + \eta(\mathbf{r}_{x,y+1,z}, t_n) \\
&\qquad + \eta(\mathbf{r}_{x,y,z-1}, t_n) + \eta(\mathbf{r}_{x,y,z+1}, t_n) - 6\eta(\mathbf{r}_{x,y,z}, t_n)]/(\Delta h)^2\}
\end{aligned} \tag{3.5}$$

For the spatial discretization, Δh should be chosen fine enough to resolve the boundary profile. Literature sources have reported that the boundary width should be at least four times Δh to yield reasonable simulation results [150, 150, 151]. Following this rule of thumb, Δh in this study was set equal to one-fourth of the boundary width used in the simulations.

In the phase field model, each grain ideally has a unique order parameter. If this is not the case, coalescence will occur when two grains of the same order parameter come into contact, thereby forming a single large grain almost instantaneously. This phenomenon leads to incorrect growth kinetics and unphysical grain shapes [125]. In light of the fact that the simulation allocates memory for p order parameters at each grid point in the simulation cell, if p is set to equal to the total number of grains, the simulation will require an enormous amount of the memory simply to store the order parameters. In addition, computing the order parameters for the TDGL is time-consuming. In order to address these issues, several methods have been proposed, including local reassignment of grain labels [125], a sparse data structure [147, 152, 153], and the implementation of a bounding-box algorithm [154]. The sparse data structure was adopted for the phase field algorithm used in this thesis. As there are only a few order parameters that take on value close to 1 in the vicinity of any given grain boundary, the TDGL equations need only to be solved for the order parameters whose values exceed a small threshold. In the current work, a threshold of 0.001 resulted in a suitable trade-off between obtaining the correct growth kinetics and reducing memory requirements for data storage.

As mentioned above, Δt_s should be set small enough to maintain stability of the calculation. Consequently, the phase field method usually requires a large amount of computational time to simulate significant growth in the microstructure. In order to lower the overall run time, simulations are nowadays carried out on high-performance clusters that exploit parallel computing techniques using Message Passing Interface (MPI) [155] and a graphics processing unit (GPU) [151, 156–161]. In this thesis work, a CUDA-accelerated simulation was implemented on a GPU (GeForce GTX TITAN X) [162].

3.4 Grain growth with anisotropic boundary properties

In the phase field model, the boundary energy and mobility are defined implicitly by the phenomenological parameters that appear in Eqs. 3.1, 3.2 and 3.3. The main difficulty for implementing the phase field method with anisotropic boundary properties is that the diffuse boundary width does not stay constant when the phenomenological simulation parameters are changed [163]. A non-constant boundary width results in nonuniform stability and accuracy conditions for the numerical solution. Starting from Fan and Chen's model, Moelans [149] proposed a method that can vary the phenomenological parameters according to desired values for the boundary mobility and energy while keeping the boundary width constant. In this section, I present the main quantities and computations that must be carried out to implement Moelans's approach. The relationship between the phase field phenomenological parameters m, γ, κ and L on the one hand, and the boundary energy and boundary mobility on the other, is thereby revealed. Using such a relationship, some aspects of the macroscopic description of grain boundaries can be incorporated into the simulation, such as the misorientation angle. Nevertheless, the boundary inclination cannot be considered by the phase field model used in this thesis due to infeasibility of tracking the local boundary normal.

For the sake of simplicity, the derivation is based on a two-grain system. As shown in Fig. 3.2, grains i and j form a grain boundary. The boundary energy $\sigma_{i,j}$ can be calculated from Eq. 3.1:

$$\sigma_{i,j} = \int_{-\infty}^{+\infty} \left\{ m f_0 \left(\eta_i, \eta_j\right) + \frac{\kappa_{i,j}}{2} \left[\left(\frac{d\eta_i}{dx} \right)^2 + \left(\frac{d\eta_j}{dx} \right)^2 \right] \right\} dx, \tag{3.6}$$

where x denotes the direction perpendicular to the grain boundary. The order parameters η_1 and η_2 take on the profiles shown in Fig. 3.2 when the boundary is in equilibrium. Under such a condition, the functions $\eta_i(x)$ and $\eta_j(x)$ that minimize the right-hand side

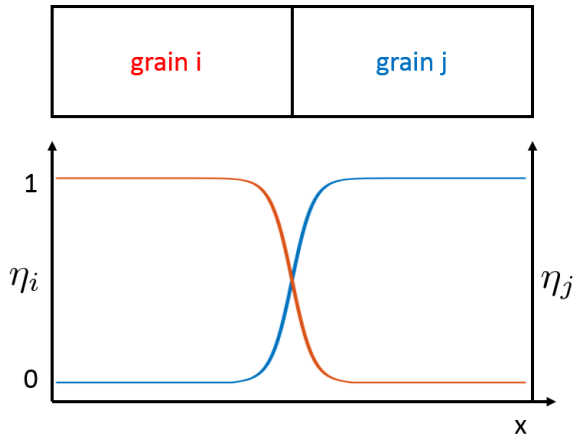

FIGURE 3.2: In a two-grain system, the order parameters η_i and η_j change gradually across the boundary.

of Eq. 3.6 can be calculated according to the Euler-Lagrange equation:

$$m\frac{\partial f_0}{\partial \eta_i} - \kappa_{i,j}\left(\frac{d^2\eta_i}{dx^2}\right) = 0, \tag{3.7}$$

$$m\frac{\partial f_0}{\partial \eta_j} - \kappa_{i,j}\left(\frac{d^2\eta_j}{dx^2}\right) = 0. \tag{3.8}$$

Integration of both equations yields

$$mf_0 - \frac{k_{i,j}}{2}\left[\left(\frac{d\eta_i}{dx}\right)^2 + \left(\frac{d\eta_i}{dx}\right)^2\right] = 0. \tag{3.9}$$

Combining Eq. 3.6 and 3.9, the boundary energy can be expressed as

$$\sigma_{i,j} = 2m\int_{-\infty}^{+\infty} f_0\left(\eta_i, \eta_j\right) dx. \tag{3.10}$$

The independent variable x can be changed to η. The above equation then takes the form [149]

$$\sigma_{i,j} = g\left(\gamma_{i,j}\right)\sqrt{\kappa_{i,j}m}. \tag{3.11}$$

The analytical solution of $g(\gamma_{i,j})$ in the above equation is rather complicated [149]. Thus, in order to solve $g(\gamma_{i,j})$ numerically, various $\gamma_{i,j}$ values are tested for coarsening of the two-grain system. The quantity $g(\gamma_{i,j})$ can be extracted from the calculated boundary energy using Eq. 3.10 and the simulation input parameters $\kappa_{i,j}$ and m. Fig. 3.3 shows the resulting values of g as a function of γ. These values are fit by a high-order polynomial for further usage.

When γ is varied, boundary profiles change accordingly. In Fig. 3.4 (a), boundary profiles are plotted for different values of γ. Note that only when $\gamma = 1.5$ is the boundary

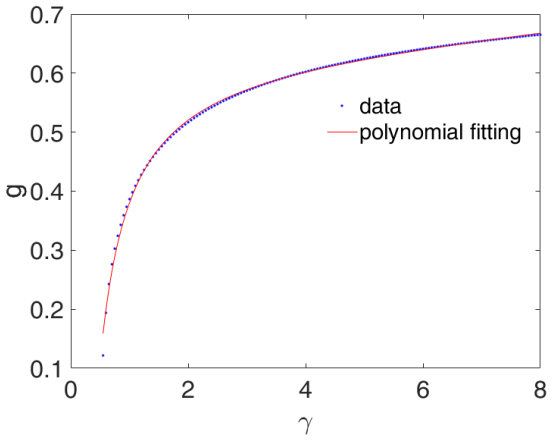

FIGURE 3.3: Numerically calculated function g of γ is fitted by a high-order polynomial.

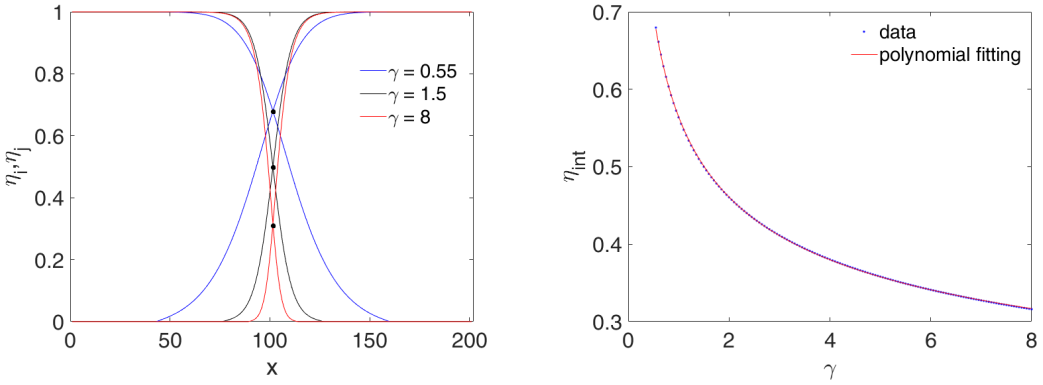

(a) (b)

FIGURE 3.4: (a) Boundary profiles for the coarsening of two grains for different values of γ. The intersection η_{int} is marked by a solid dot. (b) η_{int} expressed as a function of γ, as derived from (a).

profile symmetric, as shown by the intersection of the two order parameters, η_{int}, at the value 0.5. Figure 3.4 (b) demonstrates the dependence of η_{int} on γ. The associated energy $f_{0,int}$ is calculated from Eq. 3.2,

$$f_{0,int} = 2\left(\frac{\eta_{int}^4}{4} - \frac{\eta_{int}^2}{2}\right) + \gamma\eta_{int}^4 + \frac{1}{4}. \tag{3.12}$$

In Moelans' approach, the boundary width l_{gb} is defined as

$$l_{gb} = \frac{1}{|(d\eta_i/dx)_{x=0}|} = \frac{1}{|(d\eta_j/dx)_{x=0}|} = \sqrt{\frac{\kappa_{i,j}}{m f_{0,int}}}. \tag{3.13}$$

When $\gamma = 1.5$ (the case of symmetric boundary profile), l_{gb} is calculated to be $\sqrt{\frac{8\kappa_{i,j}}{m}}$.

From the boundary migration velocity in the Hillert grain growth model and the phase

field model, Fan and Chen [36, 37] derived the connection between the grain boundary energy σ, the mobility M and the phenomenological phase field parameters κ and L:

$$\sigma M = \kappa_{i,j} L_{i,j}. \tag{3.14}$$

Combination of Eqs. 3.10, 3.13 and 3.14 gives

$$\kappa = \sigma l_{gb} \frac{\sqrt{f_{0,int}(\gamma)}}{g(\gamma)}, \tag{3.15}$$

$$L = \frac{M}{l_{gb}} \frac{g(\gamma)}{\sqrt{f_{0,int}(\gamma)}} \tag{3.16}$$

$$\text{and } m = \frac{\sigma}{l_{gb}} \frac{1}{g(\gamma)\sqrt{f_{0,int}(\gamma)}}. \tag{3.17}$$

Using these equations, the phenomenological phase field parameter values for arbitrary values of boundary energy and mobility can be calculated using the algorithm described below [149]. After assigning the desired boundary width to l_{gb} and random values to the initial guesses for σ_{init} and γ_{init}, $g(\gamma_{init})$ is solved using the fitted polynomial of Fig. 3.3, and $f_{0,int}(\gamma_{init})$ is solved from the fitted polynomial of Fig. 3.4 (b) and Eq. 3.12. The phenomenological parameter m can be thus calculated from Eq. 3.17.

For convenience, a new parameter a is employed and defined as $a = \sqrt{f_{0,int}(\gamma)}/g(\gamma)$. The initial value of a, a_{init}, can be calculated from $\sqrt{f_{0,int}(\gamma_{init})}$ and $g(\gamma_{init})$. For every combination of boundary energy σ and mobility M, the other phenomenological parameters can calculated iteratively using the following procedure:

1. From Eq. 3.15 calculate $\kappa^* = \sigma l_{gb} a_{init}$
2. From Eq. 3.11 calculate $g(\gamma^*) = \sigma/\sqrt{\kappa^* m}$
3. From $g(\gamma^*)$ in Step 2 calculate γ^* using Fig. 3.3
4. Calculate $f_{0,int}(\gamma^*)$ from Fig. 3.4 (b) and Eq. 3.12
5. Calculate the intermediate value of a (denoted as a^*) and compare to a_{init}. If the two values are equal, then $\kappa = \kappa^*, \gamma = \gamma^*, a = a^*$. If not, redo the calculation from step 1 using $a_{init} = a^*$.
6. L is calculated from Eq. 3.16.

The calculated phase field parameters m, L, γ, κ are stored in lookup tables that are read by the phase field simulation when anisotropic boundary energy and mobility are employed.

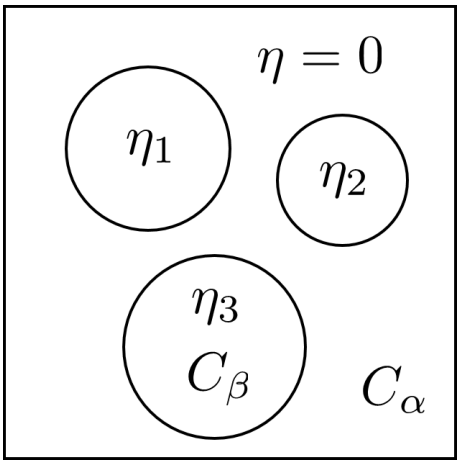

FIGURE 3.5: Schematic of Ostwald ripening in a binary system. The β-phase particles are embedded in the α-phase matrix. In the phase field model for Ostwald ripening, the order parameter η describes different particles, and a new phase field C distinguishes one phase from the other.

3.5 Phase field simulation of Ostwald ripening

In Sec. 2.3, multiphase coarsening, namely Ostwald ripening, was introduced. Phase field simulation is a perfect choice to model such coarsening, as multiple phases are intuitively distinguished by different phase fields. Furthermore, the driving force for Ostwald ripening can easily be incorporated into the model. Pioneering work for modeling Ostwald ripening using the phase field method was carried out by Fan and Chen [164–167]. Recent developments in computational power have made it feasible to extend the model from 2D to 3D [168–171]. In this thesis, phase field simulations of Ostwald ripening were made available by the courtesy of Dr. Nan Wang of Penn State University. His implementation followed the description given in Refs. [167, 172].

Similar to the phase field simulation of grain growth, the particles undergoing Ostwald ripening are distinguished by an order parameter $\eta(\mathbf{r}, t)$. Additionally, a new phase field C is introduced to describe the local concentration, which is also a function of space and time, represented by $C(\mathbf{r}, t)$. A simple case of binary-phase Ostwald ripening is shown in the schematic diagram of Fig. 3.5. The β-phase particles are embedded in the α-phase matrix. Within a given particle i, $\eta_i = 1$ and $\eta_{j\neq i} = 0$. In the matrix phase, all η components take on the value 0. C equals C_α and C_β within the matrix phase and the β-phase particles, respectively. At the interfaces between the two phases, C takes on intermediate values. The concentration field C differs from the order parameter η by the fact that C is a conserved field, owing to the requirement of mass conservation [167].

The total free energy of the system is a function of both η and C,

$$F = \int_V \left[f_0 \left(C, \eta_1, \eta_2, ...\eta_p \right) + \frac{\kappa_C}{2} \left| \nabla C \right|^2 + \sum_{i=1}^{p} \frac{\kappa_i}{2} \left| \nabla \eta_i \right|^2 \right] dV, \tag{3.18}$$

where p is the number of distinct particles, κ_C and κ_i are gradient energy phenomenological parameters, and f_0 is the local free energy density, which is given as

$$f_0 = f_1 \left(C \right) + \sum_{i=1}^{p} f_2 \left(C, \eta_i \right) + \sum_{i=1}^{p} \sum_{j \neq i}^{p} f_3 \left(\eta_i, \eta_j \right). \tag{3.19}$$

The exact forms of f_1, f_2 and f_3 are described in Ref. [167]. They are constructed in such a way that f_0 has its degenerate minima for $\eta_i = 1$ and $\eta_{j \neq i} = 0$ at the equilibrium concentration C_β.

The evolution of the order parameters η_i follows the same TDGL equation (Eq. 3.3) as in the simulation of grain growth. For the conserved concentration field C, its evolution is governed by the Cahn-Hilliard equation,

$$\frac{\partial C}{\partial t} = \nabla \left\{ D \nabla \left[\frac{\delta F}{\delta C} \right] \right\}, \tag{3.20}$$

in which D is a kinetic coefficient related to atomic diffusion [167].

In Sec. 2.3, I highlighted the coarsening kinetics of Ostwald ripening when the volume fraction (V_V) of the coarsening phase is high. In Fan and Chen's model, the interaction between particles is automatically taken into consideration, regardless of how high V_V may be. In the low volume fraction regime, the interaction between particles can be ignored; hence, in this case, the evolution of the sample microstructure is governed primarily by the Cahn-Hilliard equation for the concentration field C.

Chapter 4

4D Characterization of Microstructure

New techniques have been developed in recent decades to characterize the microstructure of materials in 3D. Depending on whether or not the characterized material is destroyed during characterization, these techniques are categorized into two types: destructive or nondestructive methods.

The destructive methods can be traced back to the serial sectioning of samples by mechanical polishing [173, 174], in which the top layer of a specimen is removed by polishing after characterization (*e.g.*, using optical microscopy or scanning electron microscopy), revealing a new surface ready for the next characterization step. In this way, the 3D microstructure can be reconstructed if the spacing between the layers is known. Later efforts led to serial sectioning automated by a FIB-EBSD. In this technique, a conventional SEM is combined with a focused ion beam (FIB), which allows *in situ* serial sectioning without moving the sample between polishing and imaging stations. FIB-EBSD yields a more precise 3D reconstruction of the characterized material, representing a new opportunity for materials scientists to investigate materials in 3D [15–19].

In nondestructive techniques, sample characterization often relies on x-rays. When interacting with a material being characterized, transmitted or scattered x-ray beams can reveal the material's internal microstructure. For example, computed tomography (CT) takes advantage of the intensity difference of transmitted x-rays when the latter pass through different phases, *e.g.,* participates, voids or inclusions. Owing to the difference in x-ray absorption of different phases, the corresponding microstructure can be distinguished. This technique, however, becomes less useful when investigating single-phase materials. X-ray diffraction (XRD) methods are often used to probe such materials.

Information like crystal symmetry, strain and texture can be obtained, and the average grain size can be estimated. However, morphological information is absent from conventional XRD characterization. Considering the merits of both CT and XRD, a combination of both techniques offers a new avenue toward characterizing microstructure in 3D. This includes successful new methods like three-dimensional x-ray diffraction (3DXRD) microscopy [20] and x-ray diffraction contrast tomography (DCT) [21, 175].

Only the nondestructive techniques allow for the investigation of microstructure in 4D (3D plus the temporal dimension), as microstructural evolution cannot be followed in destroyed layers. In this thesis, the time-resolved 3D characterization of microstructure relies on a synchrotron-based 3DXRD technique. In the following sections of the chapter, I present the principles of this technique, the details of the experimental setup and the associated reconstruction procedures.

4.1 3DXRD and other comparable 3D characterization techniques

In 3DXRD measurements, materials are irradiated by hard x-rays from a synchrotron source. The typical x-ray energy is in the range of 20–100 keV. For an incident x-ray beam of wavelength λ, constructive interference of x-rays is possible only when the Bragg condition is fulfilled for the crystallites,

$$2d \sin\theta = n\lambda, \tag{4.1}$$

where d denotes the spacing between lattice planes, θ is the angle between the incident x-ray beam and the scattering lattice planes, and n is an integer giving the order of the reflection.

Two types of modes are proposed for the collection of diffraction spots in 3DXRD [20, 176]. The first mode, grain center mapping, allows fast determination of phases, center-of-mass positions and volumes, as well as the average characteristics of grains, such as orientations and strain tensors. In this mode, however, the locations of grain boundaries are ambiguous. Nevertheless, it is worth noting that with the knowledge of grain center-of-mass locations and the associated volumes, boundary locations can be estimated using post-processing techniques like Laguerre tessellation [177–179]. The second mode for collecting diffraction spots makes it possible to perform a complete volumetric mapping of the microstructure. High-spatial-resolution detectors are essential for this purpose. Under this mode, boundary positions can be determined with good confidence, and individual grain orientations or even orientation spreads inside individual grains can be

probed. Therefore, this mode is ideal for investigating grain boundary properties as well as for characterizing deformed materials, in which the lattice orientation varies within individual grains. The compromise for the precise characterization provided by this mode is its lower time-efficiency compared to the first mode.

Using the two operation modes of 3DXRD, different physics phenomena can be investigated. In Refs. [23, 180], the authors explored the effect of heterogeneities in recrystallization using 3DXRD. The latter technique is also used in the study of solidification [181, 182] and plastic deformation [183, 184]. Moreover, the internal stresses of materials can be calculated from strain tensors measured by 3DXRD. From the first feasibility studies performed on a single grain [185, 186], this technique has shown its capability to characterize strains in multigrain systems simultaneously [187–189]. 3DXRD has also been used to measure grain rotations during deformation processes [190, 191] and during Ostwald ripening [192]. Concerning the focus of this thesis—grain growth—the first successful experimental investigation using 3DXRD was carried out by Schmidt *et al.* [25]. In the latter study, 483 grains were mapped in an Al-0.1% Mn specimen. A second map made after annealing showed that significant grain growth had taken place, as there were only 27 grains left. In this initial investigation, the spatial resolution was not sufficient to accurately determine the local curvature of grain boundaries [25].

It is worth mentioning another technique, x-ray diffraction contrast tomography (DCT), as it shows great similarity to 3DXRD microscopy. DCT was first proposed in Refs. [21, 175]. With only one near-field detector, extinction spots are observed in the transmitted beam when a grain fulfills the Bragg condition. Meanwhile, the outer regions of the same detector are used to record near-field diffraction spots. Reconstruction is based on the near-field diffraction patterns, taking advantage of the use of Friedel pairs [193]. For the detailed working principal and experimental setup, readers are referred to the review by Reischig *et al.* [194]. DCT yields good results for grain growth investigation. As shown in Ref. [26, 27], Syha *et al.* successfully measured the evolution of 849 grains in $SrTiO_3$ before and after one annealing step with a spatial resolution of 0.7 μm.

Instead of using synchrotron radiation, new technology has been developed to perform similar measurements with a laboratory x-ray source. The so-called laboratory x-ray diffraction contrast tomography (LabDCT) technique was demonstrated first in the research paper of King *et al.* [195]. Using a W-target x-ray tube source operated at 90 kV and 350 μA, the authors were able to map the grain shapes and orientations of 42 grains in a titanium sample (with average grain size around 170 μm). Compared to the synchrotron radiation approach, however, the diffraction spots collected in LabDCT may be magnified and distorted simply because of the cone-beam geometry of the laboratory x-ray source. This increases the complexity of data reconstruction. Moreover, owing to

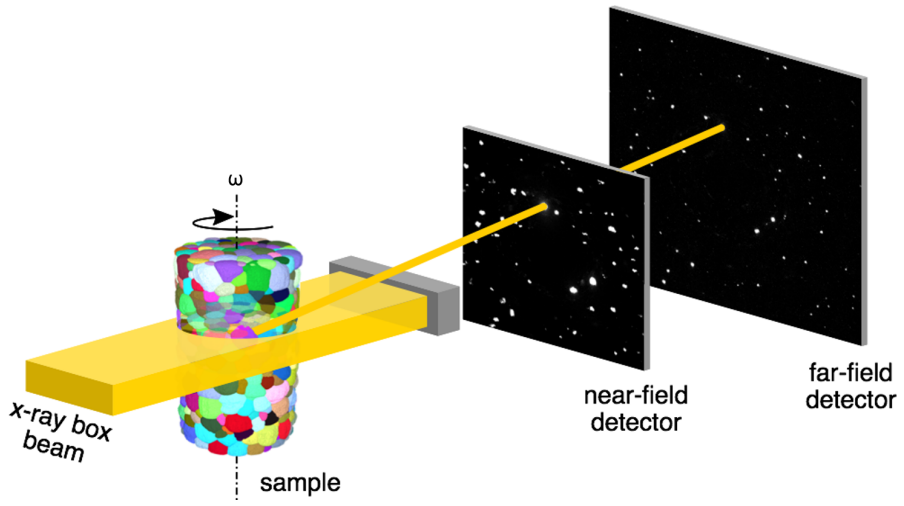

FIGURE 4.1: Schematic of the 3DXRD experimental setup. An x-ray box beam irradiates a cylindrical sample that is mounted on an ω rotation stage. Diffracted beams are collected by the near-field (NF) detector and the far-field (FF) detector. Note that the two detectors were not operated simultaneously in the experiments; rather, the diffraction patterns were collected one after the other. The image was adapted from Ref. [198] with kind permission by Jules Dake.

the lower intensity of the laboratory x-ray beam, the exposure time for each projection is considerably longer than with a synchrotron radiation source. It was reported that the exposure time of one projection was 60 s in Cu [196] and 300 s in a titanium alloy [197]. Although it has some drawbacks, LabDCT has grown in popularity, as it makes 3D (or 4D) microstructural characterization possible in a laboratory setting. This makes 3D characterization much more accessible to materials scientists, considering the fact that 3DXRD microscopy and the DCT technique are available nowadays only at a limited number of synchrotron facilities around the world.

4.2 Data collection

The 3DXRD measurements carried out in this thesis were performed at beamline BL20XU of the synchrotron radiation facility SPring-8 in Japan. The experimental setup is shown schematically in Fig. 4.1, in which the sample being characterized is mounted on a rotation stage. The sample preferably has a cylindrical shape, and its size is limited by the width of the x-ray beam. In our experiments at SPring-8, the sample diameter had to be 1.4 mm or smaller.

The ω rotation stage is rotated around an axis oriented perpendicularly to the incoming beam. The specimen is rotated up to 360° with a step size of $\Delta\omega$ in order to map out the complete microstructure. During rotation, grains that fulfill the Bragg condition generate diffraction beams, which are collected by the detectors. The detectors consist

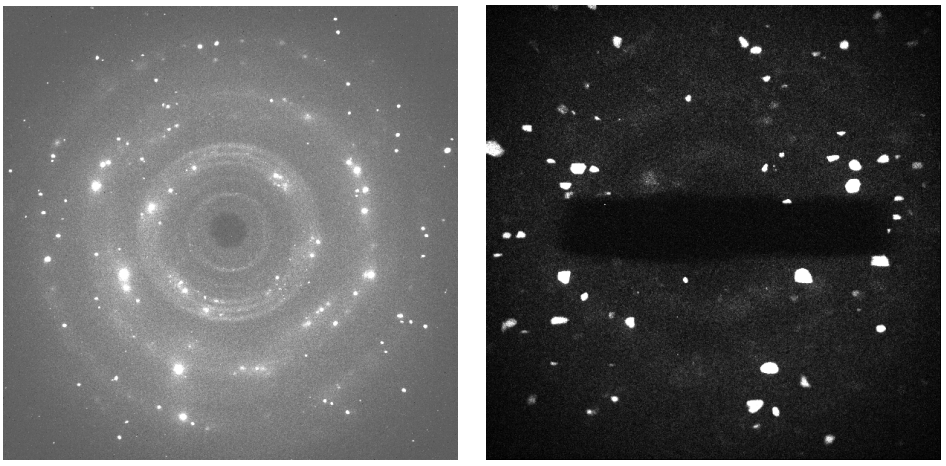

(a) (b)

FIGURE 4.2: Diffraction spots collected by (a) the far-field detector and (b) the near-field detector.

of a scintillator screen that converts x-rays to visible photons and a CCD camera that detects those photons. To enable both measurement modes as mentioned in Sec. 4.1, two separate detectors are necessary. A near-field (NF) detector with a spatial resolution around 1–5 μm is placed close to the sample (usually 2–20 mm) for volumetric mapping; a far-field (FF) detector with a lower spatial resolution (around 50–200 μm) is located 10–50 cm away from the sample, enabling fast crystallographic mapping [20]. Figure 4.2 shows an example of the diffraction spots collected by both detectors. The FF diffraction pattern (Fig. 4.2 (a)) is similar to the Debye-Scherrer rings that are collected in powder diffraction experiments. In contrast, the NF diffraction spots are located at more random positions. The shapes of the latter spots reveal the grain morphology.

Prior to carrying out 3DXRD measurements, a number of important parameters, such as the x-ray energy, the exposure time at each $\Delta\omega$ and the detector distances, must be estimated. The x-ray energy is chosen according to the x-ray attenuation property of the sample material. For aluminum alloys, a beam of 32 keV was used in the measurements of this thesis. The $1/e$ attenuation distance is calculated to be around 3.3 mm, according to the Beer-Lambert Law [199], which is larger than the maximum allowed sample diameter of 1.4 mm. Accordingly, the exposure time at each $\Delta\omega$ had to be tuned so that the intensity of the diffraction spots is in the detectable range of the detector channels. In addition, a determination of the distances between the sample and the NF detector/FF detector must be carried out. Depending on the areal density of diffraction spots for a given crystal lattice, 3–5 diffraction rings are ideal for data reconstruction [200]. The optimal detector distances can then be estimated from Eq. 4.1 after inserting the detector dimensions, the x-ray energy and lattice parameter of the sample material.

When there is too much overlap of the diffraction spots in the diffraction patterns, determination of crystallographic information is rather challenging. To avoid illuminating too many grains at once, the scanning of samples can follow the box-scanning method described in Refs. [20, 176]. In this thesis work, sample scans were divided into ten layers, with each having a height of 300 μm. An overlap of 50 μm was set between the layers in order to overcome reconstruction difficulties close to the beam edge.

In order to investigate the coarsening of materials, *ex situ* annealing must be carried out. After each annealing step, the microstructure is remapped by 3DXRD microscopy. As the heat treatment takes place outside the beam hutch, care must be taken to replace experimental specimens in the same position in the sample holder for the convenience of data reconstruction. From practical experience, a (physical) marker on the specimen that can survive the annealing procedure is helpful for this purpose.

4.3 Data reconstruction and post-processing

After the collection of diffraction data, the crystallographic and volumetric reconstruction of microstructure is carried out using the software packages FABLE (Fully Automatic BeamLine Experiments) [201] and GrainSweeper [202]. The mathematical aspects of the individual programs in FABLE are discussed in separate references (ImageD11 [203] and GrainSpotter [204]). Once reconstructed, the data must go through necessary post-processing procedures to ensure its full utilization in a 4D manner. In Fig. 4.3, I summarize the complete procedures for reconstruction and post-processing in a flow chart. In the remainder of this section, I present the details of each step shown in Fig. 4.3.

4.3.1 Far-field data reconstruction

An example of a raw FF diffraction image has already been shown in Fig. 4.2 (a). In this image, the positions of the diffraction spots contain the crystallographic orientation of the grains. Additionally, the intensities of the spots are related to the grain volumes. Segmentation of hundreds of diffraction spots is the first step of the FF data reconstruction. Thresholds in both spot size and spot intensity are implemented in order to separate the signals from noise. Note that in the current reconstruction routine, the FF spot intensity is not used for the estimation of grain volume, as a more precise volumetric reconstruction is carried out by near-field data reconstruction. In the end, the segmented spots in Fig. 4.2 (a) are shown by the marked red circles in Fig. 4.4 (a). Figure 4.4 (b) shows the overlain results of all FF images that were collected at each ω

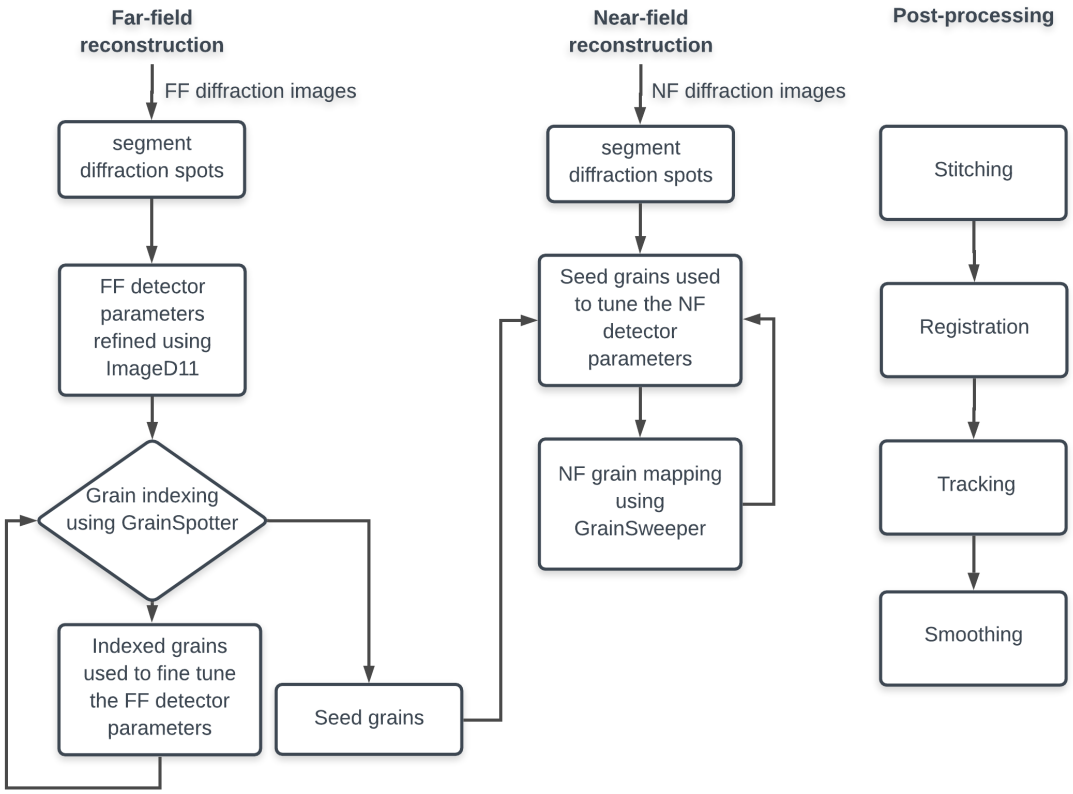

FIGURE 4.3: A summary of the reconstruction and post-processing procedures for raw 3DXRD datasets.

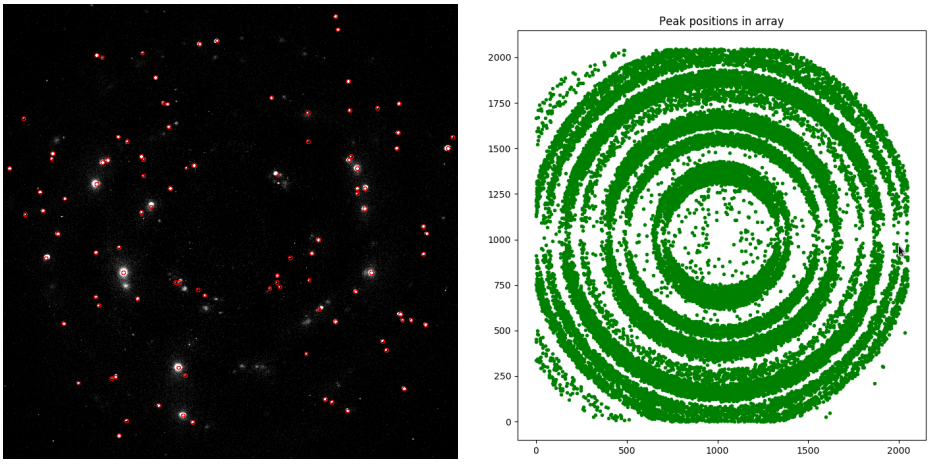

(a) (b)

FIGURE 4.4: (a) Segmentation of the FF pattern of Fig. 4.2 (a). The diffraction spots identified using both size and intensity thresholds are marked with red circles. (b) Overlay of FF patterns collected at all ω angles.

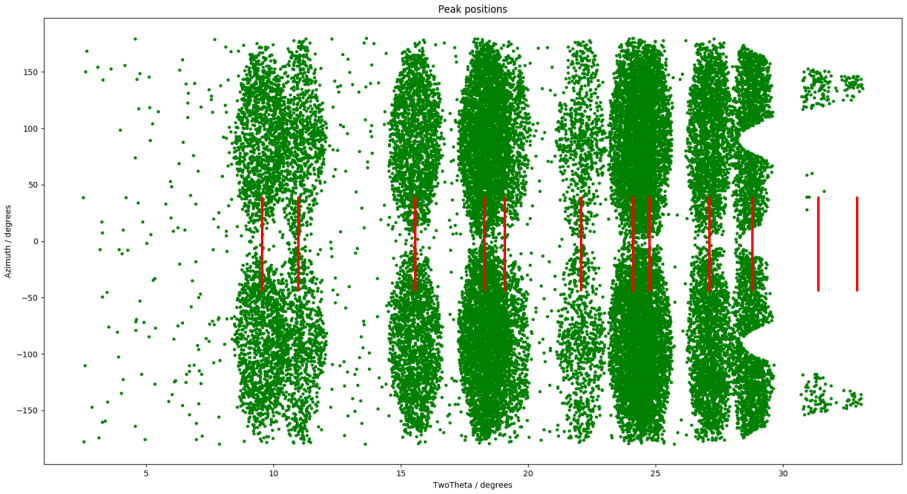

FIGURE 4.5: The Debey-Scherrer rings in Fig. 4.4 (b) are "unrolled" (*i.e.*, plotted as azimuth angle versus 2θ). The detector parameters are tuned iteratively in ImageD11 until the diffraction spots are arranged symmetrically about the theoretical peak positions marked by the red lines.

angle; this image contains all of the diffraction spots collected from the specimen. The resulting pattern shows great similarity to the Debey-Scherrer rings obtained by x-ray powder diffraction.

Before indexing the segmented spots to crystallographic orientations, it is essential to tune the detector parameters with great precision in ImageD11, including the detector distance, the x-ray beam center, the detector tilts, etc. [203]. In ImageD11, the Debey-Scherrer rings in Fig. 4.4 (b) are unrolled. After inserting the correct crystal lattice constant, crystal symmetry, x-ray wavelength and other associated parameters, the software fits detector parameters iteratively until the diffraction spots are centered about the theoretical peak positions marked by the red lines in Fig. 4.5.

GrainSpotter [204] indexes the diffraction spots to individual grains. Each spot is transformed into a scattering vector in reciprocal space: namely, a G vector [204]. Random trials are performed in orientation space to match the theoretical G vectors with the experimental ones. According to the desired completeness (*e.g.,* the minimum number of reflections per grain), a list of detected grains is generated. These grains are then used to retune the far-field detector parameters in a subsequent step in ImageD11. With improved detector parameters, GrainSpotter can identify more grains. These procedures are repeated iteratively until no more grains are identified. FF reconstruction yields a list of grains with indexed center-of-mass positions and crystallographic orientations, as shown in Fig. 4.6.

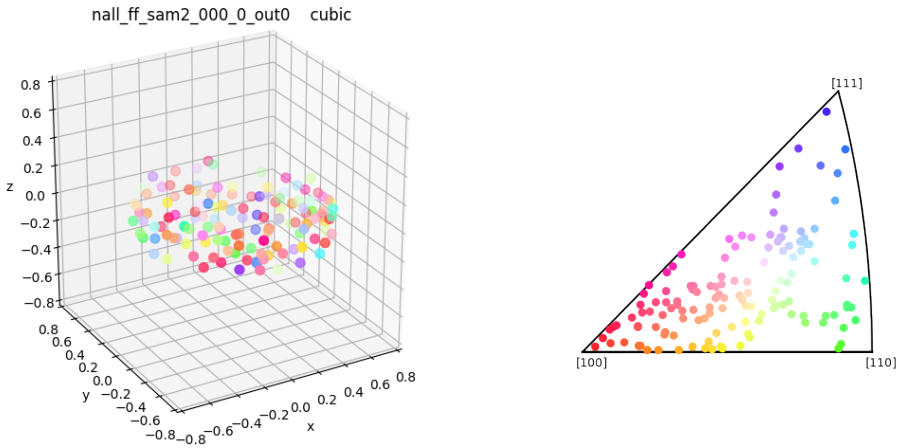

(a) (b)

FIGURE 4.6: (a) The center-of-mass plot of grains indexed by FF reconstruction and (b) the associated crystallographic orientations.

4.3.2 Near-field data reconstruction

Near-field data reconstruction starts from diffraction spots segmented on the raw diffraction images, similarly to the FF data reconstruction. Afterward, the NF detector parameters are optimized by the software package ImageD11. The complete volumetric mapping of samples works on a voxel-by-voxel basis using GrainSweeper [204]. The seed grains, which were generated by the FF reconstruction, are dilated until they form boundaries. In this manner, a possible orientation is assigned provisionally to each voxel in the reconstructed volume from the associated seed grain orientation. In GrainSweeper, the reconstruction algorithm simulates the diffraction of x-rays from each individual voxel, projecting diffraction spots onto the simulated detectors with the optimized detector parameters [204]. If more than 70% percent of the simulated diffraction spots match those found in the experimental diffraction patterns, the voxel is assigned to the provisionally chosen orientation. The completeness of a given voxel is defined to be the ratio between the number of experimentally-detected diffraction spots associated with this voxel and the number of simulated diffraction spots. A typical completeness map is shown in Fig. 4.7 (a) for an xy cross-section of the reconstructed volume, with the white color indicating higher completeness. The corresponding volumetric mapping along the same cross-section is shown in Fig. 4.7 (b). In Fig. 4.7 (b), the color denotes the local grain orientation using Rodrigues vectors. A successful NF reconstruction requires not only high completeness at grain interiors but also reasonable values at grain boundaries, which constitute the information concerning grain crystallography and grain morphology that are input into investigations of microstructure at the grain and grain boundary levels.

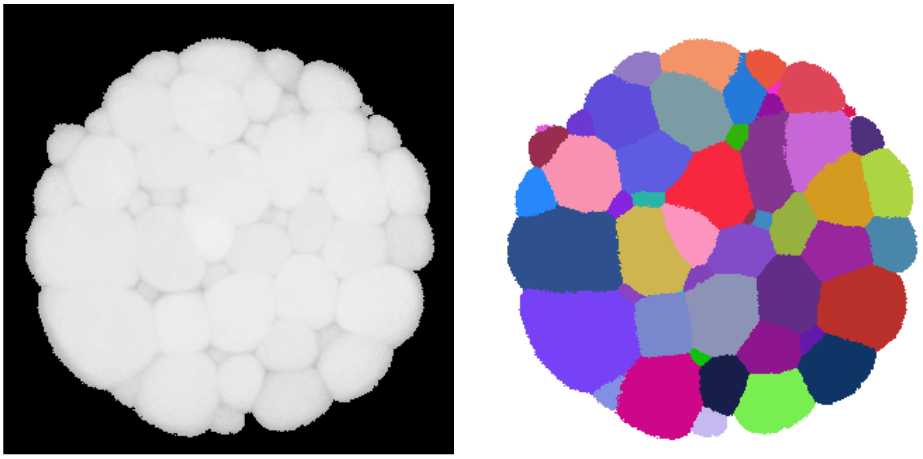

(a) (b)

FIGURE 4.7: (a) Completeness map of a NF reconstruction shown in an xy cross section. White indicates a high completeness value. (b) Grain mapping for the cross section of (a). Colors denote the grain orientation.

4.3.3 Post-processing

4.3.3.1 Stitching

As discussed in Sec. 4.2, a box-scanning method was employed for diffraction signal collection to avoid the presence of too many diffraction spots on the detectors. A scan is divided into multiple layers, and a certain vertical overlap is set between the layers. This overlap makes it possible to stitch multiple layers together using the algorithm described in Ref. [198]. In brief, grains in the overlap region of two successive layers that have misorientation angles below 1° are considered to be the same grain. These grains are assigned the same label after stitching.

4.3.3.2 Registration

Data registration is essential for the accurate investigation of coarsening, as the specimen must be alternately mounted for 3DXRD measurement and then removed for *ex situ* annealing. Although careful realignment is carried out following the practical suggestions mentioned in Sec. 4.2, minor misalignment between volumetric mappings performed at different annealing times is unavoidable. The misalignment mostly lies in a rotation about the z-axis and translations in the x- and y-direction. Suggestions from Ref. [198] were adopted for the data registration carried out in this thesis. Considering the fact that grain orientations measured at different timesteps are defined in the same reference frame, a change in orientation of the same grain between two timesteps must reflect a change in the sample coordinate system (assuming that grains do not rotate during

coarsening). Therefore, the global rotation of the sample coordinate system can be estimated from the average orientation change of grains identified to be the same in each mapping. After sample rotation has been addressed, the remaining misalignment arises mainly from translation in the x- and y-direction. These translations are addressed using the Image Processing Toolbox in MATLAB by matching the network of grain boundaries at different timesteps.

4.3.3.3 Tracking

For easy analysis of time-dependent features of grains, it is suggested to give all grains the same grain label if the grains are identified to be the same at different timesteps. Termed as tracking, this process uses the backward routine described in Ref. [198]. Because new grains do not appear during coarsening, every grain that is present at a later time step $t_i\,(i \geq 1)$ must have a counterpart at time step t_{i-1}. Therefore, tracking considers the match in both real space and orientation space: for a grain labeled as X at $t_i\,(i \geq 1)$, any grain at t_{i-1} that overlaps more than half of the volume of grain X at t_i is considered to be a candidate for the tracked grain X at t_{i-1}. Furthermore, the distances between the candidate grains and the grain X in orientation space are considered. A properly tracked grain should manifest a short distance in orientation space. Typically, a misorientation angle below 1° is a good threshold for efficient tracking. Nevertheless, grains sometimes yield multiple matchings or no matching whatsoever, necessitating manual examination and relabeling.

4.3.3.4 Smoothing

As discussed in Sec. 4.3.2, the quality of a NF reconstruction is quantified by the completeness, which typically drops in the vicinity of grain boundaries (*e.g.,* Fig. 4.7 (a)). Owing to the low completeness, the reconstructed boundary morphology may be somewhat irregular or poorly defined. Figure 4.8 (a) shows a reconstructed slice where this issue is severe. Some boundaries manifest a zigzag shape, like those indicated by the white arrows. Such boundaries rarely result from a physical coarsening process, as grain boundaries tend to migrate so as to eliminate locations of high curvature, which certainly includes the zigzag corners. This reconstruction artifact should be eliminated before attempting to relate the measured boundary migration to the microstructure. To correct such problems, I impose a 3D phase field grain growth model on the reconstructed microstructure for a very short time, which allows the irregular boundaries to relax according to the physics governing coarsening (Sec. 3.2). Figure 4.8 (b) shows the result of the correction routine applied to the cross section of (a). After 25 iterations of

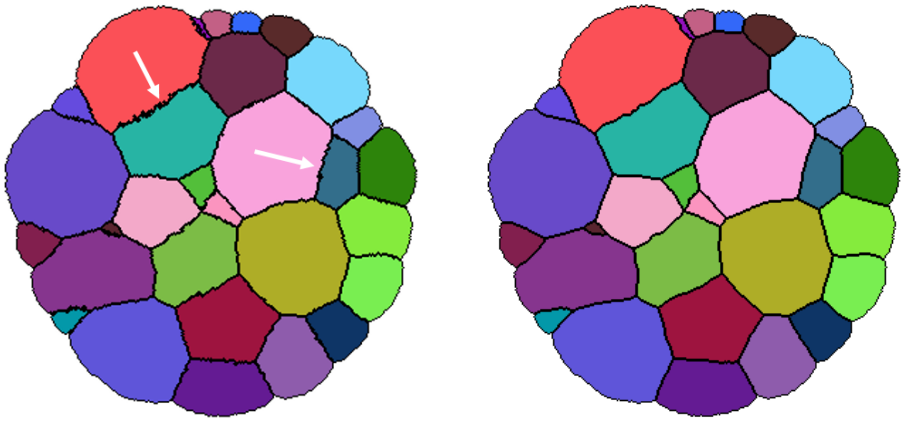

(a) (b)

FIGURE 4.8: (a) Grain boundaries may manifest roughness (white arrows) arising from the lower value of reconstruction completeness near boundaries. (b) A phase field simulation is utilized to smooth the boundaries: after 25 iterations, most of the roughness has vanished, while the boundaries remain in the same position as in the raw NF reconstruction.

the simulation, most of the boundary roughness has been damped. At the same time, the boundaries remain more or less at their initial positions. After this smoothing step, the resulting datasets are considered to be the final output of microstructural mapping by 3DXRD microscopy.

Chapter 5

Reverse Engineering Method

In Sec. 2.1.3 and 2.1.4, I discussed two important properties of grain boundaries—boundary energy γ and boundary mobility M—and their experimental measurement. The product of both parameters, the reduced mobility M', can be quantified experimentally by the bicrystal technique. However, literature shows that this technique requires a considerable amount of effort, and migration of the bicrystal boundary is quite sensitive to the bicrystal quality [14]. Furthermore, it is practically impossible to cover the entire parameter space for grain boundaries using results of bicrystal experiments. Therefore, in this chapter I present a method to measure M' directly from time-resolved 3D datasets of microstructural evolution. We call this approach the reverse engineering method. Similar to its usage in electronics engineering, reverse engineering is a way to extract and reveal the internal features of a system. In the case of grain growth, I aim to extract the reduced mobility of thousands of grain boundaries in a polycrystalline material and then determine the dependency of M' on macroscopic boundary properties like misorientation and inclination.

As shown in Eq. 2.16, the boundary migration velocity v is a function of M' and the curvature H. Rearrangement of this equation gives

$$M' = \frac{v}{H}. \tag{5.1}$$

In principle, both quantities on the right-hand side of Eq. 5.1 can be extracted from a 4D dataset, allowing us to calculate M' directly. Furthermore, the boundary misorientation Δg and the inclination $\mathbf{n}$ are available from the crystallographic and morphological information contained in 3DXRD datasets. This means that, in the end, the dependency $M'(\Delta g, \mathbf{n})$ can be acquired and investigated experimentally.

It should be noted, however, that the extraction of v and $\langle H \rangle$ from a 4D dataset is not trivial. In this chapter, details of the necessary procedure are discussed. Also, the validity of the reverse engineering method and its many approximations are examined. At the end of the chapter, I give suggestions for the experimental design of time-resolved 3D measurements, which can help yield suitable datasets for the reverse engineering method.

5.1 Measurement of boundary migration velocity

In a 4D dataset, the 3D microstructure at timestep t_i may contain hundreds to thousands of grain boundaries, depending on the sample size and average grain size. From the discrete measurement of boundary position at timesteps t_i and t_{i+1}, the boundary velocity can be estimated. However, between t_i and t_{i+1} the boundaries change not only their positions but also their sizes and shapes. Thus, extraction of local velocity at each location of a boundary is a rather complicated issue, as it is unclear how to find a one-to-one mapping that takes the boundary locations at t_i to boundary locations at t_{i+1}. Here, only the average boundary migration velocity $\langle v \rangle$ is considered. Specifically, $\langle v \rangle$ is estimated from the boundary's average displacement ΔR over the annealing time Δt,

$$\langle v \rangle = \frac{\Delta R}{\Delta t}. \tag{5.2}$$

Two grains from a 4D dataset are shown in Fig. 5.1 to illustrate the estimation of $\langle v \rangle$. In Fig. 5.1 (a), the boundary between the two grains at t_i is highlighted in red. The corresponding boundary area is denoted as A_i. At timestep t_{i+1} (Fig. 5.1 (b)), both grains have changed their morphologies upon annealing, resulting in migration of the boundary. As indicated in red, it moves upwards, and the associated area changes to A_{i+1}. This is more clearly depicted in Fig. 5.1 (c), in which the boundaries at both timesteps are shown together. The boundary sweeps through part of the volume of the original upper grain. The swept volume V_{swept} is defined to be the volume that is exchanged from one grain to the other during the time interval $(t_i, t_{i+1}]$. With the boundary areas at both timesteps, A_i and A_{i+1}, the average migration distance ΔR of the boundary can be estimated as

$$\Delta R = \frac{V_{\text{swept}}}{(A_i + A_{i+1})/2}. \tag{5.3}$$

Combining Eq. 5.2 and Eq. 5.3, we obtain

$$\langle v \rangle = \frac{2V_{\text{swept}}}{(A_i + A_{i+1})\Delta t}. \tag{5.4}$$

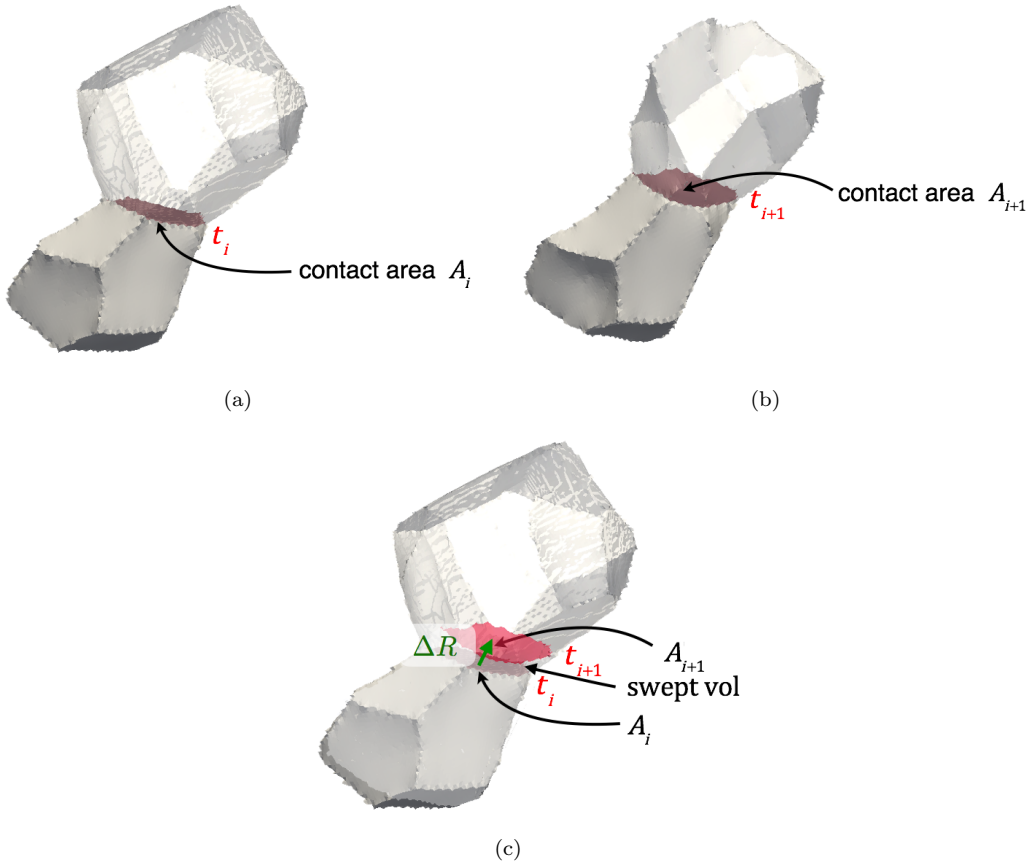

FIGURE 5.1: (a) The boundary between two grains at timestep t_i has an area of A_i. (b) Upon annealing, the boundary moves upwards. The resulting boundary area is A_{i+1} at t_{i+1}. (c) The boundary positions at t_i and t_{i+1} are shown. The volume exchanged between the two boundaries is termed the swept volume V_{swept}. From the indicated boundary positions, the average boundary migration distance ΔR can be estimated.

Note that in Eq. 5.4, the sign of $\langle v \rangle$ follows the sign of V_{swept}. When a boundary moves outwards with respect to the chosen "reference grain," the sign of V_{swept} is positive because the reference grain gains volume; an inward-moving boundary yields a negative V_{swept}. In the example of Fig. 5.1, if the bottom grain is considered to be the reference grain, V_{swept} is positive, but when the top grain is chosen as the reference, the sign of V_{swept} is negative. Nevertheless, when taking into account the sign of the boundary curvature (described in the following section), both cases yield the same value for M'. In addition, V_{swept} is defined to be the net swept volume: that is to say, if part of a boundary has a positive V_{swept} and other parts migrate in the opposite direction (*i.e.*, having negative V_{swept}), the final V_{swept} of the boundary is the sum of the positive and negative contributions.

Between two discrete timesteps grains may vanish. In other words, a grain surrounded by its first-nearest neighbors at t_i may come into contact with second-nearest neighbors

at t_{i+1}. In this situation, the exact time when a first-nearest neighbor vanishes is ambiguous. Thus, Δt in Eq. 5.4 would be undefined. Such cases are neglected in the analysis by adding a restriction to the allowable change in boundary area between time steps:

$$\left| \frac{A_{i+1} - A_i}{A_i} \right| < 100\%. \tag{5.5}$$

Under this restriction, the area of a boundary considered at t_{i+1} is not permitted to be 0. Such a threshold also filters out the situation in which a boundary area increases dramatically over the course of the annealing interval such that $A_{i+1} > 2A_i$. On the other hand, when a boundary undergoes only a minor migration, the determination of ΔR may be inaccurate, since then the relative error of the measurement of V_{swept} is larger (at fixed spatial resolution). The lower threshold for V_{swept} is set to 300 voxels. Further remarks concerning this threshold are given in the next section. To conclude, the application of area and volume thresholds results in only the grain boundaries of moderate migration being selected for reverse engineering analysis.

5.2 Measurement of boundary curvature

In this section, a method for determining the boundary integral mean curvature $\langle H \rangle$ is presented. One of the main challenges of computing boundary curvature is that the 3D reconstructed microstructure is usually extracted in the form of a voxel-based representation. Owing to this fact, two difficulties arise: on the one hand, the grain boundaries are specified implicitly—as interfaces between grain volumes; on the other hand, these interfaces exhibit roughness as a result of the underlying grid, which leads to large errors in the curvature estimation.

The software DREAM.3D (D3D) [205] is an excellent tool for overcoming these problems. The built-in function "Quick Surface Mesh" is employed to mesh interfaces between grain volumes. After a surface mesh is generated, the boundaries are represented by a collection of discrete triangles. Nevertheless, the mesh retains vestiges of the stair-step morphology from the underlying grid. Laplacian smoothing is applied to the mesh to recover the intrinsic shape of each boundary [206]. The smoothing power is controlled by the product of the number of smoothing iterations N and the smoothing factor λ, which governs how far a vertex is permitted to move from its original location during one smoothing iteration. For each triangle of the smoothed mesh, the mean curvature H can be calculated in D3D following the algorithm given in Ref. [207].

However, an accurate curvature estimation is highly dependent on the applied smoothing procedure [28, 29, 208]. In Ref. [28], the authors concluded from their investigation of

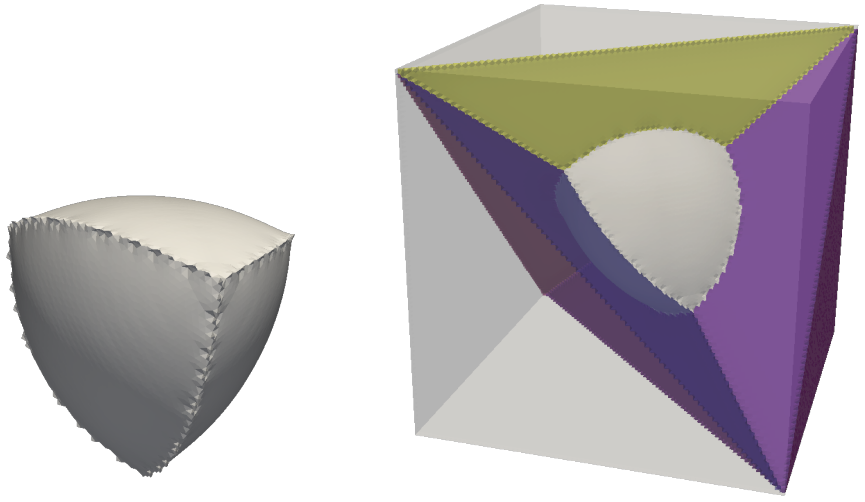

(a) (b)

FIGURE 5.2: (a) A Reuleaux tetrahedron has four spherical surfaces. The curvature of each surface is equal to $-1/R$, where R is the distance between vertices. (b) The Reuleaux tetrahedron is embedded in a cubic box, with the surrounding space divided into four regions of equal volume by planar boundaries. At the triple lines formed by the intersection of these planes with the surface of the tetrahedron, the dihedral angles are 120°. First published in: [209].

simulated spherical grains that smaller grains were better smoothed with smaller smoothing parameters, while larger grains required greater smoothing parameters. Nonetheless, for a real microstructure the optimal smoothing parameters for a given grain boundary were found not to be correlated directly with the grain size. In light of these contradictory findings, the authors of Ref. [28] used a single set of smoothing parameters for all grains in their 3D reconstruction.

In this work, the smoothing parameters were optimized on a boundary-by-boundary basis to improve the accuracy of curvature estimation. Instead of the spherical grain used in Ref. [28], a test grain having the shape of a Reuleaux tetrahedron was used to validate the curvature analysis routine. The Reuleaux tetrahedron is defined as the intersecting interior region of four spheres of radius R, which are centered at the vertices of a regular tetrahedron of side length R (Fig. 5.2 (a)). Hence, the curvature of each surface is $-1/R$. Furthermore, the surrounding space is divided into four equal regions, as shown in Fig. 5.2 (b). In this configuration, all dihedral angles between boundaries meeting at triple lines are 120°, which resembles the dihedral angles observed in real microstructures.

This structure was mapped to a cubic grid (with voxel side length set equal to 1) and imported into D3D. After meshing, Laplacian smoothing was applied to the mesh; the parameter λ was set to 0.2 at vertices of the surface triangles and reduced to 0.1 for

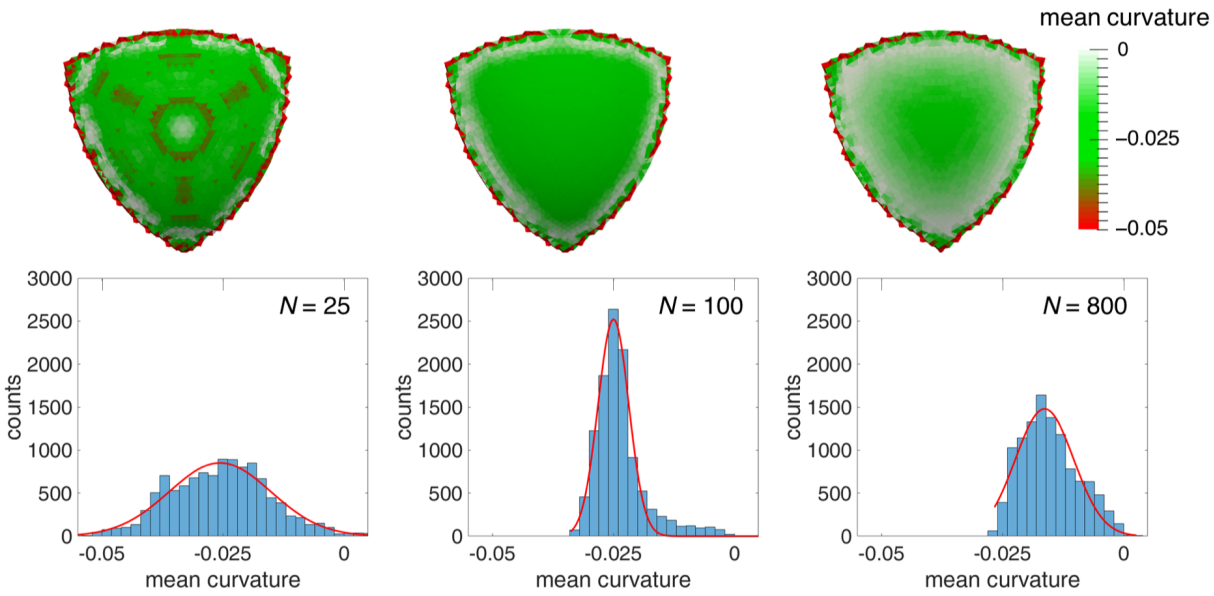

FIGURE 5.3: Influence of smoothing power on curvature estimation for a Reuleaux tetrahedron with $R = 40$. The smoothing parameter N takes on values of 25, 100 and 800 from left to right. Images in the top row show curvature values for one of the curved surfaces. The corresponding curvature distributions are plotted in the bottom row (after the exclusion of surface triangles adjacent to triple junctions); the red curves are least-squares fits of Gaussian functions to the histograms. First published in: [209].

vertices of a triple junction or quadruple point, in order to prevent the structure from shrinking during smoothing.

While keeping λ at the above-specified values, we tested the influence of smoothing power on the structure by varying the number N of smoothing iterations ($N = 25, 50, 100, 200, 400, 800$). Figure 5.3 shows the calculated curvatures for different values of N applied to one curved surface of the tetrahedral structure with $R = 40$. In the top row of the figure, the patch is colored green when the numerically extracted curvature is close to the true value ($-1/R = -0.025$), while white and red patches denote under- or over-estimations of the absolute value of the curvature, respectively. The curvature estimation is highly inaccurate close to triple lines, as evidenced by the predominance of red patches at the edges of the surfaces. This inaccuracy is to be expected, given the fact that abrupt changes in surface orientation occur at triple lines. For this reason, such values are eliminated from the calculation of boundary curvature. It is also obvious that different N values yield different smoothing results: when $N = 25$, the smoothing is inadequate, as patches with strongly negative curvature (indicated by the red color) are still present in the boundary interior. Raising N to 100 improves the uniformity of the extracted curvature values, but progressing to still higher values of N results in an oversmoothing that causes an increasing fraction of boundary segments to take on curvatures close to zero.

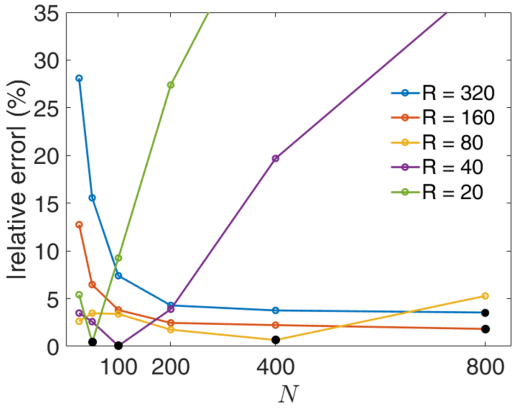

FIGURE 5.4: Absolute value of the relative error (RE) in curvature plotted against N for different sizes R of the tetrahedral test structure. For each R, the position where the minimum RE is obtained is marked by a filled black circle. First published in: [209].

These observations are quantified by the histograms of mean curvature of individual patches in the bottom row of Fig. 5.3. Gaussian functions are fit to the histograms. Using the Gaussian mean value, the average boundary curvature $\langle H \rangle$ is found to be -0.0256, -0.0250 and -0.0163 for $N = 25$, 100 and 800, respectively; the corresponding relative errors are 2.4%, 0% and -34.8%. Thus, for the smoothing of a Reuleaux tetrahedron with $R = 40$, the optimal smoothing parameter N_{opt} is 100.

As shown in Ref. [28], N_{opt} is expected to be related to the resolution of the surface—*e.g.,* the ratio between the size R and the voxel size. This notion was tested on tetrahedral structures with various R values (20, 40, 80, 160 and 320), varying N in each case from 25 to 800. Figure 5.4 plots the absolute value of the relative error (RE) in curvature against N for each R. Similar to the example shown in Fig. 5.3, the RE is found to be large when N is either too small or too large. The optimal choice for N in each case is marked by a black dot in Fig. 5.4. N_{opt} tends toward larger values with increasing R, which is consistent with the findings of Ref. [28] derived from simulated spherical grains.

Nevertheless, Ref. [28] also demonstrated that the smoothing effect on a specific boundary is not directly correlated with the grain size in a real microstructure, as the particular boundaries of a given grain could be highly curved or nearly flat. Owing to this, N_{opt} is chosen using a different strategy based on individual grain boundaries rather than grain sizes. Re-examining the results shown in Fig. 5.3, we find that N_{opt} generates not only the smallest RE but also the narrowest distribution of curvature values. The spread of a histogram can be quantified by the coefficient of variation (CV), which is defined as the ratio of the standard deviation of the distribution to the absolute value of the distribution mean, as extracted from a Gaussian fit. In Fig. 5.5, CV is plotted against RE for different sizes of the test structure. The black dots mark the position

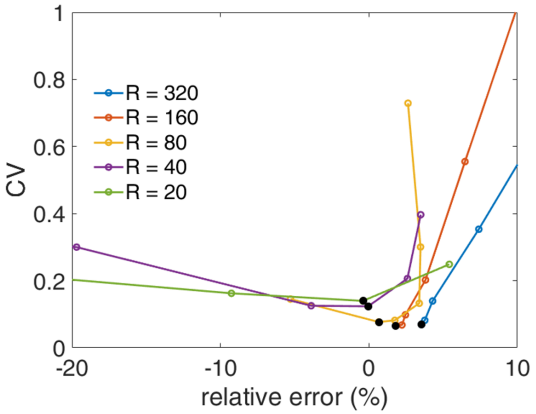

FIGURE 5.5: Coefficient of variation (CV) plotted against the relative error for various sizes R of the tetrahedral test structure. Points of minimum CV are marked by the black circles. First published in: [209].

at which the minimum CV is obtained. These points coincide with the points of lowest RE in Fig. 5.4. Therefore, it is concluded that the minimum-CV criterion identifies smoothing conditions that lead to curvature estimation with a relative error below 5%.

To implement the proposed method, we apply different smoothing parameters N to each grain boundary after they are meshed. The various CV values calculated for a given boundary are compared, and the boundary curvature is set to the value given by the calculation having the smallest CV. Notably, some types of boundaries are eliminated from consideration by the reverse engineering method, as the associated curvature estimations tend to yield low accuracy. Firstly, as shown in Fig. 5.3, owing to the presence of extreme values close to triple lines, up to second-nearest neighbors of triangles located along triple lines are excluded. Following this step, the boundaries must still be large enough for reliable curvature analysis. Boundaries with areas larger than 100 (voxel side length)^2 are considered in the current analysis. Secondly, the threshold applied to the swept volume ($V_{\text{swept}} > 300$ voxel) allows for the analysis of boundary migration distances beyond three voxel side lengths. Finally, extremely flat boundaries should also be eliminated from consideration, as small errors in the curvature estimation of such boundaries lead to massive errors in the resulting M'. A direct threshold is therefore applied to the absolute value of the curvature, restricting the reverse engineering analysis to boundaries with $|\langle H \rangle| > 0.002$ (voxel side length)$^{-1}$.

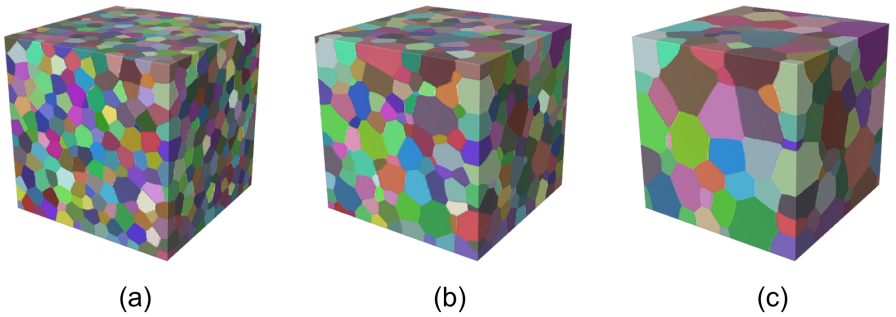

FIGURE 5.6: (a) Initial synthetic microstructure generated by DREAM3D. Phase field simulation of grain growth at (b) $t = 175$ and (c) $t = 535$.

5.3 Method validation

In both the measurement of boundary migration velocity and the determination of boundary curvature, many approximations are involved. Whether or not the resulting M' represents the boundary's true reduced mobility must be validated, and this validation step has to be carried out on a system for which M' is known. Computer simulations of grain growth are ideal candidates for this purpose, as they treat the boundary energy and mobility as explicit input parameters.

To generate the initial microstructure for a grain growth simulation, I utilized the "StatsGenerater" filter in D3D, in which the desired grain size distribution was set to the lognormal type. Such a microstructure was mapped to a 300^3 grid (voxel side length $= 1$), and no periodic boundary conditions were applied. Figure 5.6 (a) shows a synthetic microstructure containing 2001 grains, with the average grain size estimated to be 14.55.

Coarsening of the synthetic microstructure was simulated using a phase field method, as described in Sec. 3.2. I set the boundary M' to 0.25 for all boundaries by choosing $M = 1$ and $\gamma = 0.25$. The corresponding phase field parameters were calculated according to the procedure described in Sec. 3.4. The discretization parameters for the TDGL equation were set to $\Delta x = 0.3$ and $\Delta t_s = 0.01$. The simulation was run long enough to ensure that significant grain growth took place in the system. The simulated microstructure at $t = 175$ and $t = 535$ is shown in Figs. 5.6 (b) and (c), respectively. In Fig. 5.7 the change in grain number and the squared average grain size are plotted against simulation time. Similar to the observations of other phase field simulations (*e.g.,* Ref. [210]), we observe a transient state at the beginning of the simulation, during which the grain number remains nearly stable, and the squared mean radius does not follow a linear relationship with time. This simulation artifact was excluded, and the reverse engineering analysis was applied only to grain growth starting from $t = 175$. At that timestep, the grain number was equal to 973, and the corresponding average grain

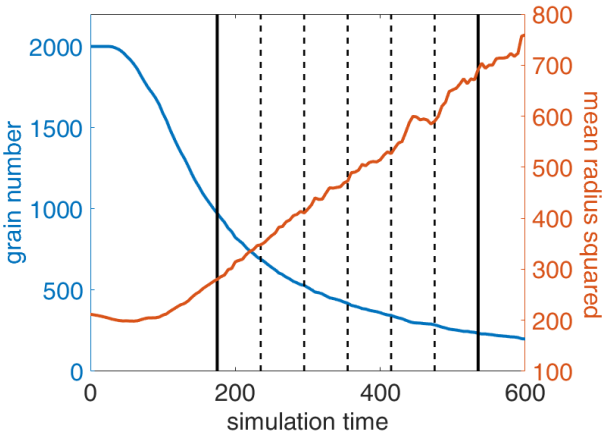

FIGURE 5.7: Number of grains and mean radius squared plotted against time for the grain growth simulation of Fig. 5.6. Reverse engineering of the boundary M' was carried out with the microstructures marked by the solid and dashed black lines from $t = 175$ to 535. The time interval (space between dashed vertical lines) was 60.

radius was 16.74. Although a simulation can generate coarsened microstructures with excellent time resolution, a time interval of $\Delta t = 60$ was selected between two sequential snapshots of the microstructure to better match the annealing duration used in experiments. In total, six time intervals were taken for the analysis, with the last snapshot captured at $t = 535$, in which 234 grains were left, and the mean grain radius equaled 26.29.

Between all sequential timesteps, I applied the methods described in Sec. 5.1 and 5.2 to estimate the migration velocity and curvature of individual grain boundaries. Afterwards, each boundary can be associated with a M' calculated from Eq. 5.1, except for the boundaries that violate the thresholds imposed on the boundary migration velocity or the curvature. Since M' remains constant throughout the entire simulation, the M' values extracted from different time intervals should be indistinguishable. A histogram of M' for all boundaries is shown in Fig. 5.8. The histogram manifests a strong peak close to its median of 0.2535 (marked by the solid red line), which is very near to the simulation input of $M' = 0.25$. The relative error of the median value is only 2.5%.

Nevertheless, the histogram shows a certain spread, which can be quantified by the boundaries of the second and third quartiles of the data. Marked by the dashed red lines in Fig. 5.8, the 25th percentile is located at 0.2129 and the 75th percentile at 0.2947. It is also noteworthy that the histogram exhibits high counts when M' is close to 0. This can be explained by the fact that under the current spatial resolution (voxel side length = 1)[1] and temporal resolution (time interval = 60), boundaries that migrate very short

[1]When extracting M' from voxelized data, we set voxel side length = 1 in order to remove an explicit dependence on length scale from analysis.

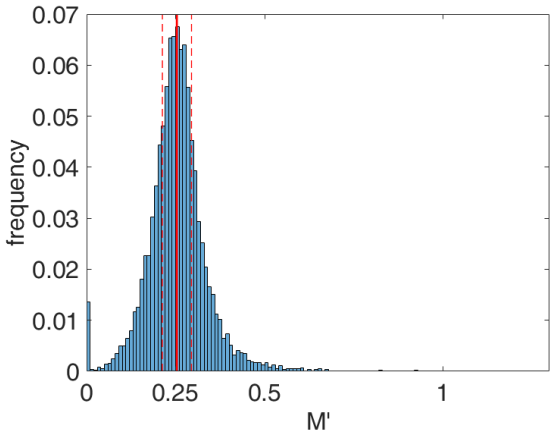

FIGURE 5.8: Histogram of boundary M' values extracted from the time steps shown in Fig. 5.7 by the reverse engineering method. The solid red line indicates the data median, and the dashed red lines mark the boundaries of the second and third quartiles of the data, respectively.

distances yield close-to-zero M' values. Owing to this, calculations of the data median and the quartile boundaries ignore the data in the first bin.

The reduced mobility M' of grain boundaries in real materials is rarely isotropic, usually varying with misorientation and inclination. The question of whether our reverse engineering method is able to resolve such dependencies is vital to the analysis of experimental datasets. A new type of simulation is proposed for such a validation, in which the boundary energy and mobility take on anisotropic values.

The initial microstructure for the anisotropic simulation was the same as in the isotropic case. Values for M' were set to depend on the boundary misorientation as plotted in Fig. 5.9, where the dependency has a triangle shape and a peak at 30°. In order to utilize the boundary misorientation in the determination of M' values, additional information—grain orientation—must be assigned to individual grains. Such an assignment followed the algorithm described in Sec. 2.1.1.1. The resulting boundary misorientation distribution manifests a shape close to that of the Mackenzie distribution (Fig. 5.10 (a)). The simulation with anisotropic M' values began only after a transitional stage with isotropic M' from $t = 0$ to 175. The changes in grain number and average grain size during the simulation are plotted in Fig. 5.10 (b).

Just as before, microstructures at seven timesteps were selected for the reverse engineering analysis, with the time interval remaining at 60. For each interval, the M' of individual grain boundaries was calculated. Because the input M' depends on grain boundary misorientation, I plotted the calculated M' values against misorientation. In the histogram of Fig. 5.11, the bin height shows the value of the median M' of data

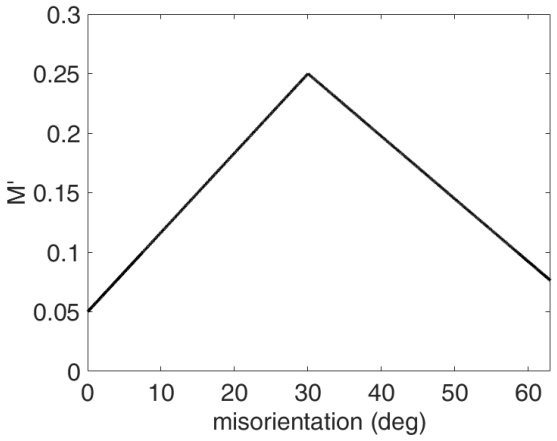

FIGURE 5.9: Dependence of M' on boundary misorientation, which served as the input to a phase field simulation of anisotropic grain growth.

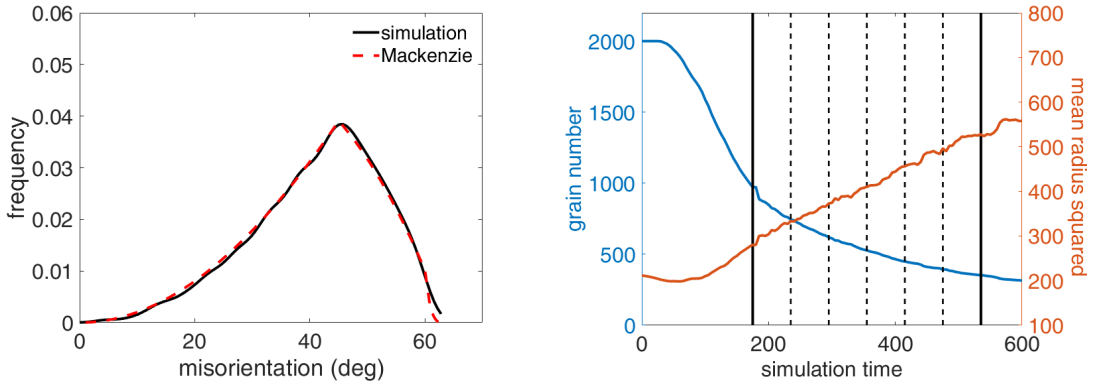

(a) (b)

FIGURE 5.10: (a) The distribution of boundary misorientations in the synthetic microstructure follows closely the Mackenzie distribution [56]. (b) Grain number and mean radius squared *vs.* simulation time. The anisotropic simulation began at $t = 175$, following an initial run of isotropic grain growth.

points lying within the bin range. The results manifest a triangular shape for the dependency of M' on misorientation. When compared with the simulation input, the two plots show great similarity, as evidenced by the fact that the solid line passes through most of the bin centers. The fifth bin (center at 27.9°) has the highest M' at 0.2352, which is close to the peak of the input M'. The agreement is less pronounced for the first two bins and the last bin. This can be attributed to the poor statistics in these bins. As shown in Fig. 5.10 (a), boundary populations are low for the misorientation ranges of these bins. This validation of the simulation for anisotropic M' demonstrates that the reverse engineering method is able to extract possible dependencies of M' on grain boundary parameters during grain growth.

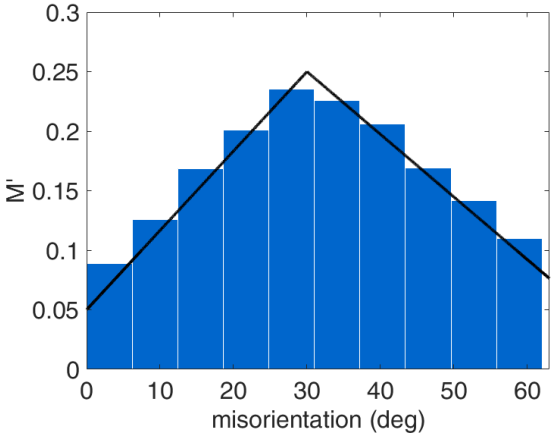

FIGURE 5.11: Values of M' extracted from the anisotropic grain growth simulation of Fig. 5.10 (b) and mapped against misorientation. The result reproduces the triangular shape of the simulation input M' (solid black lines).

5.4 A guide to experimental design

At the end of this chapter, I comment on the design of time-resolved 3D data measurements so that such experiments can yield suitable datasets for a reverse engineering analysis of the boundary M'. This is an important practical issue, as experimental time is limited by the available beamtime at synchrotron sources. Additionally, for optimal use of each dataset, complex and time-consuming reconstructions must be carried out. Careful design of the 4D measurements in advance helps to maximize the amount of information that they provide.

Intuitively, both temporal and spatial resolution play a role in the final data quality. For example, if the time interval between two measured microstructures is too long, we lose information regarding the exact time when a boundary vanishes; however, when the time intervals are too short, the boundary migration distances are so small that we must spend a considerable overall amount of beamtime to record adequate growth in one sample. The evolution of microstructure in a computer simulation can be considered to be continuous.[2] Also, the spatial resolution of the synthetic microstructure can be adjusted. Hence, the influence of both parameters can be evaluated before carrying out experimental studies.

During method validation, we set the time interval Δt for reverse engineering of the isotropic simulations to 60. To evaluate the influence of Δt, such results are compared to cases where Δt was set to 5, 30, 120 and 180. For all tests, the reverse engineering method was applied starting from the microstructure captured at $t = 175$, with the first

[2]In simulations, the temporal discretization parameter can be set much smaller than the shortest annealing interval that is feasible to achieve experimentally.

two time intervals after $t = 175$ being used to estimate the boundary M'. For each Δt, the histogram of boundary M' values is plotted in Fig. 5.12. The data median, the 25th percentile and the 75th percentile are marked in each histogram.

The effect of the choice of Δt is quantified in Fig. 5.13 (a), where the median and data spread are plotted against Δt. For different Δt, the median remains close to the simulation input of 0.25, ranging from 0.2157 to 0.3066. Nevertheless, there is a trend that M' decreases with greater Δt, while the spread in data slightly increases. This can be explained by considering the number of data points that enter into each histogram. Figure. 5.13 (b) plots the number of grain boundaries (GBs) being analyzed by the reverse engineering method for different values of Δt. The number of GBs decreases dramatically for larger Δt due to the fact that, when Δt is large, more boundaries vanish within one time interval and are left out of the analysis. It is worth noting that the number of GBs is even smaller for Δt=5. At such a high temporal resolution, many GBs undergo fairly small displacements, and are, therefore, eliminated from the analysis because they violate the swept volume threshold. Considering both factors, we conclude that a moderate temporal resolution is optimal for experiments in order to capture significant boundary migration, while avoiding the disappearance of too many grains.

For a given temporal resolution, if an experiment is performed at higher spatial resolution (by lowering the grid spacing Δx), the estimation of M' for boundaries that undergo small migrations is more accurate. In a sense, this is equivalent to an increase in the temporal resolution. However, the spatial resolution is usually restricted by the experimental technique and setup (*e.g.,* in 3DXRD microscopy, the Δx value of a measurement is determined by the spatial resolution of the near-field detector). To qualitatively demonstrate the influence of Δx on the analysis, we consider the case when Δx is doubled for a simulation of isotropic grain growth, with Δt set to 60. The results of the boundary M' values for $\Delta x = 2$ are plotted in the histogram of Fig. 5.14. Compared to the results obtained when $\Delta x = 1$ (Fig. 5.12 (c)), the histogram has a higher first bin, because more boundaries fall into the bin of smallest migration when $\Delta x = 2$. The data median shifts from 0.2535 to 0.3158 for $\Delta x = 2$, which is further away from the simulation input of 0.25. In addition, a broader distribution is observed for $\Delta x = 2$.

It is noteworthy that Δx plays a role not only in the estimation of boundary migration velocity but also in the determination of boundary curvature. At low spatial resolution, boundaries exhibit sharp corners arising from the underlying grid. These lead to a less accurate estimation of the mean curvature, which, in turn, results in errors in the estimation of the boundary M'. A good spatial resolution is one of the key parameters for the reverse engineering extraction of boundary M' values. Since the absolute spatial

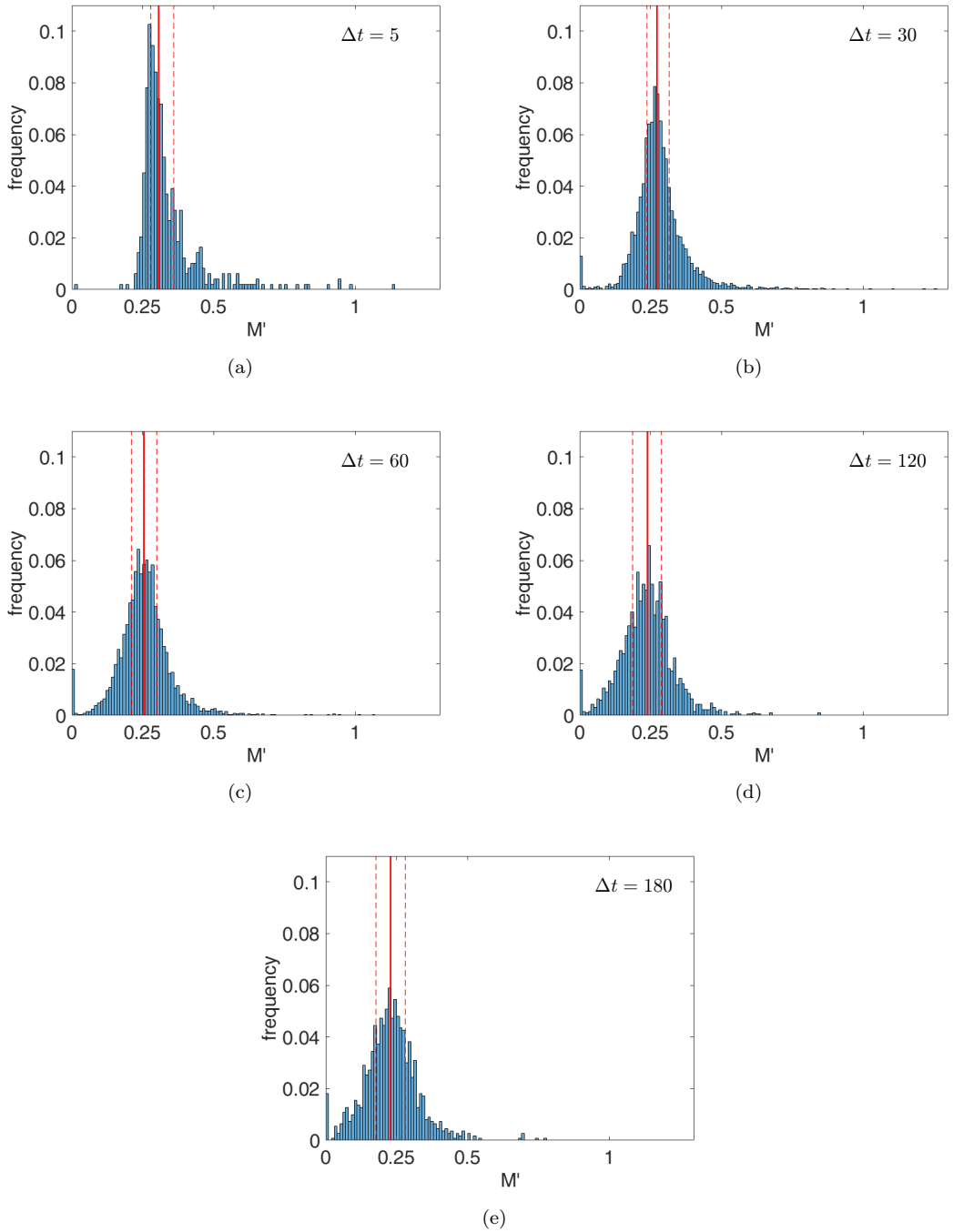

(a) (b) (c) (d) (e)

FIGURE 5.12: Histograms of boundary M' values calculated by the reverse engineering method using Δt = 5, 30, 60, 120 and 180. In each histogram, the solid red line indicates the data median. The spread of the data is quantified by the boundaries of the second and third quartiles (dashed red lines).

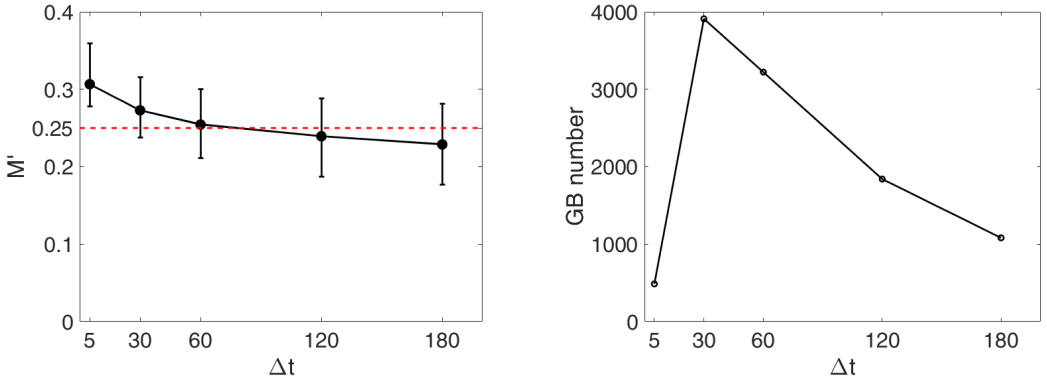

(a) (b)

FIGURE 5.13: (a) Comparison of the data median and spread of the histograms of Fig. 5.12 plotted against Δt. (b) The number of GBs analyzed as a function of Δt.

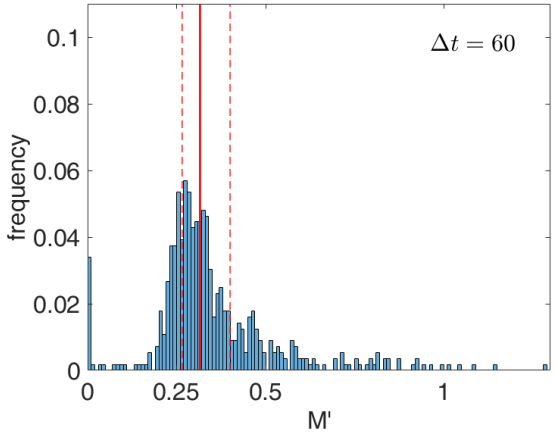

FIGURE 5.14: Histogram of grain boundary M' values extracted from the synthetic microstructure when Δx is set to 2. The results can be compared to the histogram of Fig. 5.12 (c), which was obtained at the same temporal resolution but at a higher spatial resolution (Δx = 1). The data median, 25th percentile and 75th percentile are marked with red lines.

resolution is limited by the experimental setup, one often aims to improve the relative spatial resolution by increasing the average grain size in the specimen so that the grain boundaries can be better resolved by 3DXRD microscopy. From a practical standpoint, the latter strategy must consider the fact that a reasonable number of grain boundaries must remain in the irradiated sample volume in order to yield a statistically significant number of data points for later analysis.

Chapter 6

Coarsening in an Al-Mg Alloy

In the previous chapter, a method to retrieve the reduced grain boundary mobility M'—namely, the reverse engineering method—was established. This method was tested against simulations with isotropic and anisotropic boundary properties, and the results confirmed that, when implemented correctly, the method is capable of extracting M' for individual GBs from sequential snapshots of a 3D microstructure. In this chapter, I apply the reverse engineering method to experimental grain growth occurring in an Al-1 wt% Mg specimen. The sample preparation and the experimental details are presented at the beginning of this chapter, followed by the extraction of microstructural characteristics at the grain and grain boundary levels. In the end, the dependency of M' on the mesoscopic properties of grain boundaries is investigated.

6.1 Sample preparation and 4D data acquisition

The Al-1 wt% Mg specimen (referred to as AlMg) was prepared by Prof. Dmitri Molodov from RWTH Aachen. Cylindrical samples were cut out via spark erosion of an Al-1 wt% Mg plate, which had been cold-rolled to 50% reduction in thickness. Before grain growth experiments, the specimen was recrystallized at 350°C for 75 min. The final sample for measurements had a diameter of 1.4 mm and a height of 6 mm.

The 3D microstructure of the AlMg specimen was mapped using 3DXRD microscopy on beamline BL20XU at the Japanese synchrotron radiation facility SPring-8. These measurements were carried out and published by Dake *et al.* [198]. Some important experimental parameters are summarized here: The incident box beam had a size of 1600 μm in width and 300 μm in height. The x-ray energy was set to 32 keV. The angular step $\Delta\omega$ was 0.48° for the collection of far-field and near-field diffraction peaks.

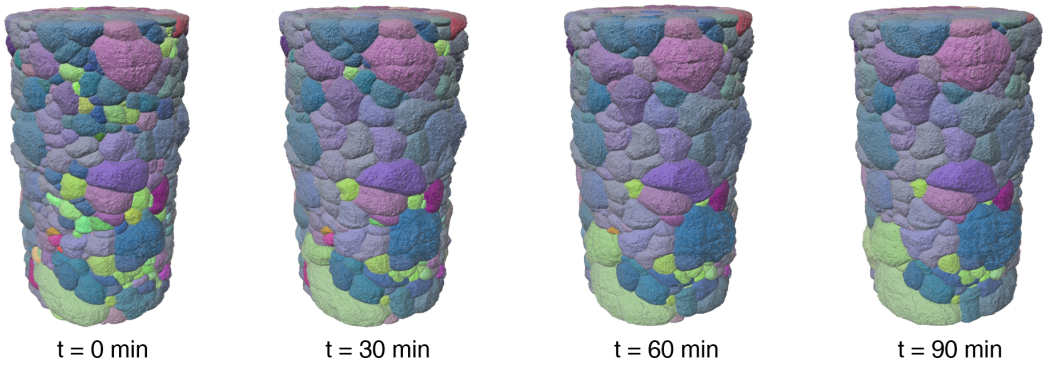

FIGURE 6.1: 3D microstructural evolution in an AlMg specimen annealed at 400°C for the indicated times. Grains are colored according to the Rodrigues representation of their orientation.

The illumination time for each $\Delta\omega$ was 1 s for far-field images and 0.1 s for near-field images. In total, ten adjacent layers were collected, with a layer height of 300 μm and an overlap between layers of 50 μm. The total measured height of the specimen was 1.55 mm.

The AlMg sample underwent several annealing sequences during previous investigations of grain growth. For a detailed annealing history, readers are referred to Ref. [198]. In this thesis, I focus on the final sequence of annealing at 400°C that was carried out by Dake *et al.*, because the temporal and spatial resolution of this final dataset is suitable for reverse engineering analysis. The 3D microstructure of the sample was mapped by 3DXRD microscopy after each 30 min *ex situ* heat treatment. In total, four snapshots of the sample were available as reconstructed datasets.

6.2 Microstructural evolution at the grain level

In this section, I focus on the microstructural characteristics of the AlMg sample at the grain level. Figure 6.1 shows the reconstructed 3D microstructure at different timesteps. After 90 min of annealing, significant grain growth took place, as seen in the change in the number of grains (Fig. 6.2 (a))—the number drops from 1320 at $t = 0$ to 618 at $t = 90$ min. In Fig. 6.2 (b), the square of the mean grain size $\langle R \rangle^2$ is plotted against annealing time t. In Sec. 2.2, we discussed that a linear relationship between $\langle R \rangle^2$ and t is expected for normal grain growth. A clear deviation from this linear prediction is observed for grain growth in the AlMg specimen, as shown in Fig. 6.2 (b). Here, growth seems to slow down, as the data point at $t = 90$ min lies well below a linear extrapolation of the first three data points.

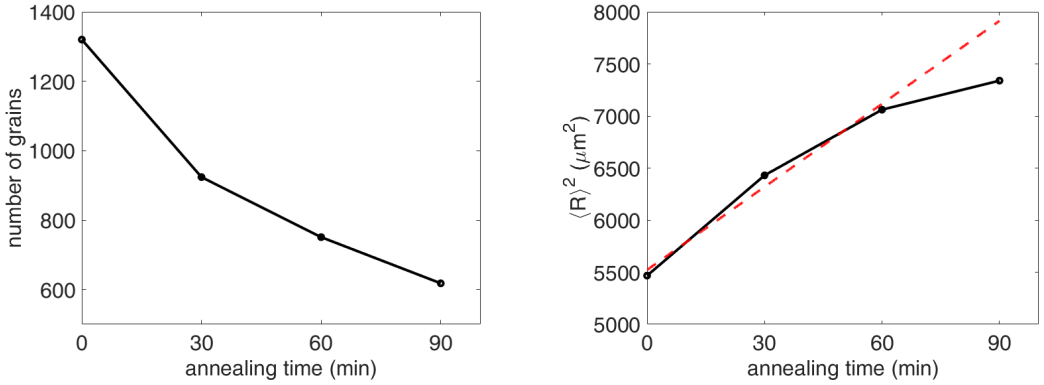

(a) (b)

FIGURE 6.2: (a) Plot of the number of grains in the AlMg specimen during an isothermal anneal at 400°C. (b) Square of the mean grain size plotted against annealing time. The dashed red line is a least-squares fit of a straight line to the first three data points in the plot.

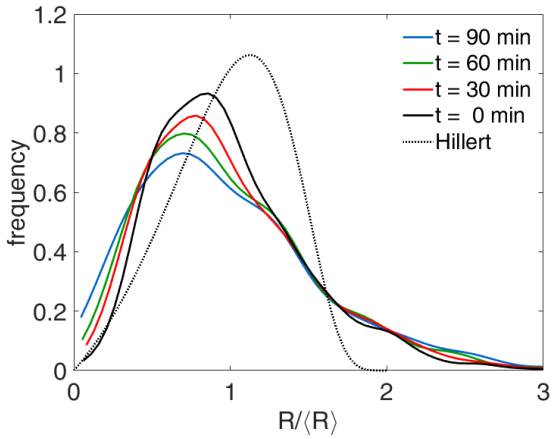

FIGURE 6.3: Evolution of the grain size distribution (GSD) in the AlMg specimen annealed at 400°C. The GSDs are compared to the mean-field prediction of Hillert [103].

From the volume of individual grains, the grain size distribution (GSD) of the AlMg sample can be calculated for each timestep. The radius R of an individual grain is calculated as the radius of a sphere of equal volume. The resulting GSDs are plotted in Fig. 6.3. Considering that the x-axis is the normalized grain radius $R/\langle R\rangle$, the GSDs should exhibit a time-invariant shape for normal grain growth. However, in Fig. 6.3, the GSD peaks are found to shift to the left with increasing annealing duration.

All deviations mentioned above point to the possibility of the occurrence of abnormal grain growth in the AlMg specimen. Examination of the time-resolved microstructure reveals the coarsening of individual grains. Figure 6.4 shows the microstructural evolution that occurs in an xy cross section ($z = 430$). For clarity, grain boundaries in the micrographs are marked in black. On the right side of the cross section, changes in grain

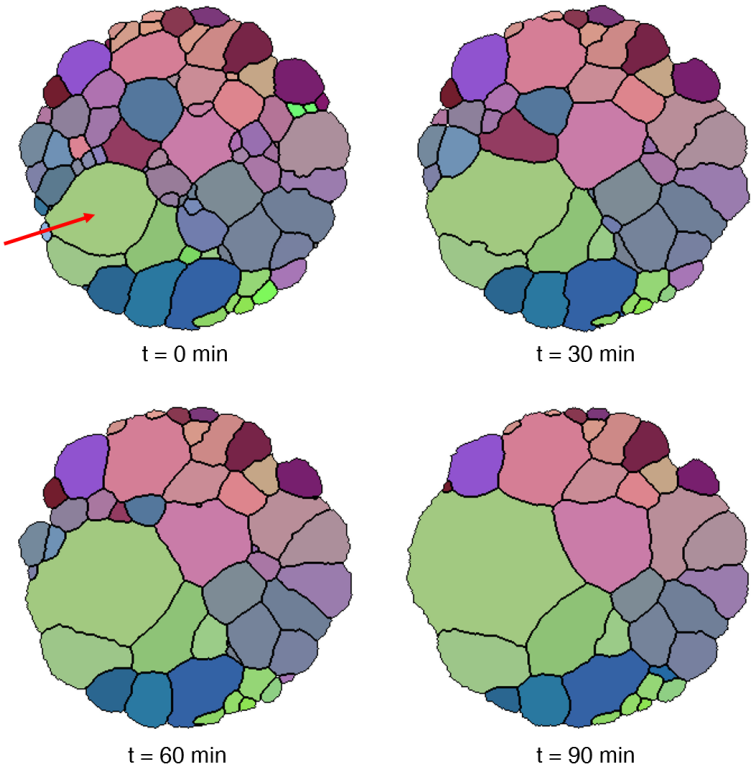

FIGURE 6.4: Microstructural evolution in the AlMg at 400°C, shown in a single xy cross-section ($z = 430$). Grain boundaries are marked in black.

size appear to correspond more-or-less to normal grain growth, whereas some grains on the left side of the cross section grow unexpectedly large. It is clear that, after 90 min of annealing, the green grain indicated by the red arrow grew to a much larger size than the other grains.

To quantify this observation, the radii of the grains that appear in these images are plotted against annealing time in Fig. 6.5 (a). Note that R is calculated from the spherical equivalent radius of the grain volume in 3D, rather than from the grain area visible in the cross section. Growth of the green grain is marked in green in Fig. 6.4. The black data points and line illustrate the mean grain size $\langle R \rangle$ in the sample. According to the mean-field model for grain growth in 3D, a grain that is smaller than $R_c = (9/8)\langle R \rangle$ ought to shrink [103]. This is true for most of the grains in the AlMg specimen; however, some grains with sizes larger than R_c also shrink and eventually vanish, as shown by trajectories that start out well above the black line and then cross other ones while dropping to zero.

For a given grain size trajectory, the growth rate of an individual grain, dR/dt, can be estimated from discretized data points using a central difference approach:

$$\frac{dR}{dt} = \frac{R_{i+1} - R_{i-1}}{t_{i+1} - t_{i-1}}, \tag{6.1}$$

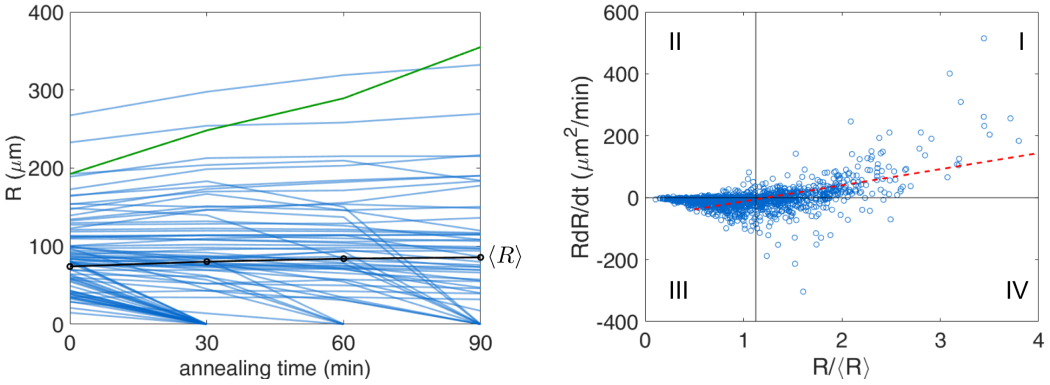

FIGURE 6.5: (a) Size trajectories of the grains shown in the cross section of Fig. 6.4. The green trajectory corresponds to the large green grain marked by the red arrow. The black data points denote the evolution of the mean grain radius of the sample. (b) The scaled growth rate $R \cdot dR/dt$ of the individual grains in (a), plotted against the normalized grain radius $R/\langle R\rangle$.

in which R_i, R_{i-1} and R_{i+1} denote the grain radius at timesteps t_i, t_{i-1} and t_{i+1}, respectively. If both sides of Eq. 2.22 are multiplied by R and R_c is replaced by $(9/8)\langle R\rangle$, we obtain

$$R\frac{dR}{dt} = \frac{8}{9}M\gamma\left(\frac{R}{\langle R\rangle} - \frac{9}{8}\right). \tag{6.2}$$

The scaled growth rate $R \cdot dR/dt$ is a linear function of $R/\langle R\rangle$ passing through the point (9/8,0). Since the prefactor $M\gamma$ in Eq. 6.2 is positive, if $R > (9/8)\langle R\rangle$, $R \cdot dR/dt$ is positive—thus the grain grows; if $R < (9/8)\langle R\rangle$, $R \cdot dR/dt$ is negative and the grain shrinks.

We investigate this relationship in Fig. 6.5 (b) by plotting $R \cdot dR/dt$ for individual grains against the corresponding value of $R/\langle R\rangle$. We separate the plot into four quadrants using $R \cdot dR/dt = 0$ and $R/\langle R\rangle = 9/8$. If the relationship predicated by Eq. 6.2 holds, the scattered data points should lie in quadrants I and III, and a linear regression through the data points should go through the point $R \cdot dR/dt = 0$ and $R/\langle R\rangle = 9/8$. In Fig. 6.5 (b), the red dashed line indicates a least-squares linear fit of the data points. It intersects $R \cdot dR/dt = 0$ at $R/\langle R\rangle = 1.23$, which is close to the theoretical value of 9/8. However, a considerable number of points lie in quadrant IV, indicating that some large grains that ought to have grown, according to the mean-field model, have in fact shrunk in the experiments. We also notice that the data points are rather scattered about the linear fit. This is especially true for the grains with large R, for which the scaled growth rates are well beyond their linear predictions. From the growth of individual grains, it is concluded that the mean-field theory alone cannot explain the grain growth that took place in the AlMg specimen.

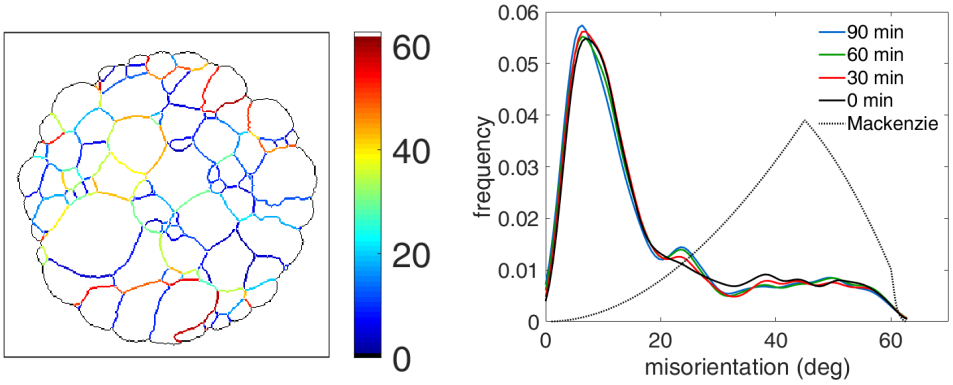

(a) (b)

FIGURE 6.6: (a) Grain boundary misorientations for the first cross section shown in Fig. 6.4. Grain boundaries are colored by their misorientation angles. (b) Misorientation distribution of GBs in AlMg for different timesteps. The distributions are compared to the Mackenzie distribution derived from a random assembly of crystallites.

6.3 Microstructural evolution at the grain boundary level

Grain growth in the AlMg specimen can be investigated at the grain boundary (GB) level, as the boundaries and their associated properties can be extracted from the time-resolved 3D microstructure. For the microstructures shown in 3D (Fig. 6.1) and 2D (Fig. 6.4), the colors of grains are found to be far from randomly distributed—there are regions where nearby grains share similar colors. Since the color denotes the grain orientation derived from the Rodrigues vector, grains of similar colors ought to have similar orientations. The misorientation of each GB is calculated from the orientations of the two adjacent grains. In Fig. 6.6 (a), the same microstructure is shown as in Fig. 6.4, but here the GBs are colored by the misorientation angle. It is found that boundaries in blue are dominant in the cross section. To visualize the misorientation of all boundaries in the specimen, we plot the misorientation distribution in Fig. 6.6 (b). Note that the contribution of each boundary to the distribution is weighted by the corresponding boundary area. Compared to the Mackenzie distribution, which describes a random assembly of grains, the results demonstrate a much higher frequency of low-angle grain boundaries (LAGBs) in the AlMg specimen. In addition, the distributions are shown for all timesteps in Fig. 6.6 (b). The distributions follow a similar pattern, even though the microstructure changes dramatically over the course of the heat treatment.

Although high-angle grain boundaries (HAGBs) are not dominant in the sample, we examine the population of some special HAGBs, *i.e.,* CSL boundaries, as they may possibly exhibit rather different behavior during boundary migration. The criterion for proximity to a CSL boundary is given by the Brandon criterion of Eq. 2.11. In Fig. 6.7, the frequencies of CSL boundaries in AlMg are plotted against Σ up to 23. Values

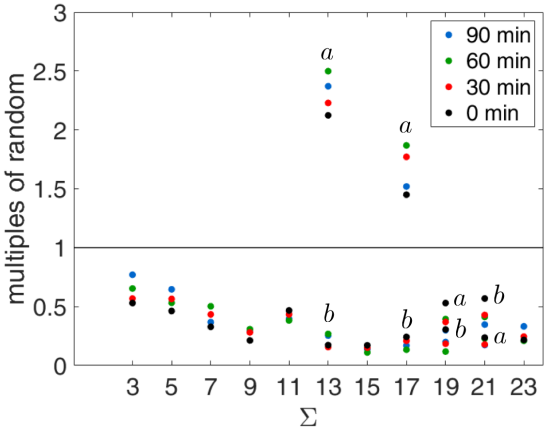

FIGURE 6.7: Relative frequency (in multiples of a random distribution) of CSL boundaries in AlMg at different annealing steps. The measured values for most CSL types lie well below the expected value of unity. The labels "a" and "b" distinguish between different CSL boundary types having the same Σ value.

on the y-axis are quoted in multiples of a random distribution (MRD), showing the relative frequency compared to that of a random assembly of grains (Fig. 2.7). The MRD vales are plotted in different colors for different annealing timesteps. Except for $\Sigma 13a$ and $\Sigma 17a$ boundaries, the frequencies of all CSL types are smaller than those of a random assembly.[1] By summing up the total number of all CSL types, we find that CSL boundaries make up only 5.16%, 5.38%, 5.69% and 5.98% of the overall boundary population at t=0, 30 min, 60 min and 90 min, respectively. Based on this analysis, we expect CSL boundaries to play at most a minor role during coarsening in the AlMg specimen, for which most boundaries are LAGBs and general HAGBs.

In addition to boundary misorientation, the boundary inclination can be estimated from the extracted network of grain boundaries in the specimen. In Sec. 5.2, I presented an approach to estimating GB curvature from a surface mesh of grain volumes. The same software DREAM3D gives the normal direction of each patch in the mesh. Ignoring the normal vectors for patches that are on or close to triple lines, we calculate the area-weighted average boundary inclination $\langle \mathbf{n} \rangle$ as

$$\langle \mathbf{n} \rangle = \frac{\sum \mathbf{n}_i A_i}{\sum A_i}, \tag{6.3}$$

where $\mathbf{n_i}$ denotes the normal vector of patch i, and A_i is the corresponding patch area. Following the routine described in Sec. 2.1.1.2, the inclination of each boundary can be specified in coordinate systems attached to the two adjacent grains. The results are plotted in the [001] pole figures of Fig. 6.8.

[1] Even for the CSL boundaries of highest frequency—$\Sigma 13a$ and $\Sigma 17a$—the absolute frequency of occurrence is quite low: 0.62% for $\Sigma 13a$ and 0.28% for $\Sigma 17a$.

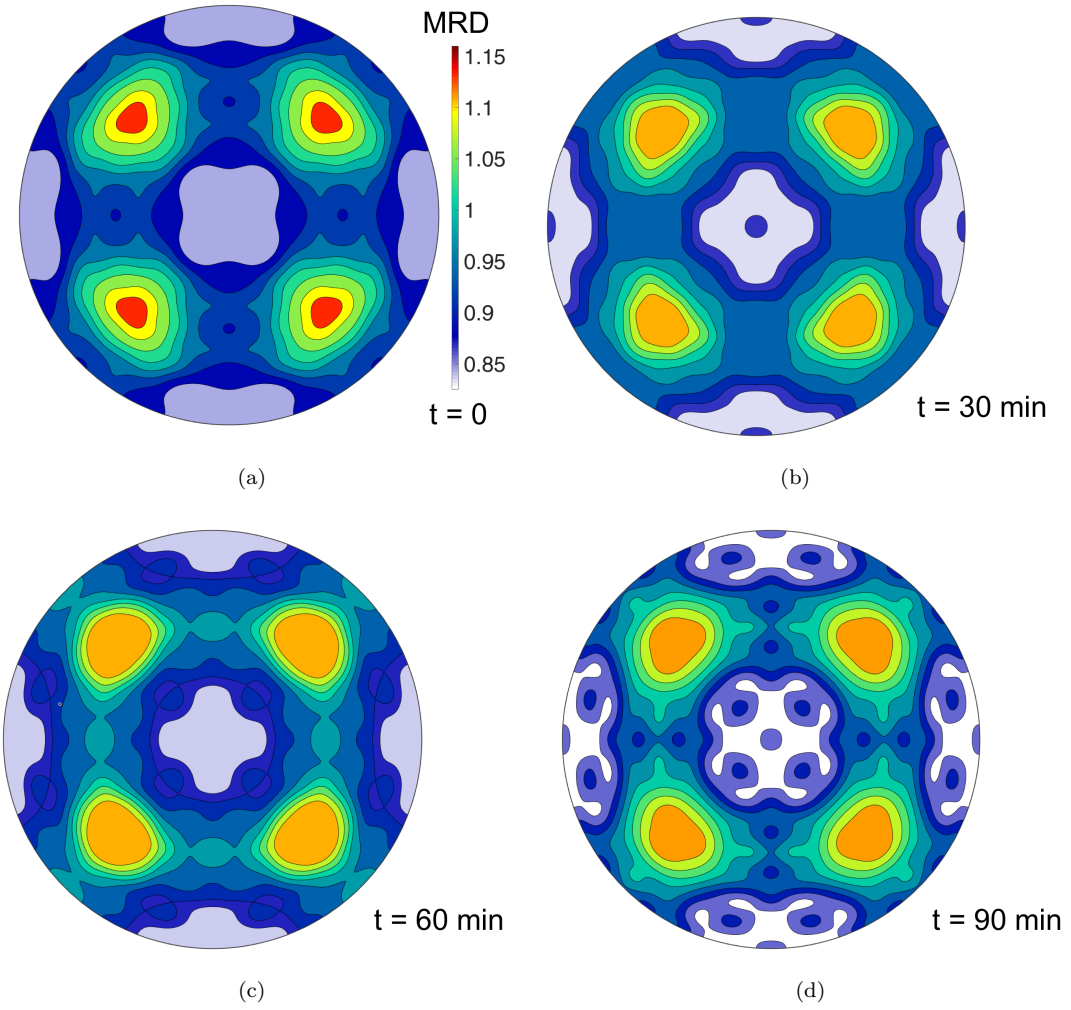

FIGURE 6.8: Grain boundary inclination distribution in AlMg annealed at 400°C for the indicated times, plotted on a [001] pole figure. The colors are indexed to the frequency of planes for an ensemble of randomly oriented FCC crystallites.

At $t = 0$, the pole figure shows peaks located at $\langle 111 \rangle$ poles. According to the equilibrium phase diagram [211], Al-1 wt% Mg has a face-centered cubic (FCC) crystal structure. For FCC materials, the $\{111\}$ planes are close-packed planes that are known to have the lowest surface/interfacial energies. Considering the inverse relation between the GB energy and the GB population revealed in various references [7, 8, 88, 91, 92], the $\langle 111 \rangle$ peaks in the pole figures are expected. Such peaks in the inclination distribution coincide with findings in other FCC materials, such as pure Al [7, 92] and $MgAl_2O_4$ [7]. Moreover, the MRD values of the overall inclination distribution are distributed between 0.85 and 1.15, which is close to the ranges of [0.86, 1.25] in pure Al [7, 92] and [0.7, 1.78] in $MgAl_2O_4$ [7]). In Fig. 6.8, we can also follow the change in inclination distribution of the specimen during the 90-min anneal. The peaks for $\{111\}$ planes are found to decrease somewhat in intensity with the annealing duration.

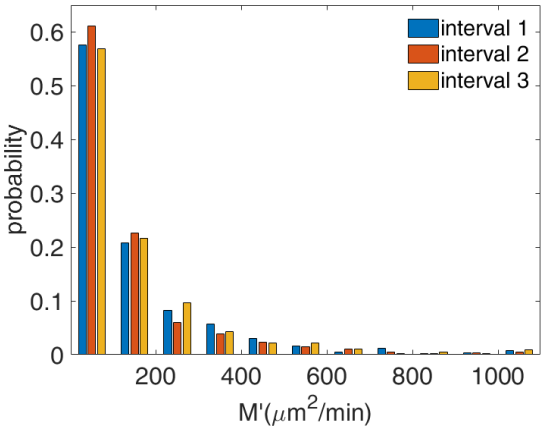

FIGURE 6.9: Reduced grain boundary mobility M' as estimated by the reverse engineering method for three annealing intervals of the AlMg specimen at 400°C.

6.4 Reverse engineering the grain boundary M'

Using two sequential 3D microstructural mappings, we are able to extract the reduced mobility of individual grain boundaries in the AlMg specimen. With the reverse engineering method proposed in Chap. 5, reduced mobilities are calculated for all three 30-min annealing intervals, and the results are plotted in the histograms of Fig. 6.9. All three histograms show a similar trend: Around 80% of the boundaries have reduced mobility in the range from 0 to 200 $\mu m^2/min$. The similarity between different annealing intervals is expected, because the sample was annealed at the same temperature in each interval. In this analysis, therefore, I focus on the common features instead of the insignificant differences between various intervals. This approach also provides for a more robust analysis, since the statistics are improved.

As presented in the previous section, grain boundaries in the AlMg specimen show large variations in misorientation. The predominance of LAGBs may result in an inhomogeneous distribution of M' for the boundaries of AlMg. In order to investigate the dependency of M' on misorientation, the M' of each grain boundary is indexed to the corresponding boundary misorientation. Instead of plotting individual data points, I plot the data in the form of a histogram (Fig. 6.10) in which data points are grouped by their misorientations. The height of each bin represents the median M' value recorded within the corresponding bin's range.

The histogram shows that M' tends toward higher values for larger misorientation until reaching a peak around 35°. According to the Read-Shockley model for LAGBs [61], the dislocation density at a boundary increases as its misorientation increases, which results in a higher boundary energy. This relationship is reflected in the dependency of M' on misorientation. Nevertheless, the angular limit θ_m for this increase (which

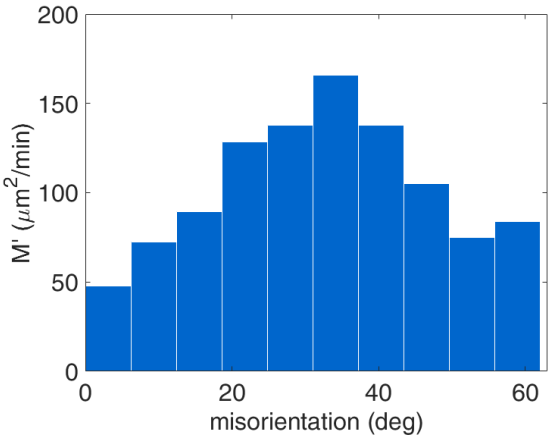

FIGURE 6.10: Reduced boundary mobility M' in the AlMg specimen indexed to boundary misorientation.

equals the upper misorientation limit of LAGBs) in the AlMg specimen (35°) is larger than the value (15°) commonly quoted in the literature ([3, 61, 64–66]). From Eq. 2.9, boundaries are expected to have constant energy γ_m at misorientations greater than θ_m. In AlMg, however, M' surprisingly decreases above θ_m and continues to drop with increasing misorientation.

A similar decrease in boundary energy was measured for HAGBs in Cu, as presented in Refs. [8, 212, 213]. The authors attributed the drop to the presence of coherent twin ($\Sigma 3$) boundaries. However, since the stacking fault energy in Al in higher than in Cu [3], twinning should be rather limited in the AlMg sample; this agrees with the low frequency of $\Sigma 3$ boundaries plotted in Fig. 6.7. In addition, the possibility of low M' arising from CSL boundaries is unlikely, as the bin height of the histogram represents the data median (rather than, say, the average). This notion is confirmed in the histogram of Fig. 6.11, in which CSL boundaries are excluded. Compared to the original histogram shown in Fig. 6.10, the two histograms manifest no significant differences. Thus, we can conclude that the drop in M' for HAGBs in the AlMg specimen is not due to the presence of CSL boundaries.

In Fig. 6.12, the dependency of M' on boundary inclination is presented. Plotted on a [001] pole figure, M' is found to have relatively low values at the $\langle 111 \rangle$ poles. Considering the high frequency of $\{111\}$ planes in the boundary population (Fig. 6.8), the local minima in M' at $\{111\}$ in Fig. 6.12 are consistent with an inverse relationship between boundary energy and boundary population [7, 8, 88, 91, 92]. The values for the normalized M' range from 0.8 to 1.15 (an increase of only 44% from the minimum to maximum value), suggesting that the reduced mobility in AlMg is not very strongly dependent on boundary inclination. In contrast, M' varies greatly with respect to the

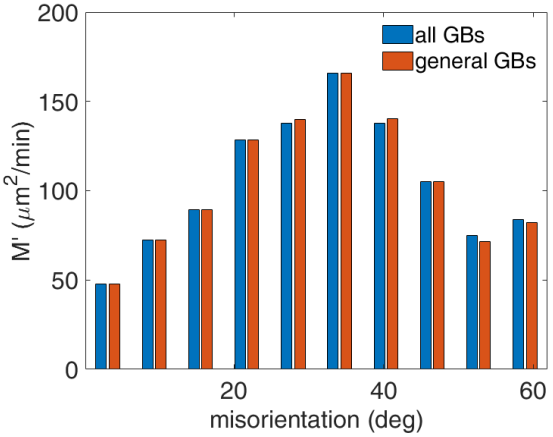

FIGURE 6.11: The dependencies of M' on misorientation are compared for all boundaries in the AlMg specimen (blue) and general boundaries (red), from which CSL boundaries $\Sigma 3$ and higher have been excluded.

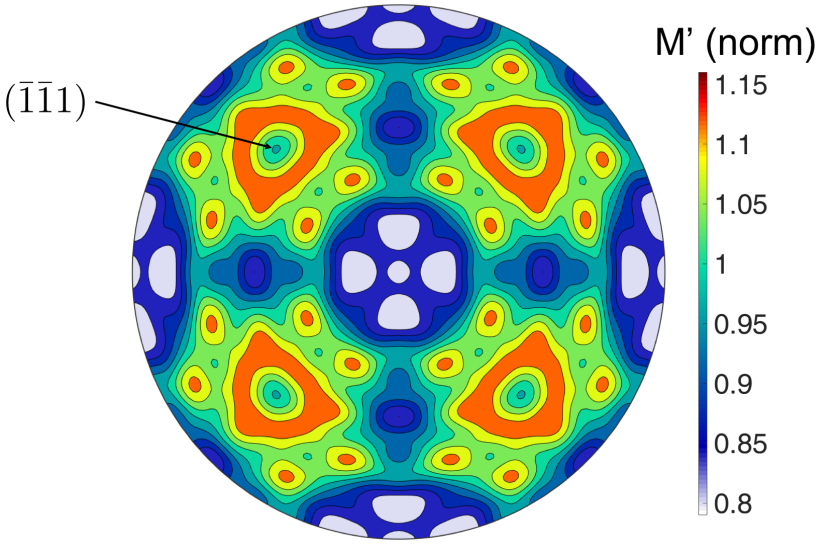

FIGURE 6.12: Values for M' (normalized such that the area weighted average is equal to unity) indexed to the GB inclination in AlMg and plotted in a [001] pole figure.

grain misorientation—as shown in Fig. 6.10, where the bin height ranges from a low of around 50 μm^2/min to a high of over 150 μm^2/min.

Figure 6.10 clearly illustrates the general dependence of M' on the boundary misorientation, but, because the median is used to represent the bin height, the actual data spread of each bin is absent. In order to show this data spread, I utilize a combination of violin and box plots. In a violin plot, the data distribution in each bin is estimated by a kernel density function. By plotting the estimated distribution vertically and reflecting the frequency across the midline of the bin, one can present the spreads in different bins simultaneously. In a box plot, the bottom and the top line of a box (also known as the lower and upper hinge) mark the 25th and 75th percentiles of the data, respectively.

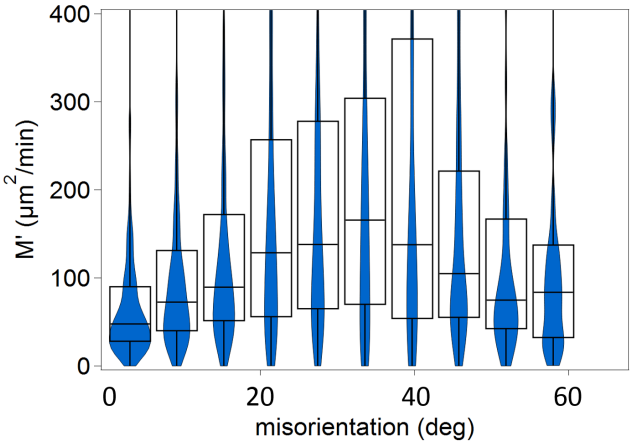

FIGURE 6.13: The distribution of data in the histogram of Fig. 6.10, represented by a superposition of violin and box plots.

In Fig. 6.13, I superpose a box plot on the violin plot calculated from the histogram of Fig. 6.10. The spread of the data is quite large—all violins have long necks, and in some bins the 75th percentile is twice as large as the median. We quantify the spread by defining the relative data spread to be the distance from the lower/upper hinge to the median divided by the median value. When averaged across all bins, the relative spread of M' in the AlMg specimen is calculated to range from -52.4% to 102.3%.

6.5 Discussion and final remarks

6.5.1 A case study

An example of an abnormally growing grain is presented in the micrographs of Fig. 6.4. The green grain marked by the red arrow (Grain ID = 1017) manifests rapid growth during annealing, as evident by its grain size trajectory plotted in Fig. 6.5 (a). Figure 6.6 (a) gives a glimpse of the boundary misorientation of this grain in a 2D cross section. All boundary misorientations of Grain 1017 are summarized in Table 6.1. Neighboring grains and the associated misorientations are listed in the first two columns. In the third column, the reduced mobilities are presented. If a boundary survives more than one annealing interval, M' is assigned to the average value of all intervals. In Fig. 6.14, I plot M' against misorientation using the data given in Table 6.1. It is clear that the grain boundaries of Grain 1017 are separated into two populations: boundaries with misorientations smaller than 10° with small M', and boundaries with misorientations larger than 30° and typically large values of M'. On the same plot, the 25th, 50th and 75th percentiles shown in the box plot of Fig. 6.13 are marked in red. It is noteworthy that the large-misorientation boundaries of Grain 1017 have M' values that

lie well beyond the top hinge of the corresponding box. Such fast-migrating boundaries are responsible for the rapid growth of Grain 1017 at the grain level.

Grain ID	misorientation (°)	M' (μm^2/min)	distance to 38.2°/⟨111⟩ (°)	distance to 40.5°/⟨111⟩ (°)
956	40.4	392.7	9.9	9.9
998	4.5	61.1	35.4	37.7
1171	41.4	2468.3	26.1	26.6
950	41.7	632.2	7.3	6.6
952	24.3	618.2	19.5	21.5
970	42.7	824.3	23.5	23.8
1008	4.2	134.3	34.2	36.5
1011	33.7	292.7	8.3	9.9
1084	43.1	1017.0	12.9	12.5
1097	3.9	108.2	34.6	36.9
1104	32.9	265.4	15.6	16.8
1197	37.5	2140.9	25.6	26.5
862	38.0	1472.9	16.2	16.8
1012	34.8	156.5	16.5	17.5
1143	32.6	408.6	23.4	24.7
1153	32.5	55.5	21.7	23.0
1169	32.6	605.6	23.4	24.6
1222	34.6	388.7	27.6	28.8
1226	41.2	1710.1	14.7	14.8
1249	34.2	317.7	28.2	29.4

TABLE 6.1: Misorientations and estimated M' values for the grain boundaries of Grain 1017 (green grain marked with a red arrow in Fig. 6.4). Columns 4 and 5 list the distance from the boundary misorientation to $\Sigma 7$ (38.2°/⟨111⟩) and 40.5°/⟨111⟩, respectively.

In Refs. [1, 3, 214, 215], the authors measured the boundary mobility against the boundary misorientation in high-purity aluminum alloys. A maximum in the vicinity of $\Sigma 7$ (38.2°/⟨111⟩) boundaries for mobility was observed. The peak was found to shift to 40.5°/⟨111⟩ at a high temperature. The misorientation angle of this reported fast boundary is close to what was measured for the boundaries of Grain 1017. Thus, I evaluated the proximity to these reported boundary types by calculating the distances (in orientation space) from each GB's misorientation to 38.2°/⟨111⟩ and 40.5°/⟨111⟩.[2]

[2]We calculate this distance in the spirit of the Brandon criterion (to which the distance will be compared) by holding one of the two crystals fixed that form the boundary and then rotating the other crystal until the desired fast-moving boundary is formed. The angle of this rotation is defined to be the distance.

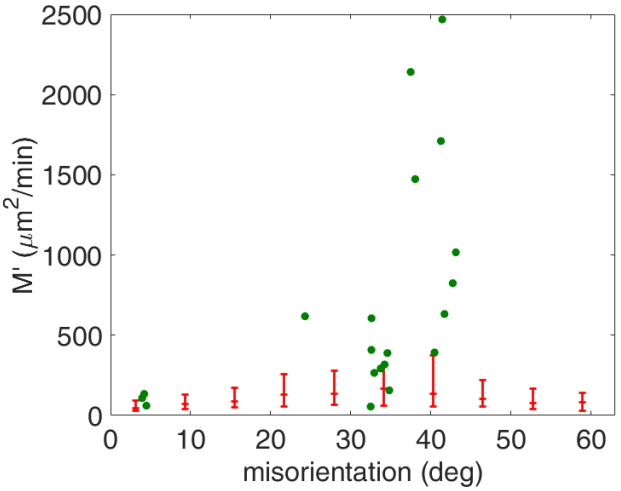

FIGURE 6.14: M' for the individual grain boundaries of Grain 1017. The red markings indicate the 25th, 50th and 75th percentiles of the box plot in Fig. 6.13.

The results are shown in Columns 4 and 5 of Table 6.1. Considering the Brandon criterion for a Σ7 boundary (5.7°), no boundaries of Grain 1017 are close to either of the specified boundary misorientations found in the literature. Therefore, the Σ7 boundary is not responsible for the high value of M'. Furthermore, the population of Σ7 boundaries is less than expected for a random assembly (the corresponding MRD value is smaller than unity in Fig. 6.7), which again suggests that Σ7 boundaries do not explain the unexpectedly large values for M' of some grain boundaries in AlMg.

6.5.2 Final remarks

Microstructural evolution in an Al-5 wt% Mg specimen was captured by 3DXRD measurements. The reconstructed microstructure shows that significant growth took place in the sample. Nevertheless, the growth seems somewhat abnormal: the square of the mean radius is not linearly proportional to the annealing time, and the normalized grain size distributions are not time-invariant during coarsening.

By examinating individual grains, we see that some grains are observed to grow more rapidly than the rest. This is confirmed by the scaled growth rate plot of Fig. 6.5. The scatter of the data points is consistent with the abnormality of grain growth in the specimen. At the grain boundary level, we found a large number of boundaries to have misorientations below 10°. According to the texture-induced AGG mechanism, these LAGBs should be rather immobile, whereas HAGBs in the sample are expected to manifest relatively high migration rates, which could account for some grains growing abnormally large. Besides boundary misorientations, inclinations were also investigated.

Although the boundary inclination is rather homogeneously distributed, the corresponding pole figure shows weak peaks for {111} planes, which is consistent with other such measurements performed on FCC materials.

The texture-induced growth mechanism is supported by the M' values computed by the reverse engineering method. LAGBs are demonstrated to manifest low M', and their reduced mobilities increase with greater boundary misorientation. However, a surprising result is that the M' of HAGBs was found to decrease above a misorientation of about 35°. We ruled out the possibility that certain types of CSL boundaries are predominant in the sample. Nonetheless, the reason for the drop in M' for HAGBs remains unknown. In addition to the dependency of M' on boundary misorientation, M' was also indexed to boundary inclination. An inverse relationship between the boundary population and the M' value was observed for the AlMg specimen.

The aforementioned dependencies of M' on misorientation and inclination are, in a certain sense, average characteristics for the boundaries in the sample. When referenced to individual grain boundaries, the results may show a rather different picture: the violin and box plots of Fig. 6.13 demonstrate that M' exhibits a large spread even within a narrow range of misorientations. Moreover, from the study of individual grains that grew abnormally in experiment, it is found that the GBs of such abnormal grains may have rather extreme values in M' that lie well beyond the 75th percentile of the data. Such fast-migrating boundaries were evidently responsible for the abnormal growth of certain grains in the AlMg specimen.

Chapter 7

Coarsening in an Al-Cu Alloy

In the previous chapter, the grain growth that took place in an Al-1 wt% Mg specimen was discussed. From microstructural characteristics recorded at the grain and grain boundary levels, considered together with the extracted M' values of these grain boundaries, it was concluded that the growth occurring in this sample was abnormal in nature. In this chapter, I intend to establish a control experiment in which normal grain growth is investigated. With these results, the abnormal growth mechanisms observed in the AlMg specimen can better be identified and understood.

In an earlier study [119], a previous doctoral student in the Krill group found that, at high volume fractions of the coarsening phase, coarsening in semisolid Al-5 wt% Cu (referred to as AlCu) resembled normal grain growth. For this reason, this AlCu alloy was chosen as a specimen for the control experiment. From reconstructed time-resolved 3D microstructures, I show that the coarsening in AlCu differs from that in AlMg at both the grain and grain boundary levels. Using the reverse engineering method, I extract boundary M' values from the 4D mappings, and, at the end of this chapter, I discuss the dependencies of M' on boundary misorientation and inclination.

7.1 Sample preparation and 4D data acquisition

All measurements were performed on cylindrical specimens of Al-5 wt% Cu, cut to a diameter of 1.4 mm by spark erosion from a plate that had been cold-rolled to a total thickness reduction of 50% and then homogenized at 500°C for 24 h in air. A pre-annealing at 600°C for 10 min was conducted on the samples. At this temperature, the alloy consists of Al-rich solid particles and a surrounding liquid matrix. Heating into the semisolid state is reportedly capable of weakening the texture that arises from the

rolling process [192]. Upon cooling, the liquid phase crystallizes into a mixture of Al and θ phase, the latter of which contains a significant concentration of Cu. Owing to the difference in x-ray absorption of the two phases, it is possible to distinguish them by computed tomography (CT).

3D reconstructions of the sample microstructure were captured using both CT and 3DXRD microscopy at the Japanese synchrotron radiation facility SPring-8. For CT scans, the incident box beam had a size of 800 μm in height and 1600 μm in width. With the overlap between layers set to 50 μm, a total height of 3050 μm was measured after four layers of scans. The spatial resolution for the CT scans was 0.75 μm. Regarding the 3DXRD measurements, the settings for the incident beam and the detector parameters were identical to those described in Sec. 6.1.

We performed our investigations of coarsening in AlCu at a temperature slightly above the single-phase region (575°C), where a small amount of liquid wets the boundaries of the solid aluminum grains. According to the Al-Cu phase diagram [211], the volume fraction of the solid phase (V_V) is calculated to be 0.98. The advantage of two-phase coarsening is the potential homogenization of boundary properties by the thin liquid layer, through which atoms can quickly diffuse to equalize variations in boundary energy or mobility. In total, the sample was annealed six times at this temperature, with each annealing interval set to 10 min.

7.2 Microstructural evolution at the grain level

The recorded 3DXRD diffraction patterns were segmented and fed into appropriate reconstruction programs. The reconstructed grain volumes and associated crystallographic orientations are shown in Fig. 7.1 for different annealing steps. The corresponding number of grains is calculated and plotted against time in the same figure. After 60 min of annealing, the grain number had dropped from 937 to 271.

An example of a cross section that is reconstructed from a CT scan is shown in Fig. 7.2. After cooling from the annealing temperature, the liquid surroundings solidify to a mixture of the Al α phase and the θ phase, which has a higher x-ray absorption compared to the solid α phase grains. However, the volume fraction of the liquid phase is low, as confirmed by the small thickness of the θ phase between the grains in the micrograph. In some places, the θ phase is ambiguous or even undetectable with the current CT setup.

In Sec. 2.3, we discussed the coarsening mechanism in multiphase systems, namely Oswald ripening. Instead of directly migrating from one grain to another as in grain

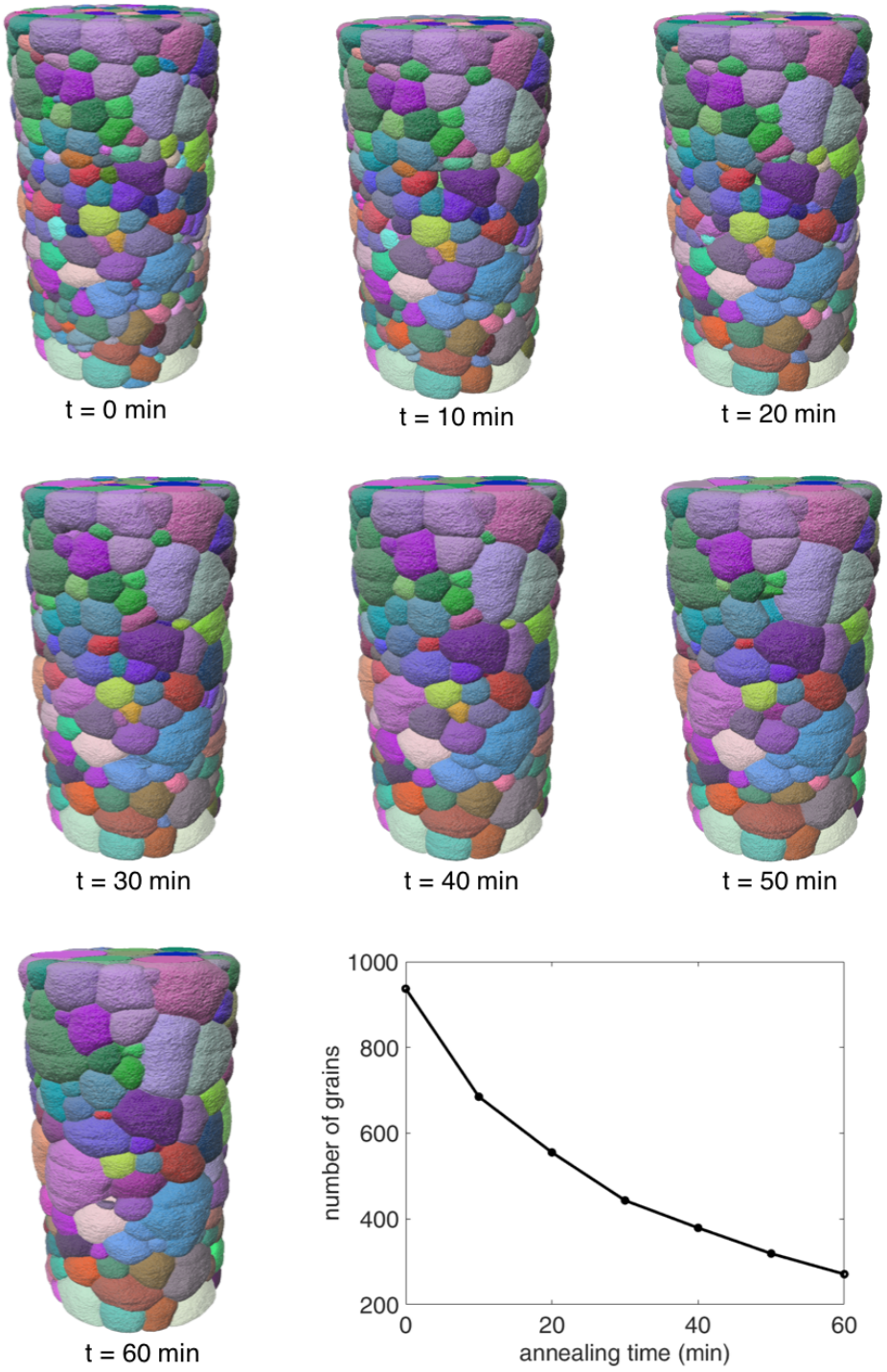

FIGURE 7.1: 3D coarsening in the AlCu specimen, visualized through 3DXRD reconstructions. Colors denote the Rodrigues vector representation of grain orientation. At lower right, the number of grains in each mapping is plotted against the cumulative annealing time.

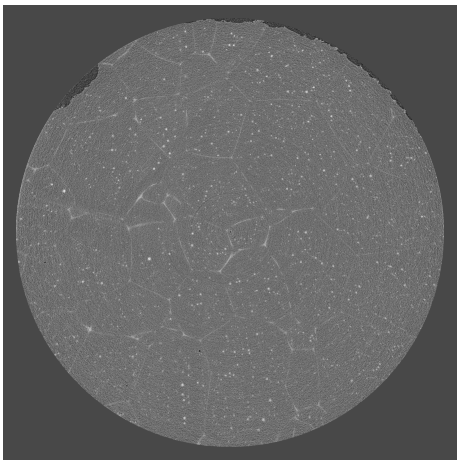

FIGURE 7.2: Cross section of a CT reconstruction of the AlCu specimen at $t = 0$. At the annealing temperature of 575°C, the volume fraction of the liquid phase (light gray color) is only 2%.

growth, the atoms from highly-curved grains must first diffuse into and through the matrix phase during Ostwald ripening. Despite this difference in the transport of atoms, at very high volume fractions of the coarsening phase, Ostwald ripening exhibits significant similarities to grain growth, as noted in the literature [122, 126].

Here, we first consider the grain size distribution (GSD) of the sample. Estimated from a kernel density function, the GSD for steady-state growth in AlCu is plotted in Fig. 7.3. The distribution is compared to the prediction of LSW theory, for which a vanishing volume fraction of the coarsening phase is assumed. The GSD in AlCu is much broader and shows a considerably lower maximum. In many regards, the AlCu GSD more closely resembles the distribution predicted by Hillert's mean-field grain growth model [103], plotted as the dashed line in Fig. 7.3. This result is consistent with findings reported in Ref. [122].

The similarity in high-V_V shape of the GSD between grain growth and Ostwald ripening is supported by our computer simulations. I used a phase field model to simulate these two different kinds of coarsening in the AlCu sample. For both simulations, the initial input was the 3DXRD reconstruction of AlCu at $t = 0$. In this 3D mapping, voxels in the proximity of grain boundaries are assigned as liquid to mimic the 2 vol% of liquid phase at the experimental annealing temperature. Grain growth was simulated using constant boundary energy and mobility, following the implementations described in Sec. 3.2. The Ostwald ripening simulation was performed by Nan Wang at Penn State University. For implementation details, readers are referred to Sec. 3.5.

Both simulations were run long enough so that the remaining number of grains lay below the total at the end of the experiment. In order to match the time scale of the simulation of that of experiment, I considered both the number of grains and individual

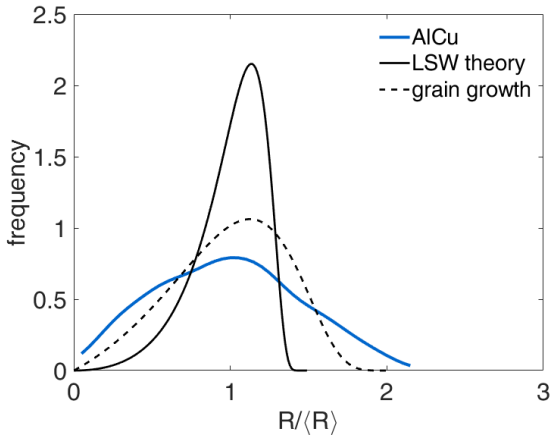

FIGURE 7.3: Grain size distribution in the AlCu specimen as calculated from the steady-state growth region (total of 6 timesteps, $t = 0$ is excluded). The result is compared to the distributions predicted by LSW theory and the mean-field grain growth model.

voxels. The 10-min annealing interval of the experiment was found to be equivalent to 3700 iterations for the grain growth simulation and 4 simulation outputs for the Ostwald ripening simulation. After this rescaling, the number of grains in experiment, in the grain growth simulation and in the Ostwald ripening simulation are plotted against a common time axis in Fig. 7.4 (a). All three curves manifest similar trajectories.

Grain size distributions can be calculated at each annealing timestep for the three datasets. Averaged distributions computed for the steady-state growth regime for each case are compared in Fig. 7.4 (b). Both simulated GSDs show a striking resemblance to the experimental one. None of the three show a sharp peak and rapid drop in frequency with larger particle size, as predicted by LSW theory. On the other hand, a slightly closer similarity to the mean-field prediction is observed. Evidently, although two different phases were involved in the coarsening of the AlCu specimen, the microstructural evolution shows no obvious statistical difference compared to that of grain growth. For this reason, the recorded 4D dataset of AlCu ought to constitute a fair comparison to the grain growth observed in the AlMg specimen presented in Chap. 6.

In Fig. 7.5 (a), we examine the GSD at individual timesteps during the annealing of AlCu. If the GSD at $t = 0$ is excluded, the remaining GSDs are quite similar, which is indicative of steady-state growth. Such time-invariance is characteristic of normal grain growth, but it was not observed in the AlMg specimen (Fig. 6.3). Moreover, a linear relation is found to hold between the square of the mean grain radius and the annealing time (Fig. 7.5 (b)), which is also typical of normal grain growth.

The same speculation can be made based on the evolution of 2D microstructures presented in Fig. 7.6. We find no evidence that certain grains grow much faster than the

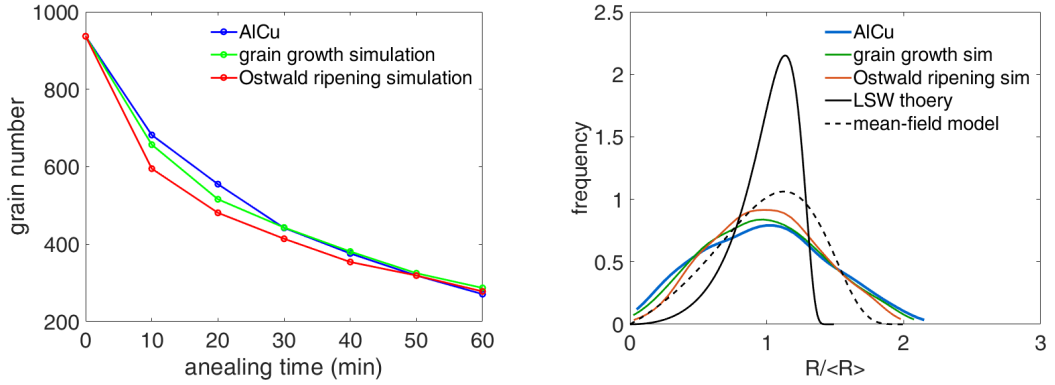

(a) (b)

FIGURE 7.4: (a) Number of grains in the AlCu experiment and in the grain growth and Ostwald ripening simulations after rescaling the simulation time. The grain size distributions for the three cases are plotted in (b) and compared to curves of LSW theory and the mean-field grain growth model.

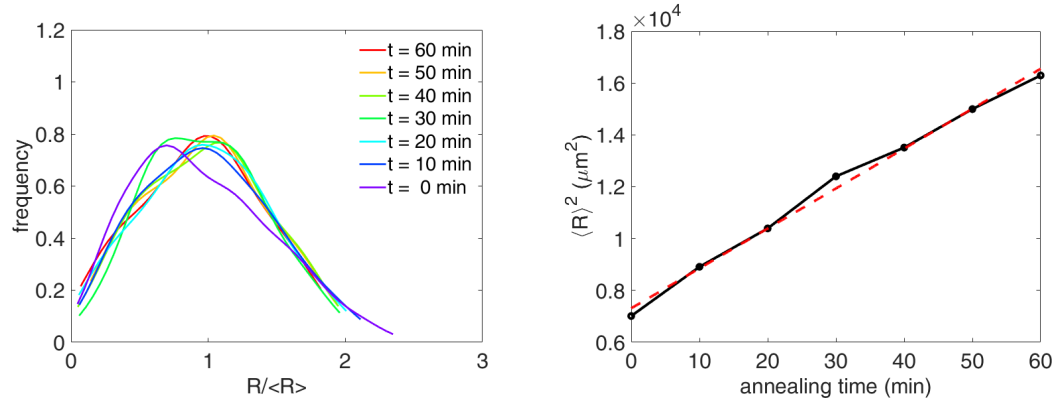

(a) (b)

FIGURE 7.5: (a) Grain size distributions at different timesteps for the AlCu specimen. (b) Square of the mean grain radius plotted against annealing time in AlCu. The dashed red line is a least-squares fit of a linear function to the data points.

rest. We can follow the corresponding grain size trajectories plotted in Fig. 7.7 (a) and see that most grains that were larger than R_c grew, while grains that were smaller than R_c shrunk during annealing. From the grain size trajectories, the growth rate dR/dt can be calculated for the intermediate data points of the trajectories using a central difference approach. As demonstrated by Eq. 6.2, the scaled growth rate $R \cdot dR/dt$ of a grain of size R is expected to depend linearly on $R/\langle R \rangle$. We investigate such a relationship in AlCu by constructing the scatter plot of Fig. 7.7 (b). Most of the data points lie in quadrants I and III of the plot and are concentrated around the dashed red line, which is the least-squares fit of a straight line to the data points. This regression line intersects $R \cdot dR/dt = 0$ at $R/\langle R \rangle = 1.05$, which is close to the value of 9/8 predicted by the Hillert grain growth model.

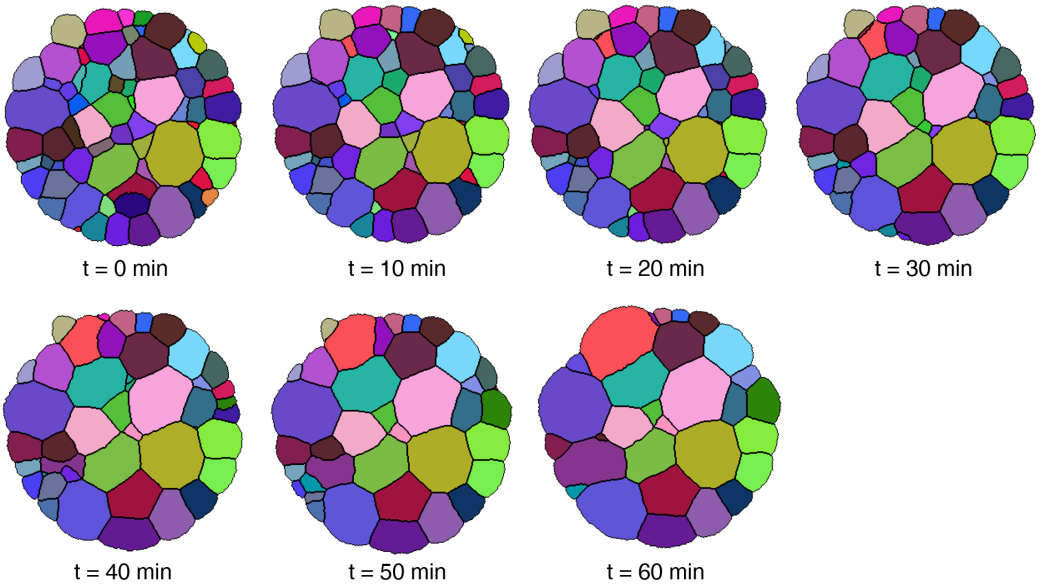

FIGURE 7.6: Microstructural evolution in the AlCu specimen as seen in an xy cross-section ($z = 200$). Grain boundaries have been marked by black lines in these images.

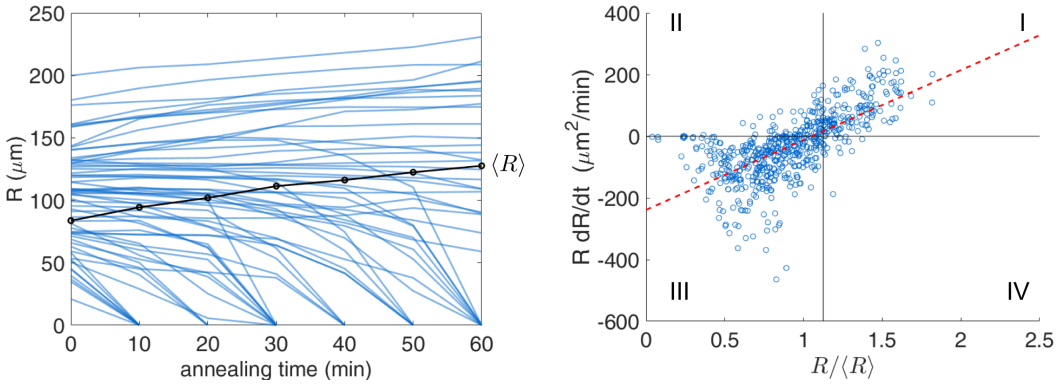

(a) (b)

FIGURE 7.7: (a) Grain size trajectories of the grains that appear in the cross sections of Fig. 7.6. The mean grain radius of all grains in the sample is shown by the black dots. (b) The scaled growth rate $R \cdot dR/dt$ plotted against the normalized grain radius $R/\langle R\rangle$. The dashed red line indicates a linear fit to the data points.

In order to compare the data points of Fig. 7.7 (b) to their counterparts in AlMg, a normalization is required, since coarsening of the two samples took place at rather different overall rates. The normalized $R{\cdot}dR/dt$ is defined to be the ratio of an individual grain's $R \cdot dR/dt$ to the global growth rate, $\langle R\rangle d\langle R\rangle/dt$, extracted from the slope of the linear regression line. For both samples, the normalized $R \cdot dR/dt$ plots are compared in Fig. 7.8. It can be seen that the data points of AlCu are more concentrated around the regression line, whereas the data points of the AlMg sample display much more scatter.

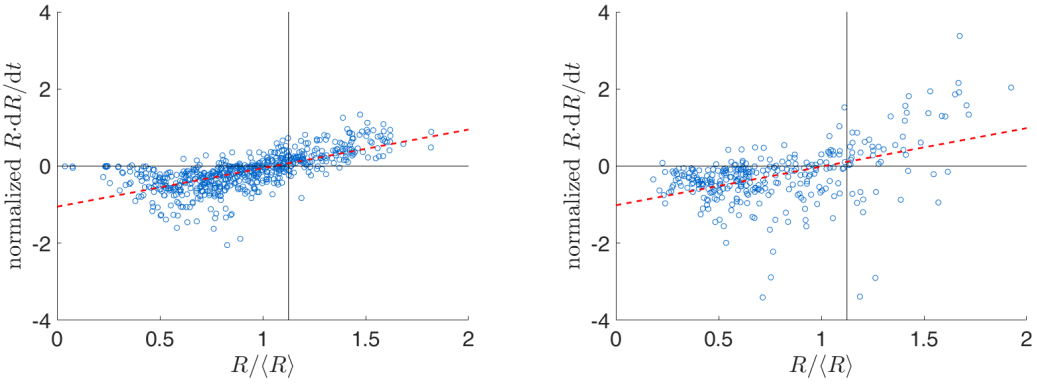

FIGURE 7.8: Normalized $R \cdot dR/dt$ plotted against $R/\langle R\rangle$ in (a) AlCu and (b) AlMg.

The residual standard error is used to quantify this scatter.[1] The residual standard error is calculated to be 0.3506 for AlCu and 0.6648 for AlMg. From such a comparison, it is concluded that the growth of individual grains in AlCu is better described by the mean-field model of grain growth than is the coarsening of individual grains in AlMg. This is consistent with the global statistics for AlCu.

7.3 Microstructural evolution at the grain boundary level

In this section, we focus on grain boundary characteristics and how these change during annealing of the AlCu specimen. In Fig. 7.9 (a), the same cross section shown in Fig. 7.6 is presented again for $t = 0$. This time, grain boundaries are colored to indicate their misorientation angle. In the 2D cross section, many fewer blue boundaries are seen compared to the results of AlMg (cf. Fig. 6.6 (a)). Misorientation distributions of all boundaries in the AlCu sample are plotted in Fig. 7.9 (b) for the different annealing timesteps. These distributions do not change significantly over time, and they closely resemble the Mackenzie distribution derived from a random assembly, although a weak peak is seen around 10° for all annealing steps. The grain boundaries in the AlCu specimen are thus more-or-less randomly distributed in misorientation space.

Considering the large fraction of high-angle grain boundaries (HAGBs)s, it is worthwhile to examine the population of CSL boundaries in the sample. Figure 7.10 plots the relative frequency in multiples of a random distribution (MRD) for the various CSL boundaries of Σ values up to 23. For clarity, only the results at $t = 0$ and $t = 60$ min are shown. Note that at $t = 0$, two types of Σ17 have the same MRD value, leading to

[1] Residual standard error is defined as $\sqrt{RSS/(n-2)}$, where RSS is the residual sum of squares of the linear fit, and n is the number of data points.

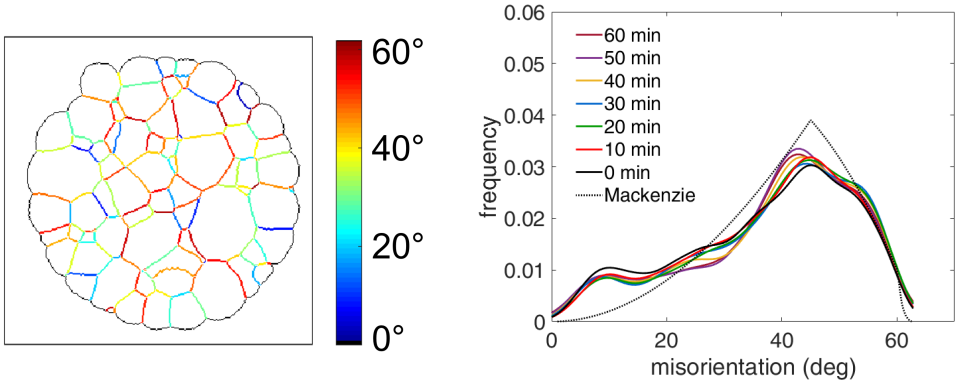

(a) (b)

FIGURE 7.9: (a) Grain boundaries in a cross section ($z = 200$) of the reconstructed AlCu sample at $t = 0$. Colors indicate the boundary misorientations. (b) Misorientation distributions for all GBs in AlCu at different timesteps. The distributions are compared to the Mackenzie distribution (dotted black line).

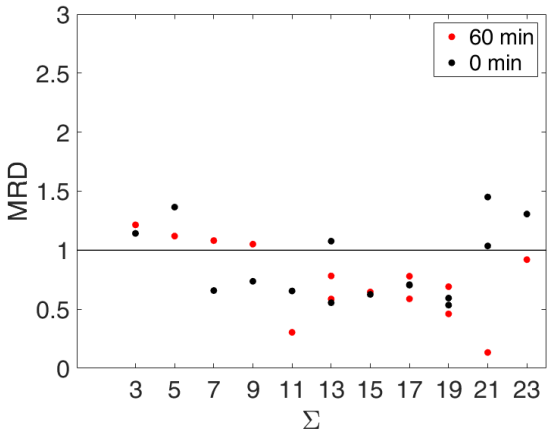

FIGURE 7.10: Relative frequency (in multiples of a random distribution, MRD) of CSL boundaries in the AlCu specimen at $t = 0$ and $t = 60$ min.

a single dot on the plot. The same applies to Σ21 at $t = 60$ min. On the plot, the MRD values for most of the data points are smaller than one. Only a few points, *e.g.*, Σ3, Σ5, Σ7 and Σ9, have an MRD slightly larger than one. We also calculated the actual occurrence frequency of all CSL boundaries in the sample. The results of 8.92% at $t = 0$ and 8.93% at $t = 60$ min are somewhat lower than the 9.75% expected for a random assembly.

Inclination distributions were also calculated for the boundaries of the AlCu sample. The results at $t = 0$ and $t = 60$ min are plotted in the [001] pole figures presented in Fig. 7.11. The color bar is set to have the same range as the plot in Fig. 6.8, so that the inclination distributions for AlCu and AlMg can be directly compared. As shown in Fig. 7.11, AlCu exhibits no strong peak at either the beginning or end of the measured coarsening, considering the fact that there are no reddish colors in the pole figures.

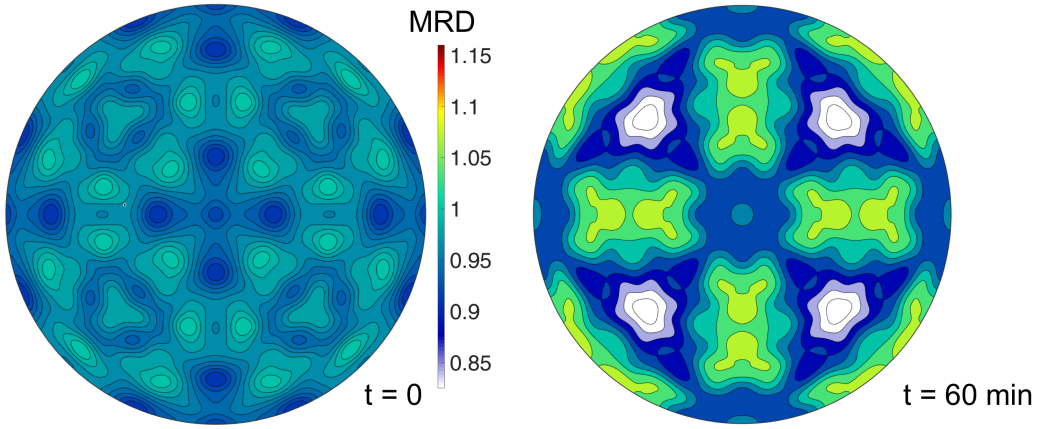

(a) (b)

FIGURE 7.11: Grain boundary inclination distribution in the AlCu specimen at $t = 0$ and $t = 60$ min. The color bar is set to the same range as in Fig. 6.8.

Compared to the AlMg sample, the boundary inclinations in the AlCu specimen are more homogeneously distributed, *i.e.,* the grain boundary normals manifest no predominant direction.

7.4 Reverse engineering the grain boundary M'

Using the reverse engineering method, I was able to extract the grain boundary M' from sequential 3D microstructural mappings of the AlCu specimen. The resulting M' values for all six annealing intervals are plotted in the histogram of Fig. 7.12 (a). The median value is 345.69 μm^2/min. In Fig. 7.12 (b), the reduced grain boundary mobility is further analyzed and indexed to the boundary misorientation. Inside each bin of the bar chart, the median was used to set the bin height. In the AlCu specimen, M' increases with greater misorientation for LAGBs. The angular limit θ_m for LAGBs is around 20°. This value is close to the commonly used threshold angle found in the literature [3, 61, 64–66]. Additionally, for boundaries of misorientation larger than θ_m, the reduced mobility remains at a more-or-less constant value. Although the grain boundary energy is only one of the two factors contained in M', the dependency of energy on misorientation described by Eq. 2.9 is qualitatively consistent with the trend seen in Fig. 7.12 (b).

Figure 7.13 displays the boundary M' with respect to the GB inclination in a [001] pole figure. In order to compare with the inclination dependency of the AlMg specimen, the color bar in Fig. 7.13 takes the same range as in Fig. 6.12. Compared to the valleys at $\langle 111 \rangle$ poles present in AlMg, AlCu shows a rather homogeneous dependency of M' on inclination. In AlMg, we also found an inverse relationship between the boundary

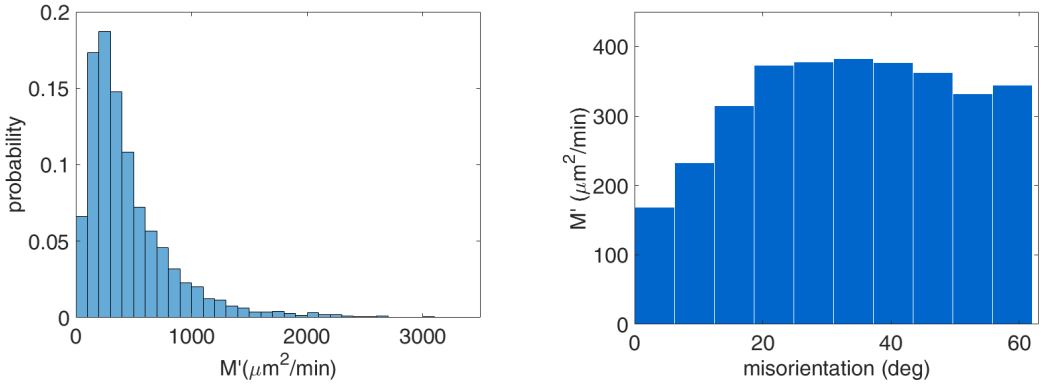

(a) (b)

FIGURE 7.12: (a) Grain boundary reduced mobility M' estimated by the reverse engineering method for the six annealing intervals of the AlCu specimen. (b) Dependency of the median M' value on GB misorientation in AlCu.

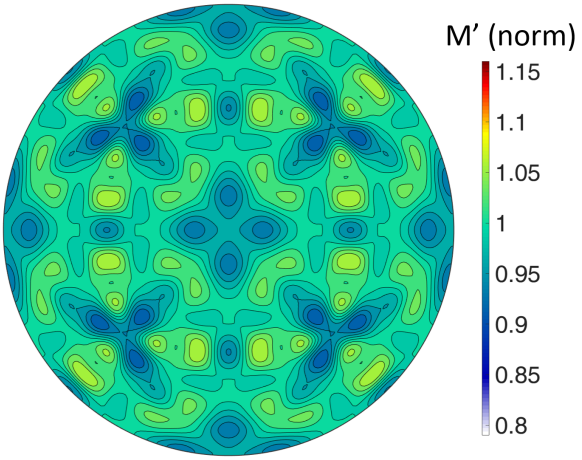

FIGURE 7.13: Normalized M' in AlCu plotted against grain boundary inclination in a [001] pole figure. The color bar has the same range as in Fig. 6.12.

M' and the boundary population, whereas such a relationship is not apparent in AlCu because of the homogeneity exhibited in both the inclination population distribution and the dependency of M' on inclination.

At the end of this section, we examine the spread of the data underlying the bar chart of Fig. 7.12 (b), which displays only the median value for each bin. The corresponding violin and box plots are shown in Fig. 7.14. The stretched shape of the violins in each bin indicates that grain boundaries of a similar misorientation in the AlCu specimen vary in their M' values to a great extent. Nevertheless, compared to the results of AlMg, the box plot in Fig. 7.14 has shorter distances between the upper and lower hinges. I used the 25th, 50th and 75th percentiles of the data to calculate the relative data spread in each bin: the average relative data spread in AlCu ranges from -40.6% to 71.3%, which is smaller than the values determined for AlMg (from -52.4% to 102.3%).

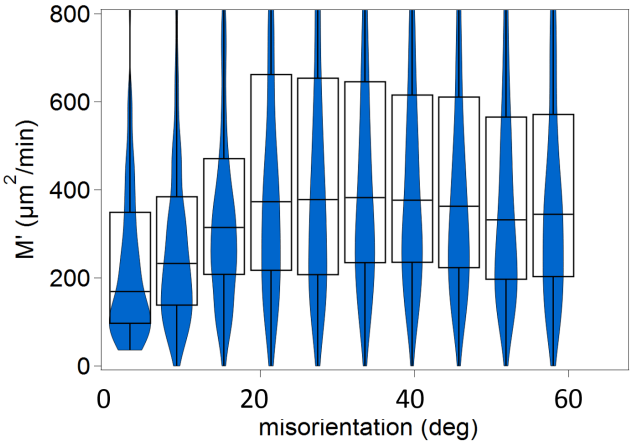

FIGURE 7.14: Spread of M' data points underlying the bar chart of Fig. 7.12 (b), represented by superposed violin (blue) and box (black) plots.

7.5 Final remarks

The goal of the experimental work presented in this chapter was to collect time-resolved 3D data that displayed normal grain growth. Such a dataset was achieved by taking 3D snapshots of the coarsening in an Al-5 wt% Cu specimen using 3DXRD microscopy. The annealing temperature (575°) was set slightly above that of the single-phase region. From the reconstruction of CT scans, the microstructure (Fig. 7.2) manifests solid grains surrounded by a thin layer of liquid (2% in volume fraction). Although the coarsening mechanism is Ostwald ripening, the resulting grain size distribution differs greatly from the theoretical model for Ostwald ripening derived for a vanishing fraction of the coarsening phase. Comparing phase field simulation results for a model that assumes Ostwald ripening to those for normal grain growth, we see that the thin liquid layer has only a slight effect on the predicted outcome when starting from the same initial microstructure. More importantly, however, this liquid layer is found to homogenize the grain boundary properties in the AlCu sample, a finding that is backed by analysis at both the grain and grain boundary levels.

At the grain level, the square of the mean grain radius is linearly proportional to the annealing time. Moreover, the grain size distributions take on time-invariant shapes. Neither of these features were observed during grain growth in the AlMg specimen. The linearity is also more pronounced between the scaled instantaneous growth rate of individual grains and the normalized grain radius. That is to say, the growth of individual grains in AlCu is closer to the mean-field prediction. This indicates that the main prerequisite for normal grain growth could be fulfilled: the grain boundary energy and mobility are isotropic (or nearly so) in the two-phase region of AlCu. At the grain boundary level, we found no predominant types of CSL boundaries in the sample. The

distributions of boundary misorientation and inclination are both homogeneous: indeed, the misorientation distribution is close to the Mackenzie distribution for a random assembly, and the inclination distribution shows very weak peaks for {111} planes when compared to AlMg.

The reduced mobility M' of individual boundaries was determined by the reverse engineering method. When indexed to the boundary misorientation, the reduced mobility was found to increase with larger misorientation until reaching a plateau for HAGBs. Moreover, the spread in M' was less than in AlMg. Pole figures of boundary inclination showed a weak dependency on this parameter. All of these observations support the original supposition that a thin layer of liquid can equalize the boundary energy and mobility. In general, the boundary migration exhibited by the AlCu specimen is much steadier and more uniform than in AlMg.

Chapter 8

Discussion and Conclusions

In the previous two chapters, I presented the coarsening that took place in two specimens measured experimentally. Through growth statistics measured at the grain and grain boundary (GB) levels, grain growth in Al-1 wt% Mg is revealed to be abnormal, whereas a rather normal type of growth is observed in the Al-5 wt% Cu specimen. These two different growth modes can be related to the dependency of the reduced GB mobility on boundary misorientation and inclination, which was obtained from the reverse engineering analysis of boundary migration. Armed with this knowledge, in this chapter I answer the scientific questions posed in *Introduction*.

8.1 Validity of the reverse engineering method

Grain boundaries are demonstrated to be an important component in polycrystalline materials [3], as they play an essential role in governing the mechanical and other functional properties of the materials. This significance of grain boundaries is exploited, for example, in the field of "grain boundary engineering" [40–44]. In particular, the boundary mobility and energy are critical for understanding the phenomenon of coarsening in polycrystalline materials.

In Sections 2.1.3 and 2.1.4, the conventional approach toward obtaining values for these two quantities is discussed. The bicrystal technique is demonstrated to be the most successful method for measuring the reduced mobility of a grain boundary under capillary/external driving forces [10–13]. Nevertheless, the main disadvantage of the bicrystal approach lies in its experimental complexity. On the one hand, the migration of a bicrystal boundary is sensitive to the bicrystal quality. On the other hand, fabricating enough samples to cover the entire five-parameter boundary space is practically

impossible. Hence, the urgency of extracting boundary reduced mobilities directly from polycrystalline materials, as addressed in the first question of Chap. 1:

1. Is it possible to retrieve the reduced GB mobility from measurements of the coarsening of grains in a polycrystalline material?

Being able to record the migration of individual grain boundaries in a polycrystalline material is a necessity to answer the question. In order to capture the 3D microstructure of a material in a time-resolved manner, 3DXRD microscopy was utilized in our investigations. Exploiting the interference of x-rays scattering from a crystal lattice, 3DXRD measurements are capable of distinguishing between grains of different crystallographic orientation in a single-phase material. After the indexing and evaluation of the various diffraction peaks, the method is able to reconstruct grain volumes and determine their lattice orientations. In such datasets, grain boundaries are implicitly defined by the grain volumes. By remapping the microstructure after each interval of heat treatment, we are thereby able to capture the migration of thousands of grain boundaries in a given sample.

In order to retrieve the reduced GB mobility for such a dataset, we proposed a reverse engineering type of analysis in Chap. 5. Two quantities—the boundary integral mean curvature $\langle H \rangle$ and the boundary migration velocity v—must be estimated with great care in order to obtain accurate values for the reduced mobility M'. For details of these procedures, readers are referred to the respective sections in Chap. 5. It is worth mentioning that the method is limited to certain types of boundaries in the dataset. This can be easily understood from a static/dynamic point of view. At a given timestep, a boundary being analyzed should not be too small (in area) or too flat, as both of these characteristics lead to huge uncertainties in the estimated boundary curvature. When considering the migration of a boundary between two sequential timesteps, one should avoid cases in which the boundary moves a short distance or disappears. In both of these cases, the estimated boundary migration distance has a large relative uncertainty. Therefore, thresholds have to be imposed in the reverse engineering method on the quantities $\langle H \rangle$, GB area and swept volume so that sufficiently precise values for M' are obtained (Secs. 5.1 and 5.2).

In addition, through computer simulations we were able to vary both the spatial and temporal resolution of a 4D dataset in order to investigate their influence on the reverse engineering method. Readers are referred to Sec. 5.4 for details. It is concluded that the annealing duration between two 3D mappings should be moderate—on the one hand, significant boundary migration should be recorded, but, on the other hand, individual GB migrations must be trackable, avoiding situations in which a GB changes greatly in size or even vanishes. High spatial resolution is an important factor for successful

data collection, as it affects not only the estimation of boundary migration but also the boundary curvature. Nevertheless, in the 3DXRD setup, the spatial resolution is limited by the resolution of the near-field detector. Therefore, the proper relative spatial resolution should be established by preparing experimental specimens with a sufficiently large average grain size.

The validity of the reverse engineering method was tested on computer simulations of grain growth that were carried out with known values for the boundary M'. Two types of simulations were employed: in one case, all boundaries were set to have the same M' (referred to as the NGG simulation); in another case, M' was set to depend on boundary misorientation (referred to as the AGG simulation). For both simulations, we found that the reverse-engineered data for M' were clustered tightly around the value(s) input to the simulation. In the NGG case, the median of the M' values had a relative error of only 2.5% with respect to the simulation input (Fig. 5.8). In the AGG case, the median representation of bin height in the bar chart of Fig. 5.11 was determined to be good enough to retrieve the orientation dependency that was assumed during the simulation.

An equally important aspect of the results was the spread in estimated M' values, which was considered to be a measure for the intrinsic error of the reverse engineering method. In this study, such spreads were quantified by the 25th and 75th percentiles of the data. We replot the results of the NGG simulation in Fig. 8.1, where the boundary M' is normalized by the simulation input (*i.e.*, the true value for M'). The relative spread about the median is marked by the dashed red lines, ranging from -16.0% to 16.3%. For the AGG simulation, the spread in data is hidden in the bars of the bar chart shown in Fig. 5.11. This is remedied in Fig. 8.2, in which violin and box plots depict the spreads of M' values in each bin. From the upper and lower hinges of the boxes, we can estimate the global relative spread (averaged over all the bins) to extend from -16.9% to 22.8%. This range is similar in size to the spread in the NGG simulation. Based on these results, the reverse engineering method proves to be capable of retrieving the boundary reduced mobility from the coarsening of an ensemble of grains, even though certain errors and uncertainties remain in the estimated values for M'.

Using the reverse engineering method, we successfully extracted the reduced mobility of boundaries from the GB migration recorded by 3DXRD microscopy in two Al-based specimens. A clear dependency of boundary M' on misorientation was observed, as plotted in Fig. 8.3. Direct comparison of the datasets in Fig. 8.3 is made possible by using normalized values for M', as the two samples were annealed at different temperatures. In this case, the normalization factors were computed from the respective medians of the absolute M' values found by reverse engineering. In both samples, M' was observed

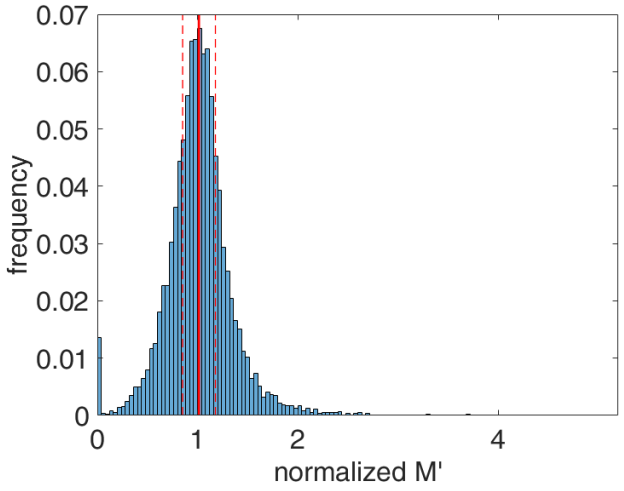

FIGURE 8.1: Histogram of normalized M' values for grain boundaries in the NGG simulation. The dashed red lines mark the 25th and 75th percentiles of the data, and the solid red line denotes the median.

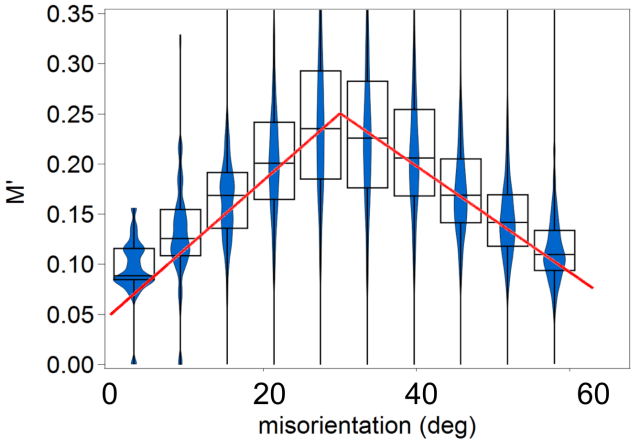

FIGURE 8.2: Violin and box-plot representations of the spread in M' values for the AGG simulation. The solid red line indicates the simulation input M'. (In Fig. 5.11 the same data are plotted as a bar chart showing only the median.)

to increase with misorientation for low-angle grain boundaries. This result is physically understandable in terms of the Read-Shockley model for the boundary energy γ, in which γ is predicted to increase with the misorientation between two neighboring grains.

8.2 Validity of the curvature-driven mechanism of boundary migration

According to Burke and Turnbull's description of boundary migration [6], the driving pressure P is a function of boundary energy and curvature (Eq. 2.15). Because the boundary energy and mobility are strictly positive terms in Eq. 2.16, the boundary

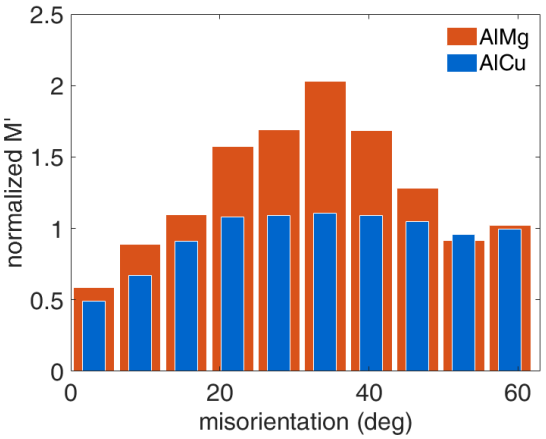

FIGURE 8.3: Dependency of the median boundary M' on the GB misorientation in AlMg and AlCu. To allow a direct comparison of these datasets, the absolute M' values were normalized by the respective median value for each sample.

velocity ought to have the same sign as the curvature: *i.e.,* a boundary migrates toward its center of curvature. Nevertheless, other forces may affect the speed and direction of boundary migration in polycrystalline materials. For example, second-phase particles are demonstrated to be capable of exerting a pinning pressure on grain boundaries [3, 31]. As described in Sec. 2.2.1, the driving force from second-phase particles is primarily determined by the particle size, volume fraction and distribution. Since the particles have a strong influence on the growth kinetics, some boundaries in the vicinity of particles may possibly migrate in a direction that is not aligned with the direction of the center of curvature. This kind of behavior can be detected and studied using the reverse engineering method, which brings us to the second question raised in Chap. 1:

2. Is GB curvature the primary driving mechanism for boundary migration in polycrystalline materials?

As described by Eq. 5.1, if curvature-driven migration takes place, the boundary velocity and the boundary integral mean curvature ought to share the same sign, which yields a positive value for M'. By searching for and examining only boundaries with negative M', we are able to determine whether mechanisms besides curvature play an important role in the boundary migration observed in various materials.

Before taking a closer look at the experimental datasets, we first examined the boundaries in the NGG and AGG simulations. The total number of grain boundaries analyzed by the reverse engineering method and the percentage of boundaries that were found to have negative M' values are listed in Table 8.1. With more than seven thousand boundaries analyzed, only 2.5% of the boundaries in the NGG simulation manifest negative values for M'. In a phase field simulation of grain growth, the grain boundaries migrate according to the minimization of the energy described in Eq. 3.1. Since there is

	number of GBs analyzed	percentage of GBs with negative M'
NGG simulation (isotropic M')	7520	2.5%
AGG simulation (anisotropic M')	8964	2.9%
Al-1 wt% Mg	4404	24.1%
Al-5 wt% Cu	6375	12.0%

TABLE 8.1: The total number of grain boundaries (GBs) analyzed by the reverse engineering method and the percentage having a negative value for M'. The first two rows come from computer simulations, whereas the remaining rows correspond to experimental datasets.

no external driving force involved, the boundaries ought to migrate solely toward their centers of curvature. This is also true for the AGG simulation with anisotropic M'. Only 2.9% of the total boundaries show negative M', as the capillary force remains the sole driving force in the simulation. Considering that M' should be strictly positive in both simulations, we view the 3% of the total boundaries that exhibit negative M' to be a measure for the intrinsic error associated with the reverse engineering method itself.

The third and fourth rows of Table 8.1 show the results for the two experimental datasets. The percentage of boundaries having negative M' takes on considerably larger values than in the simulations. This increase may result from several factors. First, the data quality has a large impact on the results. Specifically, the accuracy of an estimated boundary M' value is highly dependent on the accuracy in boundary position and tracked migration. In these regards, the simulation dataset should represent the ideal case. In an experimental dataset, the boundary positions are influenced by the reconstruction routine of the 3DXRD measurements. Additionally, the measured boundary migration distances are sensitive to the alignment of 3D mappings at different timesteps. In a computer simulation the situation is quite different: the spatial resolution can be adjusted more or less freely, and between different iterations no registration issues are encountered. However, data quality alone cannot explain the significant difference between the two experimental datasets, where around a quarter of the boundaries exhibit negative M' in AlMg, but only half as many in AlCu. This difference can be understood by considering the fact that rather different types of grain growth took place in the two specimens. As discussed in Chap. 6, coarsening in AlMg exhibits abnormal characteristics. Apparently, factors other than the capillary force facilitate the migration of some boundaries in AlMg in a quite different manner than in the isotropic growth model. From 3D mappings of the microstructure, we obtained evidence that some of the AlMg boundaries with negative M' manifested irregularity in morphology, even for boundaries of large area.

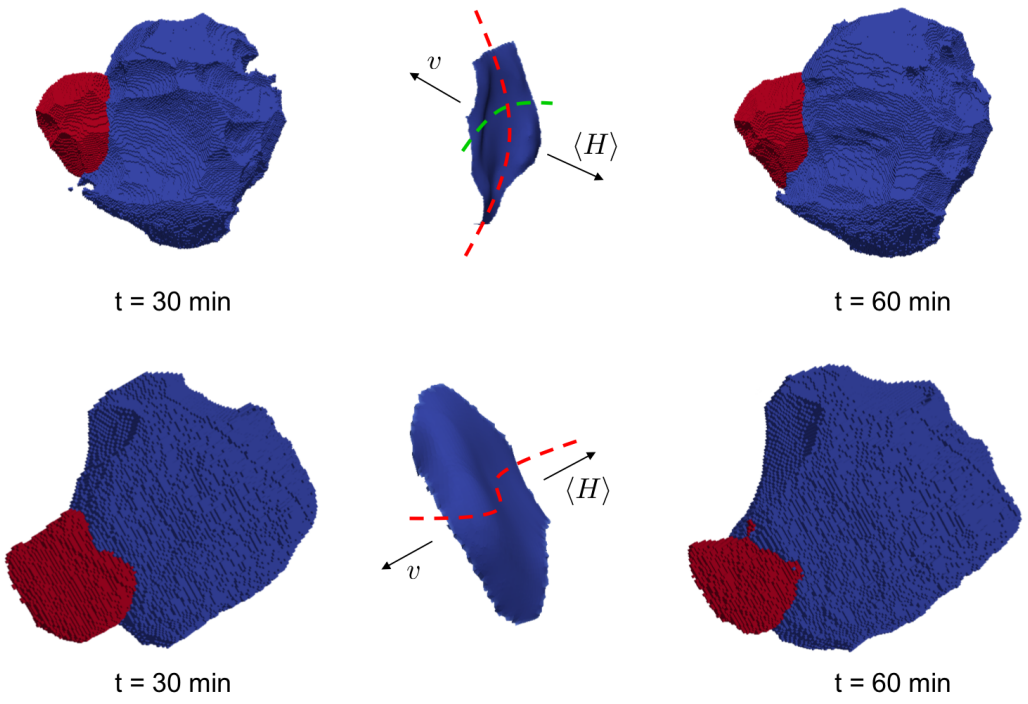

FIGURE 8.4: Examples of boundaries with negative M' in the AlMg specimen. Some boundaries are found to have irregular shapes: saddle shape (top row), wavy shape (bottom row). In both cases, the direction of local curvature varies along the boundary. The final calculated integral mean curvature $\langle H \rangle$ is opposite in sign to the observed boundary migration velocity v. Some important characteristics of these boundaries are listed in Table 8.2.

Figure 8.4 shows two examples of boundaries exhibiting negative M' values in the AlMg specimen. In the top row of images, we focus on the boundary between Grain #300 and Grain #357. The left and right figures show the grain morphology at $t = 30$ min and 60 min, respectively. Some important intermediate results that flow into the reverse engineering computation of M' are listed in Table 8.2. From the shape of the boundary at $t = 30$ min (middle column), it is found that the boundary has taken on a clear saddle shape: the two principal curvatures point in different directions. Therefore, the final sign of the integral mean curvature $\langle H \rangle$ of the boundary depends on the balance between patches of boundary area having positive *vs.* negative curvatures. For this boundary, the sign of $\langle H \rangle$ differs from the sign of the migration velocity v, leading to a negative value for M'.

In the bottom row of Fig. 8.4, a boundary in AlMg manifests a wavy shape. Indicated by the dashed red line superimposed on the boundary at $t = 30$ min, the sign of the mean curvature of individual boundary patches varies with location, which also leads to $\langle H \rangle$ having a different sign than that of the direction of boundary migration.

quantity	saddle shape (Fig. 8.4, top row)	wavy shape (Fig. 8.4, bottom row)
M' (μm^2/min)	-207.72	-119.47
$\langle H \rangle$ (μm^{-1})	-1.82×10^{-3}	-6.86×10^{-3}
V_{swept} (μm^3)	9.26×10^5	7.39×10^5
$A_{30\,\text{min}}$ (μm^2)	7.46×10^5	3.20×10^4
$A_{60\,\text{min}}$ (μm^2)	8.81×10^5	2.82×10^4

TABLE 8.2: The computed reduced mobility M', the integral mean curvature $\langle H \rangle$, the swept volume V_{swept}, and the areas $A_{30\,\text{min}}$ and $A_{60\,\text{min}}$ of the boundaries shown in Fig. 8.4.

From the discussions detailed above, I conclude that boundary curvature is the dominant driving force for boundary migration in the AlCu specimen, in which grain growth manifested all of the hallmarks of normal grain growth. In contrast, boundary migration in AlMg must be affected—at least in part—by factors other than curvature, as 24% of the boundaries migrated against the direction dictated by curvature. Moreover, these boundaries tended to exhibit rather irregular morphologies. These findings are consistent with the abnormality observed at both the grain and grain boundary levels in AlMg.

8.3 Dependency of boundary reduced mobility on macroscopic boundary properties

In the previous section, we examined the origin of negative M' values for individual boundaries according to the reverse engineering analysis. In this section, we consider the proper interpretation of positive values for M' and their relationship to macroscopic boundary properties (boundary misorientation and inclination). In so doing, we address the last question raised in the Introduction:

3. Is the reduced GB mobility determined uniquely by the macroscopic GB properties?

In Chaps. 6 and 7, we briefly discussed the dependency of M' on the boundary misorientation and inclination in AlMg and AlCu, respectively. In both cases, the dependency on boundary inclination was found to be weak, whereas clear trends were observed in the relationship between M' and misorientation. A comparison of the latter dependency already appears in Fig. 8.3. However, in both samples we found that boundaries of similar misorientation usually varied significantly in their M' values: within a given bin of misorientation angle, the violin plots of Fig. 8.5 encompass a wide range of M' values,

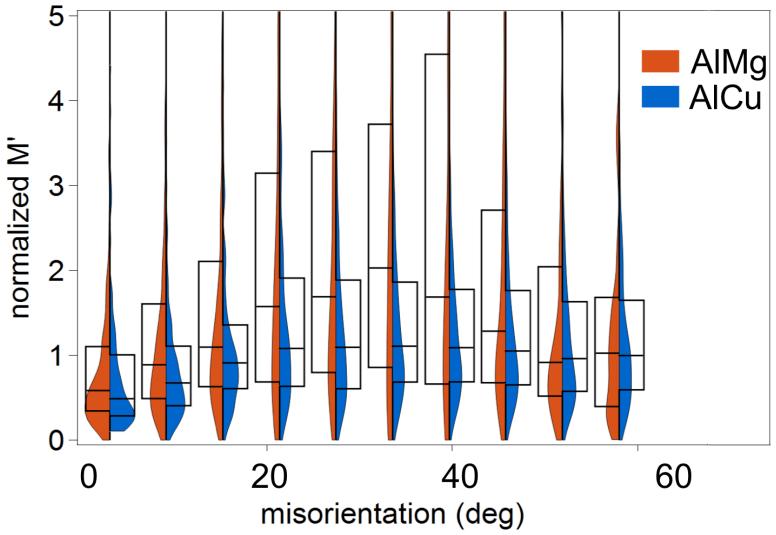

FIGURE 8.5: Comparison of the distribution in boundary M' values in AlMg and AlCu. The corresponding violin and box plots are drawn in split form with AlMg on the left and AlCu on the right. (The M' values were normalized as in Fig. 8.3.)

indicating that the boundary misorientation alone is insufficient to determine a precise value for the reduced mobility.

The box plots of Fig. 8.5 demonstrate that the spread of M' values is larger in AlMg than in AlCu. We recall the average relative spread calculated for these two samples: from -52.4% to 102.3% in AlMg and from -40.6% to 71.3% in AlCu. Both ranges are significantly greater than the spread computed for the NGG simulation (from -16.0% to 16.3%), which can be viewed as the intrinsic error of the reverse engineering method. Consequently, the larger spreads in the experimental datasets imply that other factors modified the measurement of reduced mobility for the GBs in the experimental specimens.

For the results presented in Fig. 8.5, the reverse engineering analysis combined the data from various annealing intervals—in other words, data from different time steps were included in the sample figure. In order to better understand the origin of the data spread, we decompose M' into a time-independent, intrinsic part of the reduced mobility, $M'_{\text{intrinsic}}$, and the change in M' over time, $\delta M'(t)$:

$$M' = M'_{\text{intrinsic}} + \delta M'(t). \tag{8.1}$$

These two components can be distinguished by plotting trajectories of the reduced mobility of individual GBs. In Fig. 8.6 (a), we show a schematic plot of M' values for a GB that appears in five sequential microstructural mappings, which leads to four data points in the plot. For a given trajectory, we estimate $M'_{\text{intrinsic}}$ by the data mean, and we quantify the fluctuation term $\delta M'(t)$ by the distance between M' and $M'_{\text{intrinsic}}$ at the

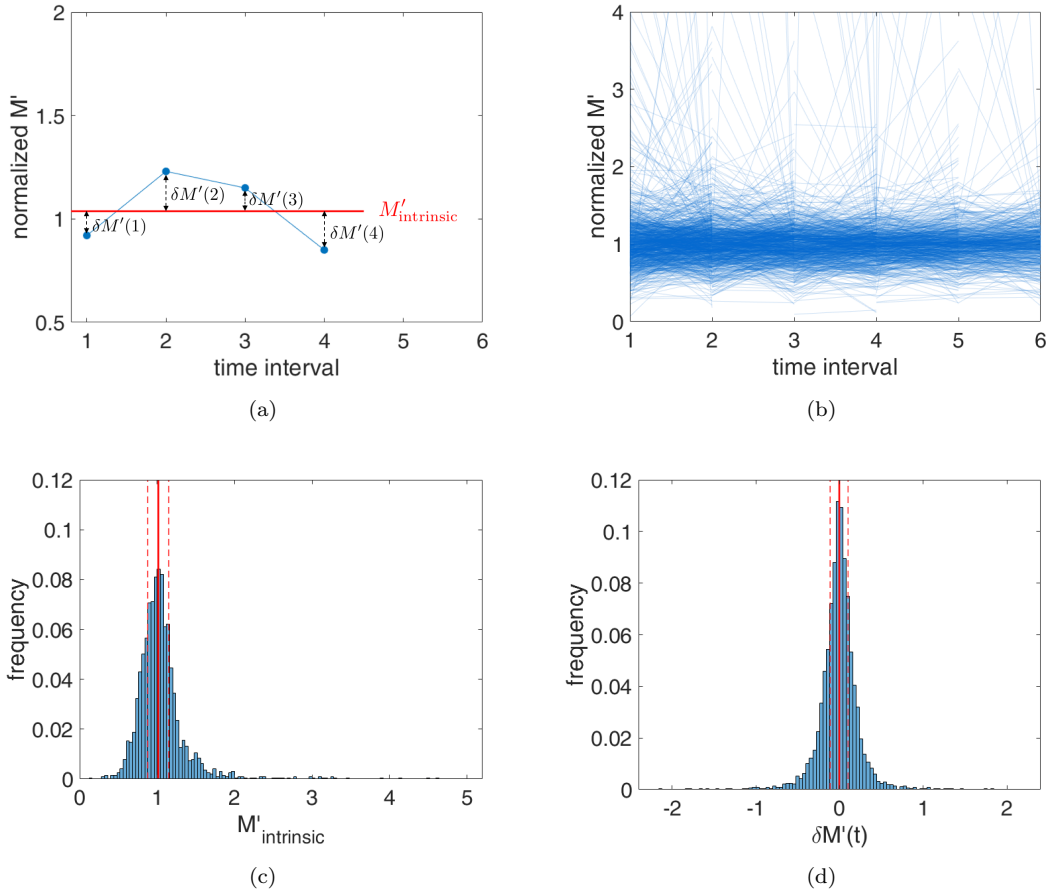

FIGURE 8.6: (a) Schematic illustration of the quantification of components $M'_{\text{intrinsic}}$ and $\delta M'(t)$ for the M' trajectory of a single GB. (b) Trajectories of normalized M' in the NGG simulation. The quantities $M'_{\text{intrinsic}}$ and $\delta M'(t)$ for the trajectories of (b) are plotted in the histograms of (c) and (d), respectively.

time t. Figure 8.6 (b) shows the M' trajectories for all boundaries in the NGG simulation. It is found that most trajectories are concentrated around a value of 1 (normalized M'). From these trajectories we calculate $M'_{\text{intrinsic}}$ values for each boundary and plot them in a histogram (Fig. 8.6). Using the same method to quantify the data spread as above, we calculate the relative spread in $M'_{\text{intrinsic}}$ to range from -13.4% to 13.2%. The trajectories in Fig. 8.6 (b) are also rather flat, since the boundaries in the NGG simulation should not change their M' value over time. Nevertheless, small fluctuations with time are found by the analysis. The quantity $\delta M'(t)$ for each GB is calculated and plotted in the histogram of Fig. 8.6 (d), and the spread of the $\delta M'(t)$ term extends from –0.11 to 0.10.

The same decomposition procedure was applied to both experimental datasets. In Figs. 8.7 (a) and (b), trajectories of normalized M' are plotted for GBs in AlMg and AlCu. Since both figures share the same vertical axis, it is apparent that the trajectories of GBs in AlMg are more scattered than the trajectories in AlCu, which are more densely

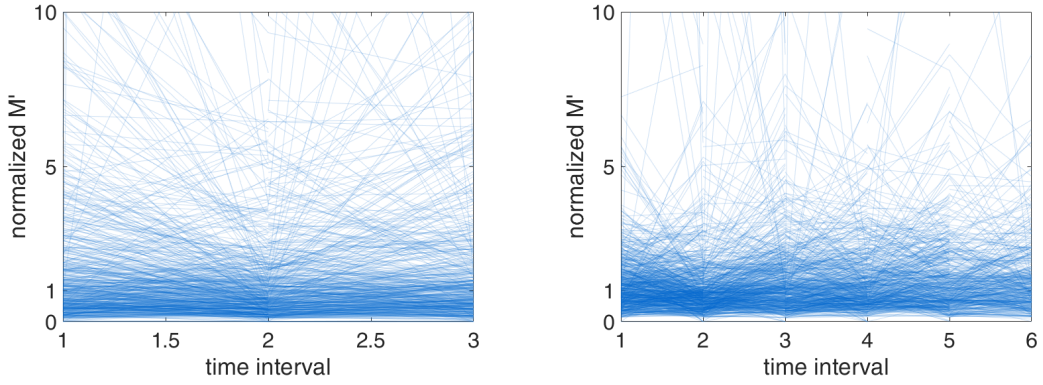

FIGURE 8.7: Trajectories of normalized reduced mobility plotted for GBs in (a) AlMg and (b) AlCu.

bunched around 1. After decomposition of M', the relative spreads arising from $M'_{\text{intrinsic}}$ and $\delta M'(t)$ are summarized in Table 8.3.

	spread in $M'_{\text{intrinsic}}$	spread in $\delta M'(t)$
NGG simulation	–13.4%, 13.2%	–0.11, 0.10
Al-1 wt% Mg	–48.6%, 115.0%	–0.34, 0.27
Al-5 wt% Cu	–36.5%, 63.8%	–0.34, 0.29

TABLE 8.3: The relative spread in $M'_{\text{intrinsic}}$ and $\delta M'(t)$ computed for the NGG simulation and two experimental datasets.

In order to understand the spread in both components, we compare to results obtained in the literature. A number of theoretical calculations of grain boundary energy and mobility are available [75, 76, 216–218]. For example, Refs. [75, 218] focus on a wide range of boundary types, rather than concentrating on special boundaries or only a limited number of boundaries, as in most of the literature. In their research, Olmsted *et al.* [75, 218] investigated the GB energy and mobility in Ni using atomistic simulations. The grain boundaries were constructed as CSL boundaries for computational convenience, since any non-CSL boundary can be approximated arbitrarily by a nearby CSL boundary [75]. The Σ values considered in their work ranged as high as 385. In this manner, a set of 388 grain boundaries was generated. The corresponding boundary energy was calculated using embedded-atom-based interatomic potentials [75], and the boundary mobility was obtained using a synthetic driving force coupled with molecular dynamics [218].

These authors investigated the relationship between both parameters (γ and M) and boundary misorientation separately. We replot their results in Fig. 8.8. In order to study the trends followed by more general boundaries, some special boundaries—including $\Sigma 3$,

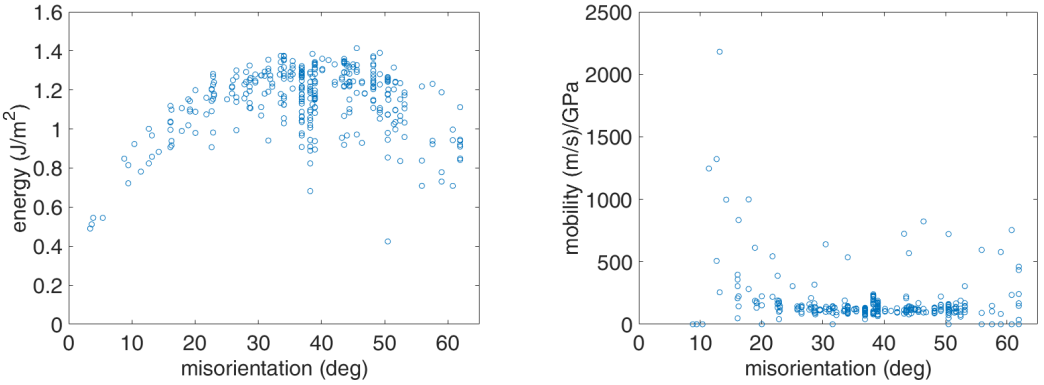

(a) (b)

FIGURE 8.8: The computed boundary energy and mobility using atomistic simulations for Ni plotted against boundary misorientation in (a) and (b), respectively. The plots are regenerated from the data of the general boundaries in Ni in Refs. [75, 218].

⟨111⟩ twist, and ⟨100⟩ twist boundaries—were excluded from in the plots of Fig. 8.8. At low misorientation angles, the boundary energy increases with misorientation (Fig. 8.8 (a)). Interestingly, a drop in energy is observed when the misorientation angle rises above about 45°. This is consistent with the results we obtained for AlMg (Fig. 6.10). However, the authors of Refs. [75] did not specify the reason for the drop. The same publication concludes that HAGBs show a significant spread in energy at fixed misorientation angle; thus, the GB energy cannot be treated as a single-valued parameter. We quantify the relative spread in the boundary energy values of (Fig. 8.8 (a)) using the 25th and 75th percentiles, finding a range of −10% to 7%. In Ref. [218], the relationship between boundary mobility and misorientation is determined. The computed mobility for general boundaries is plotted against misorientation in Fig. 8.8 (b). The boundary mobility is found to vary over a wide range, taking on values from 40 to 2000 (m/s)/GPa [218]. According to our quantification method, the relative spread in boundary mobility ranges from −16% to 26%.

From the computed spreads in boundary energy and mobility, the expected spread in the reduced mobility $M' = M \cdot \gamma$ can be estimated. Using the formula for the propagation of uncertainty, the relative spread in M' is estimated to cover the range of −19% to 27%. As discussed in Ref. [75], materials with similar crystal structure obey a scaling relation with respect to boundary properties, suggesting that the results for Ni in Refs. [75, 218] are applicable to our Al-based alloys, as Al and Ni share the same FCC crystal symmetry.

The spread in $M'_{\text{intrinsic}}$ for the AlCu specimen (Table 8.3) is considered to be roughly similar to the computed range for Ni, after taking into account the additional broadening of $M'_{\text{intrinsic}}$ that can be attributed to the analysis method itself. (The latter can be

quantified by the spread in $M'_{\text{intrinsic}}$ for the NGG simulation, which ranged from -13.4% to 13.2%.) For AlMg, however, the spread in $M'_{\text{intrinsic}}$ is still considerably larger. That is to say, the spread arising from intrinsic properties of a GB (plus measurement effects) cannot explain the spread that was actually observed for GBs in this sample. There must be additional factors that lead to significant variations in the boundary M' in AlMg. This is consistent with the conclusion drawn in the previous section regarding the higher percentage of boundaries with negative M' in AlMg. In this material, a potential source of variation could be the local concentration of solute atoms (Mg), which could modify the driving force for migration of an individual GB or exert a drag force on it.

Our finding of scattered values in $M'_{\text{intrinsic}}$ is supported by investigations performed at the atomistic scale. Recent research has revealed the existence of metastable grain boundary structures [219, 220]. Such metastability influences mesoscale boundary properties, such as the boundary energy and mobility. For example, based on atomistic bicrystal simulations of various materials, Han *et al.* [219] concluded that the dependency of the GB energy on misorientation is better described as an energy band than as a single curve, even for an individual grain boundary. Again, this is consistent with the findings of our analysis.

Reexamining the values listed in Table 8.3, we see that the spreads in the fluctuation term $\delta M'(t)$ are comparable for the two experimental datasets. However, both are larger than the spread for GBs in the NGG simulation (–0.11 to 0.10). The similarity between the two experimental datasets suggests that the spread in $\delta M'(t)$ originates from the same source. We must bear in mind, however, that several factors may contribute to this term. First, as we have already seen in previous chapters, experimental datasets exhibit errors in GB positions and migration distances, which can be traced to the 3DXRD technique and its reconstruction procedure. Additionally, during the migration of a given GB, its local inclination can vary with time, although the boundary misorientation remains unchanged. In light of the general dependency of M' on boundary inclination, a temporal change in GB inclination would manifest itself in our analysis as a fluctuation in the $\delta M'(t)$ term. Furthermore, recent theory [221], simulations [222] and experiments [223] demonstrate that GB migration occurs via the motion of disconnections along the interface.[1] During boundary migration, the disconnection state of the boundary varies, which leads to a change in the mesoscale properties of the grain boundary with time.

In light of the measured spreads in the $M'_{\text{intrinsic}}$ and $\delta M'(t)$ terms of Eq. 8.1, we conclude that the reduced mobility M' is not a single-valued function of the mesoscopic

[1] Disconnections are topological line defects constrained to an interface between two crystals, with both step and dislocation character [220, 224, 225].

GB properties (misorientation and inclination), but it rather depends in a complicated manner on additional microscopic properties, such as the local concentration of solute/impurity atoms and the metastable distribution of disconnections in the GB itself.

8.4 Conclusions

In this thesis work, a reverse engineering type of analysis was established to determine the reduced mobility of grain boundaries (GBs). Through accurate estimation of the boundary mean curvature and its migration velocity, the reduced mobility M' can be obtained directly for thousands of GBs in a polycrystalline specimen. The proposed method was validated against computer simulations of microstructural coarsening, in which M' was set to both isotropic and anisotropic values. In each such scenario, the reverse engineering method was found capable of extracting the ground truth value for M' to within about $\pm 10\%$.

Employing synchrotron-based 3DXRD microscopy, we recorded the 3D microstructural evolution that took place in an Al-1 wt% Mg specimen and in an Al-5 wt% Cu specimen. The resulting time-resolved 3D datasets were suitable for analysis at both the grain and grain boundary levels after data reconstruction and other necessary post-processing steps had been carried out. The grain growth that took place in the AlMg specimen was rather abnormal, as evidenced by the fact that neither a parabolic growth law nor time-invariance of the grain size distribution, which are the signature features of normal grain growth, were observed. Moreover, the scaled growth rates of individual grains manifested considerable scatter instead of being linearly proportional to the normalized grain radius. In contrast, experimental evidence demonstrated that grain growth in AlCu was of the normal type.

At the grain boundary level, the distribution of GB inclinations in AlMg showed a minor peak at {111} planes, which is commonly observed in FCC materials. Such peaks were weaker in AlCu. In general, in both specimens there was no strong dominant direction of the boundary inclination. However, the two samples showed a clear discrepancy in the GB misorientation distribution. A near Mackenzie distribution was found for the GB misorientation in AlCu, while an overabundance of low-angle grain boundaries was present in AlMg.

By applying the reverse engineering method to both datasets, we obtained values for the reduced mobility M' for grain boundaries during various annealing intervals. Relating the results to the boundary macroscopic properties, we determined that M' shows a weak inverse dependency on the boundary inclination population, but M' varies strongly

with the boundary misorientation. In both polycrystalline samples, M' increases with greater misorientation for LAGBs, but behaves differently in the high-angle regime.

Examining individual data points for M' in both experimental samples, we note that the reduced mobility varies significantly even for GBs of similar misorientation. The spread in M' values was found to be statistically significant after the subtraction of errors arising from the reverse engineering method itself. To understand the origin of these spreads, a decomposition of M' into an intrinsic component and a time-dependent fluctuation term was made. For AlMg, the values for $M'_{\text{intrinsic}}$ were more widely distributed than for AlCu, indicating that additional factors, such as a variation in the local concentration of solute atoms, might affect the migration of GBs in AlMg. The similar spread of the temporal fluctuation term in both samples can be understood as a consequence of the shared mechanism for GB migration at the atomistic scale: in the boundaries of both AlMg and AlCu, the disconnection content varies over time, resulting in a stochastic modification of M'. This nondeterministic feature of the reduced mobility suggests that the current state of the art in simulations of microstructure evolution, which typically employ only simplified models of mesoscale boundary properties, might be fundamentally unable to predict the grain-boundary-level evolution of polycrystalline microstructures, expect in a statistical sense. Additional information from atomistic investigations will have to be incorporated into such simulations if they are ever to gain true predictive power for the migration of GBs in real materials. In addition, the grain boundary connectivity might also need to be taken into consideration, as a network of grain boundaries need not evolve such that all boundaries necessarily move toward their centers of curvature; rather, the only stringent constraint on the network of grain boundaries is that its evolution must lower the total energy of the system.

Bibliography

[1] G. Gottstein and L. S. Shvindlerman. *Grain boundary migration in metals: thermodynamics, kinetics, applications*. CRC press, 2009.

[2] A. P. Sutton and R. W. Balluffi. *Interfaces in crystalline materials*. Clarendon Press Oxford, 1995.

[3] F. Humphreys and M. Hatherly. *Recrystallization and related annealing phenomena*. Elsevier, 2004.

[4] E. O. Hall. The deformation and ageing of mild steel: III Discussion of results. *Proceedings of the Physical Society. Section B*, 64:747–753, 1951.

[5] N. J. Petch. The cleavage strength of polycrystals. *Journal of the Iron and Steel Institute*, 174:25–28, 1953.

[6] J. Burke and D. Turnbull. Recrystallization and grain growth. *Progress in Metal Physics*, 3:220–292, 1952.

[7] G. S. Rohrer, D. M. Saylor, B. E. Dasher, B. L. Adams, A. D. Rollet, and P. Wynblatt. The distribution of internal interfaces in polycrystals. *Zeitschrift für Metallkunde*, 2004.

[8] G. S. Rohrer. Grain boundary energy anisotropy: a review. *Journal of Materials Science*, 46:5881–5895, 2011.

[9] D. A. Molodov. *Microstructural design of advanced engineering materials*. John Wiley & Sons, 2013.

[10] R. Sun and C. Bauer. Measurement of grain boundary mobilities through magnification of capillary forces. *Acta Metallurgica*, 18:635–638, 1970.

[11] R. Sun and C. Bauer. Tilt boundary migration in NaCl bicrystals. *Acta Metallurgica*, 18:639–647, 1970.

[12] M. Furtkamp, G. Gottstein, D. Molodov, V. Semenov, and L. Shvindlerman. Grain boundary migration in Fe–3.5% Si bicrystals with [001] tilt boundaries. *Acta Materialia*, 46:4103–4110, 1998.

[13] M. Furtkamp, G. Gottstein, and L. Shvindlerman. The shape of the moving grain boundary in the reversed-capillary technique under consideration of the drag effect. *Interface Science*, 6:279–288, 1998.

[14] D. Molodov, G. Gottstein, F. Heringhaus, and L. Shvindlerman. Motion of planar grain boundaries in bismuthbicrystals driven by a magnetic field. *Scripta Materialia*, 37:1207–1213, 1997.

[15] Y. Bhandari, S. Sarkar, M. Groeber, M. Uchic, D. Dimiduk, and S. Ghosh. 3D polycrystalline microstructure reconstruction from FIB generated serial sections for FE analysis. *Computational Materials Science*, 41:222–235, 2007.

[16] D. Rowenhorst, A. Gupta, C. Feng, and G. Spanos. 3D Crystallographic and morphological analysis of coarse martensite: Combining EBSD and serial sectioning. *Scripta Materialia*, 55:11–16, 2006.

[17] T. L. Matteson, S. W. Schwarz, E. C. Houge, B. W. Kempshall, and L. A. Giannuzzi. Electron backscattering diffraction investigation of focused ion beam surfaces. *Journal of Electronic Materials*, 31:33–39, 2002.

[18] M. D. Uchic, M. A. Groeber, D. M. Dimiduk, and J. Simmons. 3D microstructural characterization of nickel superalloys via serial-sectioning using a dual beam FIB-SEM. *Scripta Materialia*, 55:23–28, 2006.

[19] S. Zaefferer, S. Wright, and D. Raabe. Three-dimensional orientation microscopy in a focused ion beam–scanning electron microscope: A new dimension of microstructure characterization. *Metallurgical and Materials Transactions A*, 39: 374–389, 2008.

[20] H. F. Poulsen. An introduction to three-dimensional X-ray diffraction microscopy. *Journal of Applied Crystallography*, 45:1084–1097, 2012.

[21] W. Ludwig, S. Schmidt, E. M. Lauridsen, and H. F. Poulsen. X-ray diffraction contrast tomography: a novel technique for three-dimensional grain mapping of polycrystals. I. Direct beam case. *Journal of Applied Crystallography*, 41:302–309, 2008.

[22] I. McKenna, S. Poulsen, E. Lauridsen, W. Ludwig, and P. Voorhees. Grain growth in four dimensions: A comparison between simulation and experiment. *Acta Materialia*, 78:125–134, 2014.

[23] S. Schmidt, S. F. Nielsen, C. Gundlach, L. Margulies, X. Huang, and D. J. Jensen. Watching the growth of bulk grains during recrystallization of deformed metals. *Science*, 305:229–232, 2004.

[24] M. Syha, W. Rheinheimer, M. Bäurer, E. Lauridsen, W. Ludwig, D. Weygand, and P. Gumbsch. Three-dimensional grain structure of sintered bulk strontium titanate from X-ray diffraction contrast tomography. *Scripta Materialia*, 66:1–4, 2012.

[25] S. Schmidt, U. Olsen, H. Poulsen, H. Soerensen, E. Lauridsen, L. Margulies, C. Maurice, and D. J. Jensen. Direct observation of 3-D grain growth in Al-0.1% Mn. *Scripta Materialia*, 59:491–494, 2008.

[26] M. Syha. *Microstructure evolution in strontium titanate Investigated by means of grain growth simulations and x-ray diffraction contrast tomography experiments.* PhD thesis, Karlsruher Institut für Technologie, 2014.

[27] A. Trenkle, M. Syha, W. Rheinheimer, P. Callahan, L. Nguyen, W. Ludwig, W. Lenthe, M. P. Echlin, T. M. Pollock, D. Weygand, M. De Graef, M. J. Hoffmann, and P. Gumbsch. Nondestructive evaluation of 3D microstructure evolution in strontium titanate. *Journal of Applied Crystallography*, 53:349–359, 2020.

[28] X. Zhong, D. J. Rowenhorst, H. Beladi, and G. S. Rohrer. The five-parameter grain boundary curvature distribution in an austenitic and ferritic steel. *Acta Materialia*, 123:136–145, 2017.

[29] D. Rowenhorst, A. Lewis, and G. Spanos. Three-dimensional analysis of grain topology and interface curvature in a beta-titanium alloy. *Acta Materialia*, 58: 5511–5519, 2010.

[30] E. Miyoshi, T. Takaki, M. Ohno, Y. Shibuta, S. Sakane, T. Shimokawabe, and T. Aoki. Ultra-large-scale phase-field simulation study of ideal grain growth. *npj Computational Materials*, 2017.

[31] C. S. Smith. Grains, phases, and interfaces: an interpretation of microstructure. *Met Technol*, 15:1–37, 1948.

[32] D. Molodov, U. Czubayko, G. Gottstein, and L. Shvindlerman. On the effect of purity and orientation on grain boundary motion. *Acta Materialia*, 46:553–564, 1998.

[33] L. S. Shivindlerman, G. Gottstein, and D. A. Molodov. Grain boundary motion in pure metals: Effect of interaction between adsorbed atoms at moving boundaries. *physica status solidi (a)*, 160:419–429, 1997.

[34] C. Maurice and F. Humphreys. 2-and 3-D curvature driven vertex simulations of grain growth. *Grain Growth in Polycrystalline Materials*, 3:81–90, 1998.

[35] L. B. Mora, G. Gottstein, and L. Shvindlerman. Three-dimensional grain growth: Analytical approaches and computer simulations. *Acta Materialia*, 56:5915–5926, 2008.

[36] D. Fan and L.-Q. Chen. Computer simulation of grain growth using a continuum field model. *Acta Materialia*, 45:611–622, 1997.

[37] L.-Q. Chen and W. Yang. Computer simulation of the domain dynamics of a quenched system with a large number of nonconserved order parameters: The grain-growth kinetics. *Phys. Rev. B*, 50:15752–15756, 1994.

[38] J. Dennis, P. Bate, and F. Humphreys. Abnormal grain growth in Al-3.5Cu. *Acta Materialia*, 57:4539–4547, 2009.

[39] M. A. Miodownik. A review of microstructural computer models used to simulate grain growth and recrystallisation in aluminium alloys. *Journal of Light Metals*, 2:125–135, 2002.

[40] T. Watanabe. An approach to grain boundary design for strong and ductile polycrystals. *Res mechanica*, 1984.

[41] G. Palumbo, P. King, K. Aust, U. Erb, and P. Lichtenberger. Grain boundary design and control for intergranular stress-corrosion resistance. *Scripta Metallurgica et Materialia*, 25:1775–1780, 1991.

[42] G. Palumbo, E. M. Lehockey, and P. Lin. Applications for grain boundary engineered materials. *JOM*, 50:40–43, 1998.

[43] V. Randle. Twinning-related grain boundary engineering. *Acta Materialia*, 52: 4067–4081, 2004.

[44] V. Randle. Grain boundary engineering: an overview after 25 years. *Materials Science and Technology*, 26:253–261, 2010.

[45] A. P. Sutton, E. P. Banks, and A. R. Warwick. The five-dimensional parameter space of grain boundaries. *Proceedings of the Royal Society of London A: Mathematical, Physical and Engineering Sciences*, 471, 2015.

[46] A. Morawiec. *Orientations and rotations*. Springer, 2003.

[47] O. Engler and V. Randle. *Introduction to texture analysis: macrotexture, microtexture, and orientation mapping*. CRC press, 2009.

[48] D. Rowenhorst, A. D. Rollett, G. S. Rohrer, M. Groeber, M. Jackson, P. J. Konijnenberg, and M. D. Graef. Consistent representations of and conversions between 3D rotations. *Modelling and Simulation in Materials Science and Engineering*, 23: 083501, 2015.

[49] S. Patala, J. K. Mason, and C. A. Schuh. Improved representations of misorientation information for grain boundary science and engineering. *Progress in Materials Science*, 57:1383–1425, 2012.

[50] F. C. Frank. Orientation mapping. *Metall Trans A*, 19:403–408, 1988.

[51] A. Morawiec and D. P. Field. Rodrigues parameterization for orientation and misorientation distributions. *Philosophical Magazine A*, 73:1113–1130, 1996.

[52] H.-J. Bunge. *Texture analysis in materials science: mathematical methods*. Elsevier, 2013.

[53] A. J. Schwartz, M. Kumar, B. L. Adams, and D. P. Field. *Electron Backscatter Diffraction in Materials Science*. Springer, 2009.

[54] E. Werner and W. Prantl. Statistical treatment of measured orientation relationships in orientation space. *Journal of Applied Crystallography*, 21:311–316, 1988.

[55] K. Sztwiertnia, J. Pospiech, and F. Haessner. Reduction of misorientations between two cubic crystals into the base domain of axis–angle space. *Textures and Microstructures*, 12:233–242, 1990.

[56] J. K. Mackenzie. Second paper on statistics associated with the random disorientation of cubes. *Biometrika*, 45:229–240, 1958.

[57] A. Morawiec. Misorientation-angle distribution of randomly oriented symmetric objects. *Journal of Applied Crystallography*, 28:289–293, 1995.

[58] H. Grimmer. The distribution of disorientation angles if all relative orientations of neighbouring grains are equally probable. *Scripta Metallurgica*, 13:161–164, 1979.

[59] J. Mason and C. Schuh. The generalized Mackenzie distribution: Disorientation angle distributions for arbitrary textures. *Acta Materialia*, 57:4186–4197, 2009.

[60] E. R. Homer, S. Patala, and J. L. Priedeman. Grain boundary plane orientation fundamental zones and structure-property relationships. *Scientific Reports*, 5:15476, 2015.

[61] W. T. Read and W. Shockley. Dislocation models of crystal grain boundaries. *Phys. Rev.*, 78:275–289, 1950.

[62] J. M. Burgers. Geometrical considerations concerning the structural irregularities to be assumed in a crystal. *Proceedings of the Physical Society*, 52:23–33, 1940.

[63] W. D. Callister and D. G. Rethwisch. *Materials science and engineering: an introduction*, volume 7. Wiley New York, 2007.

[64] M. Winning, G. Gottstein, and L. Shvindlerman. Stress induced grain boundary motion. *Acta Materialia*, 49:211–219, 2001.

[65] M. Winning, G. Gottstein, and L. Shvindlerman. On the mechanisms of grain boundary migration. *Acta Materialia*, 50:353–363, 2002.

[66] M. Winning and A. D. Rollett. Transition between low and high angle grain boundaries. *Acta Materialia*, 53:2901–2907, 2005.

[67] K. Barmak, J. Kim, C.-S. Kim, W. Archibald, G. Rohrer, A. Rollett, D. Kinderlehrer, S. Ta'asan, H. Zhang, and D. Srolovitz. Grain boundary energy and grain growth in Al films: Comparison of experiments and simulations. *Scripta Materialia*, 54:1059–1063, 2006.

[68] M. Tang, B. W. Reed, and M. Kumar. Coarsening kinetics of topologically highly correlated grain boundary networks. *Journal of Applied Physics*, 112:043505, 2012.

[69] M. Kronberg and u. F. Wilson. Secondary recrystallization in copper. *JOM*, 1: 501–514, 1949.

[70] W. Bollmann. *Crystal defects and crystalline interfaces*. Springer Science & Business Media, 2012.

[71] D. Brandon. The structure of high-angle grain boundaries. *Acta Metallurgica*, 14: 1479–1484, 1966.

[72] A. Morawiec, J. Szpunar, and D. Hinz. Texture influence on the frequency of occurrence of CSL-boundaries in polycrystalline materials. *Acta Metallurgica et Materialia*, 41:2825–2832, 1993.

[73] K. Glowinski. *Methods for quantitative characterization of three-dimensional grain boundary networks in polycrystalline materials*. PhD thesis, Aleksander Krupkowski Institute of Metallurgy and Materials Science Polish Academy of Sciences, 2015.

[74] D. Brandon, B. Ralph, S. Ranganathan, and M. Wald. A field ion microscope study of atomic configuration at grain boundaries. *Acta Metallurgica*, 12:813–821, 1964.

[75] D. Olmsted, S. Foiles, and E. Holm. Survey of computed grain boundary properties in face-centered cubic metals: I. Grain boundary energy. *Acta Materialia*, 57:3694–3703, 2009.

[76] S. Ratanaphan, D. L. Olmsted, V. V. Bulatov, E. A. Holm, A. D. Rollett, and G. S. Rohrer. Grain boundary energies in body-centered cubic metals. *Acta Materialia*, 88:346–354, 2015.

[77] C. Herring. *Surface tension as a motivation for sintering*. New York: McGraw-Hill, 1951.

[78] B. Adams, S. Ta'Asan, D. Kinderlehrer, I. Livshits, D. Mason, C.-T. Wu, W. Mullins, G. Rohrer, A. Rollett, and D. Saylor. Extracting grain boundary and surface energy from measurement of triple junction geometry. *Interface Science*, 7:321–337, 1999.

[79] A. H. King. Triple lines in materials science and engineering. *Scripta Materialia*, 62:889–893, 2010.

[80] H. Park, D.-Y. Kim, N.-M. Hwang, Y.-C. Joo, C. H. Han, and J.-K. Kim. Microstructural evidence of abnormal grain growth by solid-state wetting in Fe-3%Si steel. *Journal of Applied Physics*, 95:5515–5521, 2004.

[81] K.-J. Ko, P.-R. Cha, D. Srolovitz, and N.-M. Hwang. Abnormal grain growth induced by sub-boundary-enhanced solid-state wetting: Analysis by phase-field model simulations. *Acta Materialia*, 57:838–845, 2009.

[82] W. W. Mullins. Theory of thermal grooving. *Journal of Applied Physics*, 28: 333–339, 1957.

[83] D. M. Saylor and G. S. Rohrer. Measuring the Influence of Grain-Boundary Misorientation on Thermal Groove Geometry in Ceramic Polycrystals. *Journal of the American Ceramic Society*, 82:1529–1536, 1999.

[84] A. Morawiec. Method to calculate the grain boundary energy distribution over the space of macroscopic boundary parameters from the geometry of triple junctions. *Acta Materialia*, 48:3525–3532, 2000.

[85] H. Beladi and G. S. Rohrer. The relative grain boundary area and energy distributions in a ferritic steel determined from three-dimensional electron backscatter diffraction maps. *Acta Materialia*, 61:1404–1412, 2013.

[86] H. Beladi, N. T. Nuhfer, and G. S. Rohrer. The five-parameter grain boundary character and energy distributions of a fully austenitic high-manganese steel using three dimensional data. *Acta Materialia*, 70:281–289, 2014.

[87] J. Li, S. J. Dillon, and G. S. Rohrer. Relative grain boundary area and energy distributions in nickel. *Acta Materialia*, 57:4304–4311, 2009.

[88] D. M. Saylor, A. Morawiec, and G. S. Rohrer. The relative free energies of grain boundaries in magnesia as a function of five macroscopic parameters. *Acta Materialia*, 51:3675–3686, 2003.

[89] S. J. Dillon and G. S. Rohrer. Characterization of the grain-boundary character and energy distributions of yttria using automated serial sectioning and EBSD in the FIB. *Journal of the American Ceramic Society*, 92:1580–1585, 2009.

[90] Y.-F. Shen, X. Zhong, H. Liu, R. M. Suter, A. Morawiec, and G. S. Rohrer. Determining grain boundary energies from triple junction geometries without discretizing the five-parameter space. *Acta Materialia*, 166:126–134, 2019.

[91] D. M. Saylor, A. Morawiec, and G. S. Rohrer. Distribution and energies of grain boundaries in magnesia as a function of five degrees of freedom. *Journal of the American Ceramic Society*, 85:3081–3083, 2002.

[92] D. M. Saylor, B. S. E. Dasher, A. D. Rollett, and G. S. Rohrer. Distribution of grain boundaries in aluminum as a function of five macroscopic parameters. *Acta Materialia*, 52:3649–3655, 2004.

[93] E. A. Holm, G. S. Rohrer, S. M. Foiles, A. D. Rollett, H. M. Miller, and D. L. Olmsted. Validating computed grain boundary energies in fcc metals using the grain boundary character distribution. *Acta Materialia*, 59:5250–5256, 2011.

[94] G. S. Rohrer, E. A. Holm, A. D. Rollett, S. M. Foiles, J. Li, and D. L. Olmsted. Comparing calculated and measured grain boundary energies in nickel. *Acta Materialia*, 58:5063–5069, 2010.

[95] M. Winning. Motion of ⟨100⟩-tilt grain boundaries. *Acta Materialia*, 51:6465–6475, 2003.

[96] J. Verhasselt, G. Gottstein, D. Molodov, and L. Shvindlerman. Shape of moving grain boundaries in Al-bicrystals. *Acta Materialia*, 47:887–892, 1999.

[97] W. W. Mullins. Magnetically induced grain-boundary motion in bismuth. *Acta metallurgica*, 4:421–432, 1956.

[98] D. Molodov, G. Gottstein, F. Heringhaus, and L. Shvindlerman. True absolute grain boundary mobility: motion of specific planar boundaries in Bi-bicrystals under magnetic driving forces. *Acta Materialia*, 46:5627–5632, 1998.

[99] A. Sheikh-Ali, D. Molodov, and H. Garmestani. Migration and reorientation of grain boundaries in Zn bicrystals during annealing in a high magnetic field. *Scripta Materialia*, 48:483–488, 2003.

[100] A. D. Sheikh-Ali, D. A. Molodov, and H. Garmestani. Boundary migration in Zn bicrystal induced by a high magnetic field. *Applied Physics Letters*, 82:3005–3007, 2003.

[101] C. Günster, D. A. Molodov, and G. Gottstein. Magnetically driven migration of specific planar grain boundaries in Zn bicrystals. *Scripta Materialia*, 63:300–303, 2010.

[102] C. Günster, D. A. Molodov, and G. Gottstein. Migration of grain boundaries in Zn. *Acta Materialia*, 61:2363–2375, 2013.

[103] M. Hillert. On the theory of normal and abnormal grain growth. *Acta Metallurgica*, 13:227–238, 1965.

[104] H. Atkinson. Overview no. 65: Theories of normal grain growth in pure single phase systems. *Acta Metallurgica*, 36:469–491, 1988.

[105] C. V. Thompson. Grain growth and evolution of other cellular structures. volume 55 of *Solid State Physics*, pages 269–314. Academic Press, 2001.

[106] A. Morawiec. On abnormal growth of Goss grains in grain-oriented silicon steel. *Scripta Materialia*, 64:466–469, 2011.

[107] G. Grest, M. Anderson, D. Srolovitz, and A. Rollett. Abnormal grain growth in three dimensions. *Scripta Metallurgica et Materialia*, 24:661–665, 1990.

[108] F. Humphreys. A unified theory of recovery, recrystallization and grain growth, based on the stability and growth of cellular microstructures—I. The basic model. *Acta Materialia*, 45:4231–4240, 1997.

[109] M. Bäurer, M. Syha, and D. Weygand. Combined experimental and numerical study on the effective grain growth dynamics in highly anisotropic systems: Application to barium titanate. *Acta Materialia*, 61:5664–5673, 2013.

[110] O. Engler and M.-Y. Huh. Evolution of the cube texture in high purity aluminum capacitor foils by continuous recrystallization and subsequent grain growth. *Materials Science and Engineering: A*, 271:371–381, 1999.

[111] E. Holm, M. Miodownik, and A. Rollett. On abnormal subgrain growth and the origin of recrystallization nuclei. *Acta Materialia*, 51:2701–2716, 2003.

[112] J. Dennis, P. S. Bate, and J. F. Humphreys. Abnormal grain growth in metals. In *Recrystallization and grain growth III*, volume 558 of *Materials Science Forum*, pages 717–722. Trans Tech Publications Ltd, 2007.

[113] M. Ferry, N. Hamilton, and F. Humphreys. Continuous and discontinuous grain coarsening in a fine-grained particle-containing Al–Sc alloy. *Acta Materialia*, 53: 1097–1109, 2005.

[114] A. Baldan. Review Progress in Ostwald ripening theories and their applications to nickel-base superalloys Part I: Ostwald ripening theories. *Journal of Materials Science*, 37(11):2171–2202, 2002.

[115] I. Lifshitz and V. Slyozov. The kinetics of precipitation from supersaturated solid solutions. *Journal of Physics and Chemistry of Solids*, 19:35–50, 1961.

[116] C. Wagner. Theorie der Alterung von Niederschlägen durch Umlösen (Ostwald-Reifung). *Zeitschrift für Elektrochemie, Berichte der Bunsengesellschaft für physikalische Chemie*, 65:581–591, 1961.

[117] S. C. Hardy and P. W. Voorhees. Ostwald ripening in a system with a high volume fraction of coarsening phase. *Metallurgical Transactions A*, 19:2713–2721, 1988.

[118] L. Ratke and P. W. Voorhees. *Growth and coarsening: Ostwald ripening in material processing*. Springer, 2002.

[119] T. Werz. *Ostwaldreifung bei hohen und ultra-hohen Volumenfraktionen*. PhD thesis, Ulm University, 2015.

[120] S. K. Kailasam, M. Glicksman, S. S. Mani, and V. E. Fradkov. Investigation of microstructural coarsening in Sn-Pb alloys. *Metallurgical and Materials Transactions A*, 30:1541–1547, 1999.

[121] P. W. Voorhees and M. E. Glicksman. Ostwald ripening during liquid phase sintering—Effect of volume fraction on coarsening kinetics. *Metallurgical and Materials Transactions A*, 15:1081–1088, 1984.

[122] D. Rowenhorst, J. Kuang, K. Thornton, and P. Voorhees. Three-dimensional analysis of particle coarsening in high volume fraction solid–liquid mixtures. *Acta Materialia*, 54:2027–2039, 2006.

[123] N. Limodin, L. Salvo, M. Suéry, and M. DiMichiel. In situ investigation by X-ray tomography of the overall and local microstructural changes occurring during partial remelting of an Al–15.8wt.% Cu alloy. *Acta Materialia*, 55:3177–3191, 2007.

[124] P. Streitenberger. Analytical description of phase coarsening at high volume fractions. *Acta Materialia*, 61:5026–5035, 2013.

[125] C. K. III and L.-Q. Chen. Computer simulation of 3-D grain growth using a phase-field model. *Acta Materialia*, 50:3059–3075, 2002.

[126] W. Bender and L. Ratke. Ostwald ripening of liquid phase sintered Cu-Co dispersions at high volume fractions. *Acta Materialia*, 46:1125–1133, 1998.

[127] H. Hesselbarth and I. Göbel. Simulation of recrystallization by cellular automata. *Acta Metallurgica et Materialia*, 39:2135–2143, 1991.

[128] K. G. F. Janssens. Random grid, three-dimensional, space-time coupled cellular automata for the simulation of recrystallization and grain growth. *Modelling and Simulation in Materials Science and Engineering*, 11:157–171, 2003.

[129] M. Bernacki, Y. Chastel, T. Coupez, and R. Logé. Level set framework for the numerical modelling of primary recrystallization in polycrystalline materials. *Scripta Materialia*, 58:1129–1132, 2008.

[130] R. Logé, M. Bernacki, H. Resk, L. Delannay, H. Digonnet, Y. Chastel, and T. Coupez. Linking plastic deformation to recrystallization in metals using digital microstructures. *Philosophical Magazine*, 88:3691–3712, 2008.

[131] M. Bernacki, H. Resk, T. Coupez, and R. E. Logé. Finite element model of primary recrystallization in polycrystalline aggregates using a level set framework. *Modelling and Simulation in Materials Science and Engineering*, 17:064006, 2009.

[132] H. Hallberg. A modified level set approach to 2D modeling of dynamic recrystallization. *Modelling and Simulation in Materials Science and Engineering*, 21: 085012, 2013.

[133] M. Bernacki, R. Loge, and T. Coupez. Level set framework for the finite-element modelling of recrystallization and grain growth in polycrystalline materials. *Scripta Materialia*, 64:525–528, 2011.

[134] Matt Elsey and Selim Esedoḡslu and Peter Smereka. Diffusion generated motion for grain growth in two and three dimensions. *Journal of Computational Physics*, 228:8015–8033, 2009.

[135] Y. Jin, N. Bozzolo, A. Rollett, and M. Bernacki. 2D finite element modeling of misorientation dependent anisotropic grain growth in polycrystalline materials: Level set versus multi-phase-field method. *Computational Materials Science*, 104: 108–123, 2015.

[136] C. Mießen, M. Liesenjohann, L. Barrales-Mora, L. Shvindlerman, and G. Gottstein. An advanced level set approach to grain growth—Accounting for grain boundary anisotropy and finite triple junction mobility. *Acta Materialia*, 99: 39–48, 2015.

[137] J. Fausty, N. Bozzolo, and M. Bernacki. A 2D level set finite element grain coarsening study with heterogeneous grain boundary energies. *Applied Mathematical Modelling*, 2019.

[138] E. A. Lazar, J. K. Mason, R. D. MacPherson, and D. J. Srolovitz. A more accurate three-dimensional grain growth algorithm. *Acta Materialia*, 59:6837–6847, 2011.

[139] M. Syha and D. Weygand. A generalized vertex dynamics model for grain growth in three dimensions. *Modelling and Simulation in Materials Science and Engineering*, 18:015010, 2010.

[140] D. Srolovitz, G. Grest, and M. Anderson. Computer simulation of recrystallization—I. Homogeneous nucleation and growth. *Acta Metallurgica*, 34:1833–1845, 1986.

[141] M. Miodownik, J. W. Martin, and A. Cerezo. Mesoscale simulations of particle pinning. *Philosophical Magazine A*, 79:203–222, 1999.

[142] N. Ono, K. Kimura, and T. Watanabe. Monte Carlo simulation of grain growth with the full spectra of grain orientation and grain boundary energy. *Acta Materialia*, 47:1007–1017, 1999.

[143] D. Zöllner and P. Streitenberger. Three-dimensional normal grain growth: Monte Carlo Potts model simulation and analytical mean field theory. *Scripta Materialia*, 54:1697–1702, 2006.

[144] N. Moelans, B. Blanpain, and P. Wollants. An introduction to phase-field modeling of microstructure evolution. *Calphad*, 32:268–294, 2008.

[145] W. J. Boettinger, J. A. Warren, C. Beckermann, and A. Karma. Phase-field simulation of solidification. *Annual Review of Materials Research*, 32:163–194, 2002.

[146] S. Tang, J. Wang, B. Svendsen, and D. Raabe. Competitive bcc and fcc crystal nucleation from non-equilibrium liquids studied by phase-field crystal simulation. *Acta Materialia*, 139:196–204, 2017.

[147] S. G. Kim, D. I. Kim, W. T. Kim, and Y. B. Park. Computer simulations of two-dimensional and three-dimensional ideal grain growth. *Phys. Rev. E*, 74:061605, 2006.

[148] N. Moelans, B. Blanpain, and P. Wollants. Pinning effect of second-phase particles on grain growth in polycrystalline films studied by 3-D phase field simulations. *Acta Materialia*, 55:2173–2182, 2007.

[149] N. Moelans, B. Blanpain, and P. Wollants. Quantitative analysis of grain boundary properties in a generalized phase field model for grain growth in anisotropic systems. *Phys. Rev. B*, 78:024113, 2008.

[150] H.-K. Kim, S. G. Kim, W. Dong, I. Steinbach, and B.-J. Lee. Phase-field modeling for 3D grain growth based on a grain boundary energy database. *Modelling and Simulation in Materials Science and Engineering*, 22:034004, 2014.

[151] E. Miyoshi and T. Takaki. Extended higher-order multi-phase-field model for three-dimensional anisotropic-grain-growth simulations. *Computational Materials Science*, 120:77–83, 2016.

[152] S. Vedantam and B. S. V. Patnaik. Efficient numerical algorithm for multiphase field simulations. *Phys. Rev. E*, 73:016703, 2006.

[153] J. Gruber, N. Ma, Y. Wang, A. D. Rollett, and G. S. Rohrer. Sparse data structure and algorithm for the phase field method. *Modelling and Simulation in Materials Science and Engineering*, 14:1189, 2006.

[154] L. Vanherpe, N. Moelans, B. Blanpain, and S. Vandewalle. Bounding box algorithm for three-dimensional phase-field simulations of microstructural evolution in polycrystalline materials. *Phys. Rev. E*, 76:056702, 2007.

[155] A. Vondrous, M. Selzer, J. Hötzer, and B. Nestler. Parallel computing for phase-field models. *The International Journal of High Performance Computing Applications*, 28:61–72, 2014.

[156] A. Yamanaka, T. Aoki, S. Ogawa, and T. Takaki. GPU-accelerated phase-field simulation of dendritic solidification in a binary alloy. *Journal of Crystal Growth*, 318:40–45, 2011.

[157] T. Takaki, T. Shimokawabe, M. Ohno, A. Yamanaka, and T. Aoki. Unexpected selection of growing dendrites by very-large-scale phase-field simulation. *Journal of Crystal Growth*, 382:21–25, 2013.

[158] S. Sakane, T. Takaki, M. Ohno, T. Shimokawabe, and T. Aoki. GPU-accelerated 3D phase-field simulations of dendrite competitive growth during directional solidification of binary alloy. *IOP Conference Series: Materials Science and Engineering*, 84:012063, 2015.

[159] T. Takaki, R. Rojas, M. Ohno, T. Shimokawabe, and T. Aoki. GPU phase-field lattice Boltzmann simulations of growth and motion of a binary alloy dendrite. *IOP Conference Series: Materials Science and Engineering*, 84:012066, 2015.

[160] Y. Shibuta, M. Ohno, and T. Takaki. Solidification in a supercomputer: From crystal nuclei to dendrite assemblages. *JOM*, 67:1793–1804, 2015.

[161] T. Takaki, M. Ohno, Y. Shibuta, S. Sakane, T. Shimokawabe, and T. Aoki. Two-dimensional phase-field study of competitive grain growth during directional solidification of polycrystalline binary alloy. *Journal of Crystal Growth*, 442:14–24, 2016.

[162] A. Manin. Simulation and modeling of grain growth using a misorientation-dependent phase field model. Master's thesis, Universität Ulm, 2015.

[163] D. Fan and L.-Q. Chen. Diffuse-interface description of grain boundary motion. *Philosophical Magazine Letters*, 75:187–196, 1997.

[164] L.-Q. Chen and D. Fan. Computer simulation model for coupled grain growth and Ostwald ripening—Application to $Al_2O_3 - ZrO_2$ two-phase systems. *Journal of the American Ceramic Society*, 79:1163–1168, 1996.

[165] D. Fan and L.-Q. Chen. Diffusion-controlled grain growth in two-phase solids. *Acta Materialia*, 45:3297–3310, 1997.

[166] D. Fan and L.-Q. Chen. Topological evolution during coupled grain growth and Ostwald ripening in volume-conserved 2-D two-phase polycrystals. *Acta Materialia*, 45:4145–4154, 1997.

[167] D. Fan, S. Chen, L.-Q. Chen, and P. Voorhees. Phase-field simulation of 2-D Ostwald ripening in the high volume fraction regime. *Acta Materialia*, 50:1895–1907, 2002.

[168] S. G. Kim. Large-scale three-dimensional simulation of Ostwald ripening. *Acta Materialia*, 55:6513–6525, 2007.

[169] K. G. Wang and H. Yan. Simulating three-dimensional phase coarsening at ultra-high volume fractions by phase-field method. In *Solid State Phenomena*, volume 172, pages 1112–1118. Trans Tech Publ, 2011.

[170] S. Poulsen, P. Voorhees, and E. Lauridsen. Three-dimensional simulations of microstructural evolution in polycrystalline dual-phase materials with constant volume fractions. *Acta Materialia*, 61:1220–1228, 2013.

[171] V. Yadav, L. Vanherpe, and N. Moelans. Effect of volume fractions on microstructure evolution in isotropic volume-conserved two-phase alloys: A phase-field study. *Computational Materials Science*, 125:297–308, 2016.

[172] D. Fan, L.-Q. Chen, S. Chen, and P. W. Voorhees. Phase field formulations for modeling the Ostwald ripening in two-phase systems. *Computational Materials Science*, 9:329–336, 1998.

[173] J. Alkemper and P. W. Voorhees. Quantitative serial sectioning analysis. *Journal of Microscopy*, 201:388–394, 2001.

[174] J. E. Spowart, H. E. Mullens, and B. T. Puchala. Collecting and analyzing microstructures in three dimensions: A fully automated approach. *JOM*, 55:35–37, 2003.

[175] G. Johnson, A. King, M. G. Honnicke, J. Marrow, and W. Ludwig. X-ray diffraction contrast tomography: a novel technique for three-dimensional grain mapping of polycrystals. II. The combined case. *Journal of Applied Crystallography*, 41: 310–318, 2008.

[176] H. F. Poulsen, W. Ludwig, E. M. Lauridsen, S. Schmidt, W. Pantleon, U. L. Olsen, J. Oddershede, P. Reischig, A. Lyckegaard, J. Wright, et al. 4D characterization of metals by 3DXRD. In *31st Risø International Symposium on Materials Science: Challenges in materials science and possibilities in 3D and 4D characterization techniques*, pages 101–119, 2010.

[177] R. Quey and L. Renversade. Optimal polyhedral description of 3D polycrystals: Method and application to statistical and synchrotron X-ray diffraction data. *Computer Methods in Applied Mechanics and Engineering*, 330:308–333, 2018.

[178] O. Sedivy, J. Dake, C. Krill, V. Schmidt, and A. Jäger. Description of the 3D morphology of grain boundaries in aluminum alloys using tessellation models generated by ellipsoids. *Image Anal Stereol*, 2017.

[179] L. Petrich, J. Staněk, M. Wang, D. Westhoff, L. Heller, P. Šittner, C. E. Krill, V. Beneš, and V. Schmidt. Reconstruction of Grains in Polycrystalline Materials From Incomplete Data Using Laguerre Tessellations. *Microscopy and Microanalysis*, 25:743–752, 2019.

[180] E. Lauridsen, H. Poulsen, S. Nielsen, and D. J. Jensen. Recrystallization kinetics of individual bulk grains in 90% cold-rolled aluminium. *Acta Materialia*, 51:4423–4435, 2003.

[181] N. Iqbal, N. van Dijk, S. Offerman, M. Moret, L. Katgerman, and G. Kearley. Real-time observation of grain nucleation and growth during solidification of aluminium alloys. *Acta Materialia*, 53:2875–2880, 2005.

[182] M. Faraji, J. Wright, and L. Katgerman. In-situ observation of the nucleation kinetics and the mechanism of grain refinement in Al–Si alloys (Part I). *Materials Letters*, 64:1016–1018, 2010.

[183] R. V. Martins, L. Margulies, S. Schmidt, H. F. Poulsen, and T. Leffers. Simultaneous measurement of the strain tensor of 10 individual grains embedded in an Al tensile sample. *Materials Science and Engineering: A*, 387-389:84–88, 2004.

[184] B. Jakobsen, H. F. Poulsen, U. Lienert, J. Almer, S. D. Shastri, H. O. Sørensen, C. Gundlach, and W. Pantleon. Formation and subdivision of deformation structures during plastic deformation. *Science*, 312:889–892, 2006.

[185] H. F. Poulsen, S. F. Nielsen, E. M. Lauridsen, S. Schmidt, R. M. Suter, U. Lienert, L. Margulies, T. Lorentzen, and D. Juul Jensen. Three-dimensional maps of grain boundaries and the stress state of individual grains in polycrystals and powders. *Journal of Applied Crystallography*, 34:751–756, 2001.

[186] L. Margulies, T. Lorentzen, H. Poulsen, and T. Leffers. Strain tensor development in a single grain in the bulk of a polycrystal under loading. *Acta Materialia*, 50: 1771–1779, 2002.

[187] P. Sedmák, J. Pilch, L. Heller, J. Kopeček, J. Wright, P. Sedlák, M. Frost, and P. Šittner. Grain-resolved analysis of localized deformation in nickel-titanium wire under tensile load. *Science*, 353:559–562, 2016.

[188] J. Oddershede, S. Schmidt, H. F. Poulsen, H. O. Sørensen, J. Wright, and W. Reimers. Determining grain resolved stresses in polycrystalline materials using three-dimensional X-ray diffraction. *Journal of Applied Crystallography*, 43: 539–549, 2010.

[189] J. Oddershede, S. Schmidt, H. F. Poulsen, and W. Reimers. Measuring Type II Stresses Using 3DXRD. In *Mechanical Stress Evaluation by Neutrons and Synchrotron Radiation*, volume 652 of *Materials Science Forum*, pages 63–69. Trans Tech Publications Ltd, 2010.

[190] L. Margulies, G. Winther, and H. F. Poulsen. In situ measurement of grain rotation during deformation of polycrystals. *Science*, 291:2392–2394, 2001.

[191] G. Winther, L. Margulies, S. Schmidt, and H. Poulsen. Lattice rotations of individual bulk grains Part II: correlation with initial orientation and model comparison. *Acta Materialia*, 52:2863–2872, 2004.

[192] J. M. Dake, J. Oddershede, H. O. Sørensen, T. Werz, J. C. Shatto, K. Uesugi, S. Schmidt, and C. E. Krill. Direct observation of grain rotations during coarsening of a semisolid Al–Cu alloy. *Proceedings of the National Academy of Sciences*, 113: E5998–E6006, 2016.

[193] W. Ludwig, P. Reischig, A. King, M. Herbig, E. M. Lauridsen, G. Johnson, T. J. Marrow, and J. Y. Buffiere. Three-dimensional grain mapping by x-ray diffraction contrast tomography and the use of Friedel pairs in diffraction data analysis. *Review of Scientific Instruments*, 80:033905, 2009.

[194] P. Reischig, A. King, L. Nervo, N. Viganó, Y. Guilhem, W. J. Palenstijn, K. J. Batenburg, M. Preuss, and W. Ludwig. Advances in X-ray diffraction contrast tomography: flexibility in the setup geometry and application to multiphase materials. *Journal of Applied Crystallography*, 46:297–311, 2013.

[195] A. King, P. Reischig, J. Adrien, and W. Ludwig. First laboratory X-ray diffraction contrast tomography for grain mapping of polycrystals. *Journal of Applied Crystallography*, 46:1734–1740, 2013.

[196] S. McDonald, C. Holzner, E. Lauridsen, P. Reischig, A. Merkle, and P. Withers. Microstructural evolution during sintering of copper particles studied by laboratory diffraction contrast tomography (LabDCT). *Scientific Reports*, 7, 2017.

[197] S. McDonald, P. Reischig, C. Holzner, E. Lauridsen, P. Withers, A. Merkle, and M. Feser. Non-destructive mapping of grain orientations in 3D by laboratory X-ray microscopy. *Scientific reports*, 5, 2015.

[198] J. Dake. *Experimental Investigations of Microstructural Coarsening in 3D using X-Ray Microscopy*. PhD thesis, Ulm University, 2019.

[199] D. Swinehart. The beer-lambert law. *Journal of chemical education*, 39:333, 1962.

[200] S. Schmidt. Personal communication 2017. .

[201] J. Oddershede, S. Schmidt, M. Koker, and D. Dale. Near-field mapping with box beam using FABLE and GrainSweeper.3D.

[202] S. Schmidt. GrainSweeper. https://anaconda.org/fable/grainsweeper. .

[203] J. Wright. ImageD11. https://github.com/FABLE-3DXRD/ImageD11.

[204] S. Schmidt. GrainSpotter: a fast and robust polycrystalline indexing algorithm. *Journal of Applied Crystallography*, 47:276–284, 2014.

[205] M. Groeber and M. Jackson. DREAM.3D: a digital representation environment for the analysis of microstructure in 3D. *Integrating Materials and Manufacturing Innovation*, 3:5, 2014.

[206] D. A. Field. Laplacian smoothing and Delaunay triangulations. *Communications in Applied Numerical Methods*, 4:709–712, 1988.

[207] J. Goldfeather and V. Interrante. A novel cubic-order algorithm for approximating principal direction vectors. *ACM Trans. Graph.*, 23:45–63, 2004.

[208] A. Belyaev. Mesh smoothing and enhancing. Curvature estimation. Saarbrucken, 2006.

[209] M. Wang, S. Wu, and C. E. Krill. Extraction of grain boundary curvature from voxel-based representations of polycrystalline microstructures. *IOP Conference Series: Materials Science and Engineering*, 580:012048, 2019.

[210] Y. Suwa and Y. Saito. Computer simulation of grain growth by the phase field model. Effect of interfacial energy on kinetics of grain growth. *Materials Transactions*, 44:2245–2251, 2003.

[211] T. Massalski. *Binary Alloys Phase Diagrams*, volume 1, pages 141–143. ASM International, Materials Park, OH, 3 edition, 1996.

[212] D. Wolf and S. Phillpot. Role of the densest lattice planes in the stability of crystalline interfaces: A computer simulation study. *Materials Science and Engineering: A*, 107:3–14, 1989.

[213] H. Miura, M. Kato, and T. Mori. Temperature dependence of the energy of Cu [110] symmetrical tilt grain boundaries. *Journal of materials science letters*, 13: 46–48, 1994.

[214] D. Molodov, U. Czubayko, G. Gottstein, and L. Shvindlerman. Mobility of $\langle 111 \rangle$ tilt grain boundaries in the vicinity of the special misorientation $\Sigma = 7$ in bicrystals of pure aluminum. *Scripta Metallurgica et Materialia; (United States)*, 32:4, 1995.

[215] M. Taheri, D. Molodov, G. Gottstein, and A. Rollett. Grain boundary mobility under a stored-energy driving force: a comparison to curvature-driven boundary migration. *Zeitschrift für Metallkunde*, 96:1166–1170, 2005.

[216] M. Upmanyu, D. Srolovitz, L. Shvindlerman, and G. Gottstein. Misorientation dependence of intrinsic grain boundary mobility: simulation and experiment. *Acta Materialia*, 47:3901–3914, 1999.

[217] G. Gottstein, D. Molodov, L. Shvindlerman, D. Srolovitz, and M. Winning. Grain boundary migration: misorientation dependence. *Current Opinion in Solid State and Materials Science*, 5:9–14, 2001.

[218] D. Olmsted, E. Holm, and S. Foiles. Survey of computed grain boundary properties in face-centered cubic metals-II: Grain boundary mobility. *Acta Materialia*, 57: 3704–3713, 2009.

[219] J. Han, V. Vitek, and D. J. Srolovitz. Grain-boundary metastability and its statistical properties. *Acta Materialia*, 104:259–273, 2016.

[220] J. Han, S. L. Thomas, and D. J. Srolovitz. Grain-boundary kinetics: A unified approach. *Progress in Materials Science*, 98:386–476, 2018.

[221] L. Zhang, J. Han, Y. Xiang, and D. J. Srolovitz. Equation of motion for a grain boundary. *Phys. Rev. Lett.*, 119:246101, 2017.

[222] A. Rajabzadeh, F. Mompiou, M. Legros, and N. Combe. Elementary mechanisms of shear-coupled grain boundary migration. *Phys. Rev. Lett.*, 110:265507, 2013.

[223] Q. Zhu, G. Cao, J. Wang, C. Deng, J. Li, Z. Zhang, and S. X. Mao. In situ atomistic observation of disconnection-mediated grain boundary migration. *Nature communications*, 10:156, 2019.

[224] C. M. F. Rae and D. A. Smith. On the mechanisms of grain boundary migration. *Philosophical Magazine A*, 41:477–492, 1980.

[225] J. Hirth. Dislocations, steps and disconnections at interfaces. *Journal of Physics and Chemistry of Solids*, 55:985–989, 1994.

List of Publications

Parts of this dissertation have already been published in the following journal articles:

M. Wang, S. Wu and C. E. Krill III. Extraction of grain boundary curvature from voxel-based representations of polycrystalline microstructures. *IOP Conference Series: Materials Science and Engineering*, 580:012048, 2019.

O. Furat, M. Wang, M. Neumann, L. Petrich, M. Weber, C. E. Krill III and V. Schmidt. Machine learning techniques for the segmentation of tomographic image data of functional materials. *Frontiers in Materials*, 6:145, 2019.

L. Petrich, J. Staněk, M. Wang, D. Westhoff, L. Heller, P. Šittner, C. E. Krill III, V. Beneš and V. Schmidt. Reconstruction of grains in polycrystalline materials from incomplete data using Laguerre tessellations. *Microscopy and Microanalysis*, 25:743–752, 2019.

List of Conference Contributions

M. Wang, J. M. Dake, S. Schmidt, D. A. Molodov, and C. E. Krill III. Reverse engineering the kinetics of grain growth in Al-based polycrystals by microstructural mapping in 4D. Oral presentation, *40th Risø International Symposium on Materials Science*, Roskilde, Denmark, 2019.

M. Wang, J. M. Dake, S. Schmidt, and C. E. Krill III. Reverse engineering the kinetics of grain growth from time-resolved 3DXRD measurements. Oral presentation, *DPG Spring Meeting*, Regensburg, Germany, 2019.

M. Wang, L. Petrich, D. Westhoff, V. Schmidt, and C. E. Krill III. Description of 3D polycrystalline microstructures using a tessellation model generated by ellipsoids. Poster presentation, *DPG Spring Meeting*, Berlin, Germany, 2018.

M. Wang, J. M. Dake, J. Oddershede, H. O. Sørensen, S. Schmidt, and C. E. Krill III. Extracting the kinetics of grain growth in Al-based polycrystals from 4D measurements. Oral presentation, *DPG Spring Meeting*, Dresden, Germany, 2017.

M. Wang, J. M. Dake, A. Manin, J. Oddershede, H. O. Sørensen, S. Schmidt, and C. E. Krill III. Probing abnormal grain growth in polycrystalline materials in 4D using 3DXRD measurement and phase field simulation. Oral presentation, *6th International Conference on Recrystallization and Grain Growth*, Pittsburgh, USA, 2016.

M. Wang, J. M. Dake, A. Manin, and C. E. Krill III. Probing texture-induced abnormal grain growth in polycrystalline materials in 4D. Poster presentation, *DPG Spring Meeting*, Regensburg, Germany, 2016.

M. Wang, J. M. Dake, R. Birringer, and C. E. Krill III. Simulation of fractal abnormal grain growth in nanocrystalline materials. Oral presentation, *DPG Spring Meeting*, Berlin, Germany, 2015.

M. Wang, J. M. Dake, and C. E. Krill III. Simulation of fractal abnormal grain growth in nanocrystalline materials. Poster presentation, *Workshop: Microstructural Functionality: Dynamics, Adaption, and Self-Healing at the Nanoscale*, Duisburg, Germany, 2014.

Acknowledgments

I would like first and foremost to thank my supervisor, Prof. Carl Krill, for giving me the opportunity to work on such an exciting project. Throughout my entire PhD study, I have received insightful advice and constant encouragement from him. Only with his patient guidance have I become a qualified scientist—not only in doing research but also in delivering knowledge to others. Additionally, I appreciate the invaluable discussions and suggestions from him that improved this dissertation.

I am also grateful to my second referee, Prof. Marc Bernacki, for taking the time and effort in reading and critiquing this dissertation, which made its contents complete. I enjoy the scientific discussions with him that are not only interesting and inspiring but also always informative about the state-of-art progress on the related topics.

I am very fortunate to be part of Carl's research group also for the reason that everyone in the group is amazing and helpful. I would like to express my gratefulness to Dr. Jules Dake, who was my tutor in my Master's thesis research and later became my colleague in the group. His scientific spirit has always motivated me to never stop moving forward with research. He passed along all the valuable experience and knowledge to me without reservation, which only made my work smoother. I will always cherish the great time we have had together both professionally and personally. The same gratitude goes to Dr. Thomas Werz. Although he had nearly finished up his research when I joined the group, his constant visits back to the university brought me not only constructive scientific discussions but also inspirational life encouragement. I treasure the research experience with my research buddy in the group, Raphael Zeller. The travel we spent together for conferences and workshops will be an unforgettable memory of my PhD period.

One of the greatest challenges of my research was doing 3DXRD measurement in the Japanese synchrotron facility. Besides the helpful guidance and precious experience I gained from Carl and Jules, I am also indebted to Dr. Søren Schmidt. His help always eased the stress in carrying out the experiments. Even when he was not on-site, our remote discussions only helped with the experimental progress. His expertise is pivotal for my experimental measurements and data reconstruction. Progress in phase field computer simulations could not have been made so quickly without initial help from Dr. Nan Wang, to whom I show my deepest gratitude. I appreciate the efficient cooperation we had in performing hours of simulations. I would also like to thank the colleagues in the Institute of Stochastics, Dr. Ondrej Sedivy, Lukas Petrich, Orkun Furat, Dr. Daniel Westhoff and Prof. Volker Schmidt. The collaborative work with them has not only solved critical issues in my research but also expanded my sights in science. I

will never forget the time I spent together with the undergraduate students I supervised: Anton Manin, Shuang Wu, and Tahir Vucic. I am grateful to their help in developing simulation algorithms, implementing analysis methods and performing laboratory work.

Working in the former Institute of Micro and Nanomaterials was a more than pleasant experience in my PhD journey. I appreciate all the help from Dr. Kai Brühne, who gave me so much support on academic as well as administrative work, without which I could not have gotten focused on research. I also sincerely thank Prof. Hans-Jörg Fecht and Prof. Ulrich Herr for their feedback and suggestions regarding my research and seminar presentations. I would like to thank my office mates, Dr. Yue Dong, Dr. Pierre Denis and Dr. Mike Haddad, without whom my research life would have been less fun. Through daily discussions, some great ideas just jumped out due to these colleagues' diversity in research fields. I also would like to express my gratitude to the other members of the institute, including Dr. Markus Mohr, Runbang Shao, Florian Ostermaier, Alexander Minkow, and Günter Nusser, for building up an excellent research environment and the help I received from them.

Finally, I would like to thank my parents for their support and love. Despite the long distance, I received constant encouragement from their phone calls. To my wife Zhan, I will always cherish and appreciate the time we have spent together in this meaningful period of life!

Mingyan Wang

Birth year 1990
Place of birth Shandong, China

PROFESSIONAL EXPERIENCE

Software Engineer *Aug. 2020 - present*

Nordson MATRIX, *Feldkirchen, Germany*

- Development of image processing algorithms and inspection procedures for industrial X-ray inspection systems.

EDUCATION

Universität Ulm, *Ulm, Germany* *May. 2014 - Jun. 2021*

PhD candidate and research assistant, ***Institute of Functional Nanosystems***

- Research topic: Reverse Engineering the Kinetics of Grain Growth in Al-Based Polycrystals by Microstructural Mapping in 4D.
- Teaching assistant of lectures and lab courses: Computational Methods in Materials Science, Technical Presentation Skill for Engineers, X-Ray Diffractometer, X-Ray Fluorescence, etc.

Universität Ulm, *Ulm, Germany* *Oct. 2011 - Apr. 2014*

Master of Science, major in ***Advanced Materials*** *(grade 1,3)*

- Master's thesis: Simulation of Abnormal Grain Growth in Nanomaterials (grade 1,0)
- Awards: Baden-Württemberg-STIPENDIUM (2011), DAAD Studienabschluss-Stipendium (2013).

Southeast University, *Nanjing, China* *Sep. 2008 - Jun. 2012*

Bachelor of Engineering, major in ***Biomedical Engineering***